Selective Laser Melting-produced Ti6Al4V: Influence of annealing strategies on crystallographic microstructure and tensile behaviour

by
Gerrit Matthys Ter Haar

Thesis presented in partial fulfilment of the requirements for the degree of Master of Engineering Mechanical in the Faculty of Engineering at Stellenbosch University

Supervisor: Dr T. H. Becker
Co-supervisor: Prof D.C. Blaine

December 2017

DECLARATION

By submitting this thesis electronically, I declare that the entirety of the work contained therein is my own, original work, that I am the sole author thereof (save to the extent explicitly otherwise stated), that reproduction and publication thereof by Stellenbosch University will not infringe any third-party rights and that I have not previously in its entirety or in part submitted it for obtaining any qualification.

Date: December 2017

ABSTRACT

The ability to manufacture complex shapes and structures with little material waste, among other advantages, makes the metal additive manufacturing technique of Selective Laser Melting a superior manufacturing technique. The titanium alloy, Ti6Al4V, serves as a great material of choice for this manufacturing technique due to its excellent mechanical properties and its biocompatibility. These factors make Ti6Al4V parts produced through SLM highly applicable and valuable in the biomedical and aerospace industries. Due to limited research and development in the field however, part quality in terms of achievable mechanical properties, residual stress and density has been below standard (such as that achieved by wrought Ti6Al4V parts).

The study aimed to gain a fundamental understanding of the influence of annealing strategies on the microstructure of SLM-produced Ti6Al4V to improve and optimise the tensile properties of the material. SLM-produced Ti6Al4V tensile samples were subject to various tailored heat treatment strategies. Analysis of microstructure through optical and electron backscatter diffraction allowed for correlations to be made between the annealing strategies and the microstructure as well as between the printing process and the microstructure. Tensile test results of annealed samples show a decrease in tensile strength with an increase in annealing temperature as well as an increase in ductility and stiffness with an increase in annealing temperature. It was found that the fine martensitic (α') microstructure of the as-built samples decomposes into a dual-phase (α+β) microstructure at ~800 °C, thereby improving ductility and stiffness. An optimal duplex annealing strategy allows for a bi-lamellar microstructure to be formed which allows for a substantial increase in ductility while maintaining a high material strength.

OPSOMMING

Die vermoë om komplekse vorms en strukture te vervaardig met min afvalmateriaal, om slegs een voordeel te noem, maak die metaaltoevoegingsvervaardiging tegniek van Selektiewe Laser Smelting (SLM) 'n tegniek van voorkeur. Die titanium legering, Ti6Al4V, dien as die materiaal van keuse vir hierdie tegniek as gevolg van sy uitstekende meganiese eienskappe en sy vermoë om suksesvol met biologiese weefsel te integreer. Hierdie faktore maak Ti6Al4V dele geproduseer deur SLM hoogs toepaslik en waardevol in die biomediese en ruimte industrieë. Weens beperkte navorsing en ontwikkeling tot dusver in die gebied, is part kwaliteit, in terme van haalbare meganiese eienskappe, residuele spanning en digtheid, onder standaard (soos wat bereik word deur smee Ti6Al4V dele).

Die studie was daarop gemik om 'n fundamentele begrip van die invloed van uitgloeiing strategieë op die mikrostruktuur van SLM-geproduseerde Ti6Al4V te kry, om sodoende die meganiese eienskappe van die materiaal te verbeter en te optimaliseer. SLM-geproduseerde Ti6Al4V trek monsters was onderhewig aan verskeie hitte behandeling strategieë. Ontleding van die mikrostruktuur deur optiese en elektroniese terugstrooiings diffraksie het toegelaat om die uitgloeiing strategieë met die mikrostruktuur te korreleer, asook die SLM-proses met die mikrostruktuur. Trektoetsresultate van uitgegloeide monsters het 'n afname in treksterkte met 'n toename in uitgloeiing temperatuur asook 'n toename in smeebaarheid en styfheid met 'n toename in uitgloeiing temperatuur getoon. Daar is bevind dat die fyn martensitiese (α') mikrostruktuur van die as-vervaardigde monsters ontbind in 'n dubbele-fase (α+β) mikrostruktuur by ~800 ° C, en sodoende verbeter smeebaarheid en styfheid van die materiaal. 'n Optimale dupleks uitgloeiing strategie het toegelaat vir 'n dubbel-lamellêre mikrostruktuur om gevorm te word. Dié mikrostruktuur het 'n aansienlike toename in smeebaarheid getoon, asook 'n behoud van hoë materiaal sterkte.

ACKNOWLEDGEMENTS

The author would like to acknowledge the following individuals who had a significant impact, either directly or indirectly, on the study during the past two years:

Dr T. H. Becker for his knowledgeable leadership and keen enthusiasm in the project. Prof D. C. Blaine for her invaluable contribution to the quality of the final document.

Colleague, Melody van Rooyen, for her effort in improving the quality of the thesis.

Colleague, Richard Huchzermeyer, for his moral support through encouragement and laughter during the late hours in the office.

The Department of Science and Technology and the Centre for Scientific and Industrial Research for the critical funding made available through the collaborative program in additive manufacturing.

Finally, I would like to express my appreciation to my parents, Jeroen and Anell, for their encouragements and support and to Tersia, for her moral support during the writing of the thesis.

TABLE OF CONTENTS

Page

LIST OF ABBREVIATIONS AND SYMBOLS

Abbreviations

3D	three-dimensional
AC	air cool
AM	additive manufacturing
ASTM	American Standard Testing Method
BA	β anneal
BCC	body centred cubic
BD	build direction
BOR	Burgers Orientation Relationship
CAD	computer aided drawing
CAF	Central Analytical Facilities
CP	commercially pure
CRSS	critical resolve shear stress
CSIR	Centre for Scientific and Industrial Research
CT	computer tomography
CUT	Central University of Technology
DIC	differential interference contrast
DSC	differential scanning calorimetry
DST	Department of Science and Technology
EBM	electron beam melting
EBSD	electron backscatter diffraction
EC	European Commission
ELI	extra low interstitial
FC	furnace cool
HAGB	high angle grain boundary

HCP	hexagonal close-packed
HIP	hot isostatic pressing
hrs	hours
HSV	hue-saturation-value
IPF	inverse pole figure
ISO	International Standards Organisation
LAGB	low angle grain boundary
LENS	Laser Engineered Net Shaping
LMD	Laser Melting Deposition
MA	mill anneal
MAM	metal additive manufacturing
MIT	Massachusetts Institute of Technology
ND	normal direction
PM	powder metallurgy
PF	pole figure
ppmw	parts per million weight
RD	roll direction
ROI	region of interest
RP	rapid prototyping
RT	rapid tooling
SEM	scanning electron microscope
SLM	Selective Laser Melting
SLS	Selective Laser Sintering
STA	solution treated and aged
STL	Stereolithography
SU	Stellenbosch University
TC	thermocouple

TD	transverse direction
TEM	transmission electron microscope
TMP	thermomechanical processing
TTT	temperature-time-transformation
UTS	ultimate tensile strength
UV	ultraviolet
VAR	vacuum arc remelting
WQ	water quench
wt	weight
XRD	x-ray diffraction

Symbols

A	reduced section length
B	build session
D	gauge diameter
D	BOR rotation matrix
d	laser spot diameter
D_1	island side length
E	Young's modulus
E_L	energy density
E_p	potential energy
G	anneal group or gauge length
H	horizontal orientation
h	laser hatch spacing
HV	Vickers micro-hardness
I	laser irradiance
K_c	crystal reference coordinate system

K_s	sample reference coordinate system
L	sample total length
M_f	martensitic finish temperature
M_s	martensitic start temperature
q	laser heat flux
r	laser beam radial distance
r_o	laser beam radius (constant)
T	test session
V	laser velocity
V	voltage
α	alpha phase (also primary alpha)
β	β phase
γ	angle of crystal misorientation
ρ	density fraction
σ	stress
α’	alpha prime phase (HCP martensite)
α’’	alpha double prime phase (orthorhombic martensite)
β’	β phase precipitate
σ_0	material constant
σ_y	yield stress

LIST OF FIGURES

Page

LIST OF TABLES

Page

1. INTRODUCTION

Additive manufacturing (AM) is seen by some as the 'next industrial revolution' and was ranked as one of 2013's ground-breaking technologies by *MIT Technology Review* (Ford, 2014). Additive manufacturing (commonly known as 3-D printing, but also referred to as: additive fabrication, additive processing, additive layer manufacturing, direct digital manufacturing, rapid prototyping, rapid manufacturing, layer manufacturing and solid freeform fabrication), is defined by the American Standard Testing Method International Committee F42 on Additive Manufacturing Technologies, as "*the process of joining materials to make objects from Computer Aided Design (CAD) model data, usually layer upon layer, as opposed to subtractive manufacturing methods.*"

AM is a fast-growing industry. Osakada and Shiomi (2006) stressed that a core driving force behind the current growth in AM is the global competition between companies in industry to improve manufacturing processes and speed up the product development cycle. A key turning point leading to the current fast-paced growth of AM commercially was the expiration of early AM machinery patents. This allowed for the technology to be used and developed by a larger group of people and thereby grow the industry.

AM makes sense from a business perspective and indicators of future growth of AM include: increasing sales, technology advances and new applications (Ford, 2014). The aim of any business is to make profit and increase profit annually to grow and expand the business. Profit can, however only be enlarged by increasing income or reducing expenses. Global industry leaders in manufacturing, such as General Electric (GE), Boeing and Airbus have successfully implemented the novel manufacturing technique of AM to benefit from the various advantages it offers and to ultimately cut costs. These advantages include: low to no material waste, no tooling requirements, shorter lead times for replacing single components in an assembly, as well as fewer resources needed for manufacturing.

The core motivation for the use of AM as a substitute to conventional manufacturing routes in industry (such as casting, metal forming, shaping of polymers, material removal processes through automated milling/turning/drilling) is long term cost saving. Cost saving in industry, through the AM route, is however application specific. AM has been majorly successful in environments where low-volume, complex or customised parts are required (such as customer-specific medical implants). AM is a low-scale production process, focused on customisation. It allows for responsive production, shorter supply chains, democratisation of production and optimised design. (Royal Academy of Engineering, 2013).

Customisation using conventional manufacturing routes is extremely expensive and time consuming due to the resources and manufacturing tools that are required. AM is a long-term low-cost solution to customise parts since the only physical resources needed to manufacture the end/net-shape part is: a computer with the required software, a 3D printer and the material from which the part is to be made.

Apart from the advantages AM brings to the manufacturing industry, it also has positive social impacts. AM is a sustainable manufacturing method and due to freedom of design it offers, optimisation of material and structural strength (using mathematical optimisation techniques such as topology optimisation), is possible. AM has revolutionised the design approach for both large industry companies and smaller start-up companies.

1.1. BACKGROUND

1.1.1. Metal additive manufacturing

Additive manufacturing (AM) of metal parts is the newest branch of manufacturing techniques falling in the group of powder metallurgy (PM). Whereas the conventional PM processing technique involves applying high pressure and temperature to a die containing fine metal powder, the metal additive manufacturing (MAM) process is essentially a solidification process in which powder is melted with either a laser or electron beam. MAM is therefore an alternative to traditional metal manufacturing such as forging or casting.

Selective Laser Melting (SLM) is the chief AM technique used to produce high-precision metallic parts. SLM is a 'micro-welding' process which uses a laser to melt layers of powder to build a three-dimensional functional part.

1.1.2. Titanium as a material of choice

Titanium and titanium alloys are the material of choice for many critical, light weight structural components and are becoming increasingly popular in the aerospace industry. Titanium is the choice of material for many critical aircraft components such as the compressor blades in aircraft engines. While the strength of titanium alloys is comparable to steels (400 – 1500 MPa), titanium's major advantage over steels is that it is half the weight of steel and an excellent corrosive resistant material.

This makes its application in the chemical and petrochemical industries of great value. Titanium is also used in components of deep-sea oil wells due to the combination of properties mentioned. In terms of non-industrial application, titanium is a popular chose of material for the use in golf clubs, tennis rackets and bicycles. Titanium has also seen application in architecture, jewellery and outdoor equipment. Lastly, titanium is the material of choice for medical bone implants due to its biocompatibility, light weight and strength.

The most popular titanium alloy (the 'workhorse' of the titanium industry) is Ti6Al4V. This alloy is made up of 6 weight (wt) % aluminium, 4 wt % vanadium and balanced with titanium wt %. It accounted for 45 % of total weight of all titanium alloys shipped in the last half-century and 50 % of commercial share of Ti-alloys in industry (Donachie, 2000).

1.1.3. Selective Laser Melting-produced Ti6Al4V

Due to Ti6Al4V popularity, it has also become a main Ti-alloy used in the process of MAM. Apart from the mentioned advantages of both the material and process, the porous surface inherent to the manufacturing of SLM-produced Ti6Al4V has been found to be advantageous in osseointegration due to the strong interlocking of surrounding bone tissue with the titanium implant (Xue *et al.* 2007). SLM-produced Ti6Al4V is also advantageous for producing lightweight components, for application in the aerospace industry, in a relatively short time.

Concern has been raised, however about the achievable mechanical properties and part density of SLM-produced Ti6Al4V components. This forms the foundation for the current project motivation. The project motivation will now be discussed in detail.

1.2. MOTIVATION

Questionable part dense parts in SLM-produced Ti6Al4V is a common shortcoming resulting from the process. Inferior part density is caused by micro-pores that result from non-optimal process-related parameters. These defects have been argued to deteriorate part ductility and fatigue (Kruth *et al.* 2010). Achievable density has been improved through optimising the SLM process parameters of: laser speed, laser power, scan strategy, laser spot size and hatch spacing. Although the development of optimised process parameters to achieve high-density parts (near-full dense >99 %) has been successful, the achievable ductility of as-produced parts is still much less than it's wrought counter-part. It has largely been accepted that a post-process heat treatment is required to improve part ductility to qualify SLM-produced Ti6Al4V for application in industry.

Industrial post-process heat treatments, which are typically used to alter wrought Ti6Al4V microstructure with the aim of improving tensile performance (strength, toughness, and ductility), do not directly apply to SLM-produced Ti6Al4V. The starting crystallographic microstructure of SLM-produced Ti6Al4V is significantly different to that of its wrought counterpart. Microstructure formed through the process of SLM is an ultra-fine metastable microstructure, while wrought Ti6Al4V microstructure is a stable, course microstructure. As such, ductility values of post-heat-treated SLM-produced Ti6Al4V have been reported significantly lower than its wrought counterpart and below the requirements set by some standards (such ASTM F1472-08) (Yan and Yu, 2015).

Investigation into various heat treatments have been done by various authors such as (Vilaro, Colin and Bartout, 2011; Knowles, Becker and Tait, 2012; Vrancken *et al.* 2012; Huang *et al.* 2015; Wauthle *et al.* 2015), however differences in results and post process parameters required further research into the optimal annealing strategy. This furthermore highlights the lack of existing standard practises in the manufacturing process of SLM-produced Ti6Al4V components.

Interest in the research exists in both academic and industrial settings. Commercial interest exists in the field by major aerospace companies such as Airbus and Boeing. Academic interested parties for this project include the Department of Science and Technology (DST) and the Centre for Scientific and Industrial Research (CSIR).

The study forms part of a collaborative effort initiated by the DST to qualify SLM-produced Ti6Al4V for the biomedical and aerospace industries. The project is motivated by the shortcoming of SLM-produced Ti6Al4V's mechanical properties and the lack of research to date on the process and resulting part quality of SLM-produced Ti6Al4V. The project aims to gain a fundamental understanding of the influence of annealing strategies on of the microstructure of SLM-produced Ti6Al4V to improve and optimise the tensile properties of the material.

Major potential in SLM-produced Ti6Al4V exists in South Africa. While South Africa is the second largest supplier of titanium ore globally, it is currently limited to the production of raw material for exporting (only) since it lacks the adequate infrastructure to process the material. Finished titanium product is therefore imported at high cost. By developing SLM of Ti6Al4V, the economic value of titanium as a finished (processed Ti) product can be utilised and thereby contribute to socio-economic development of the country.

1.3. PROJECT OBJECTIVES

Project objectives are formulated to achieve the set aim. Project objectives are to:

- Carry out an in-depth literature review with focus on understanding the metallurgy, crystallography and phase transformation of Ti6Al4V and SLM-produced Ti6Al4V microstructure
- Measure sample density of SLM-produced Ti6Al4V and evaluating the nature of micro-defects
- Design and implement a wide range of heat treatment strategies
- Analyse the microstructure of SLM-produced Ti6Al4V in its as-fabricated and annealed state
- Determine tensile behaviour of as-fabricated and heat treated samples
- Analyse tensile and microstructural data
- Link heat treatment strategies to microstructure as well as microstructure and tensile behaviour
- Conclude and make recommendations

1.4. SCOPE

The scope of the thesis is focused on investigating the unique metallurgy and the tensile properties of SLM-produced Ti6Al4V. In-depth investigation of microstructural morphologies and the kinetics of phase transformation is done. The

scope furthermore comprises of investigating the mechanical and material properties of SLM-produced Ti6Al4V using standard testing procedures. Lastly, important links/couples between microstructure and mechanical properties are studied to formulate important conclusions regarding process-structure links and structure-property links that are needed in the development and qualification of the technology. In-depth investigation into dislocation and plastic deformation is outside the scope of the project.

1.5. THESIS OUTLINE

Chapter 2 reviews literature that is relevant and required for fundamental understanding of concepts covered in the thesis. This chapter first considers the metallurgy of the titanium and its alloys and then microstructural transformations of Ti6Al4V. Traditional process methods follow in which standard heat treatment processes and strategies are reviewed. AM is reviewed with focus on SLM. The literature review ends with a review of methods of microstructural analysis.

Chapter 3 sets out the experimental methodology followed to achieve the project objective. These include the process description of the SLM machine used, the design of the samples, powder analysis, density measurements, heat treatment strategies, micro-hardness measurements, microstructure analysis and tensile tests.

Chapter 4 presents the results of experimental work done. This chapter has been divided into: optical images of the effect of an observed printing error, the resulting density of builds from three build sessions, optical microstructure analysis, electron backscatter diffraction microstructure and texture analysis, and lastly, tensile results and property correlations.

Chapter 5 discusses the results in detail as well as the underlining likes between results of microstructure and heat treatments, and links between microstructure and tensile behaviour.

Chapter 6 formulates the conclusions through reiterating the project aim and summarising the findings. Recommendations are made for improvements to methods used and future study direction that would further benefit the research field.

2. LITERATURE REVIEW

This chapter revises fundamental concepts and research findings that concern key knowledge areas of SLM-produced Ti6Al4V. Chapters are assigned to the fundamental knowledge areas of the thesis research topic: The metallurgy, crystallography and transformation kinematics of the material, traditional processes, and the process of AM with focus on SLM and finally the methods/tools of microstructural analysis.

2.1. TITANIUM AND TITANIUM ALLOYS

The physical and chemical properties of titanium and its alloys are discussed in this chapter with attention given to the (α+β) Ti alloy: Ti6Al4V. Specific attention is given to parameters that influence microstructure morphology and mechanical properties such as phase- and alloy equilibrium wt % and crystal structure of relevant micro-constituencies. The microstructures and their formation through solid-state phase transformation are discussed in a separate chapter due to its key importance in the context of the thesis.

2.1.1. Physical metallurgy

Pure titanium (elemental titanium also termed commercially pure Ti) is an allotropic metal that can take the form of two different crystal structures depending on the state of temperature and pressure. Upon heating (at atmospheric pressure), titanium undergoes a solid-state phase transformation at 882.5 ºC (called the transus temperature) in which the α phase hexagonal close-pack (HCP) crystal structure, Figure 2.1(a), transforms into a β phase body centred cubic (BCC) crystal structure, Figure 2.1(b) (Lütjering and Williams, 2007). Titanium melts at 1668 ºC upon heating and solidifies at 1725 ºC (solidus) upon cooling from its liquid state. Further physical and mechanical properties of elemental Ti are summarised by Donachie (2000: 5) and Lütjering and Williams (2007).

Alloying

Titanium is alloyed to improve its physical and mechanical properties. This is possible by allowing the β phase to exist at room temperature and thereby allowing an improvement in material in terms of workability and mechanical properties. When titanium is alloyed with metallic elements, the transformation temperature is no longer fixed, as varying percentages of both phases can exist in equilibrium at an elevated temperature.

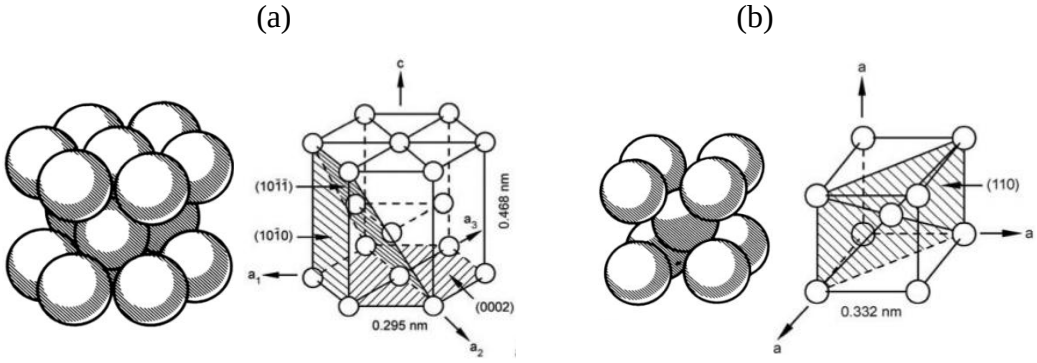

Figure 2.1: (a) Hexagonal close packed (HCP) crystal unit cell (b) body centred cubic (BCC) crystal unit cell. Left: spherical atomic model (Donachie, 2000) Right: axis conventions, planes and lattice distances (Lütjering & Williams, 2007)

Alloying elements are classified based on whether they stabilise the α phase or the β phase. In other words, allowing the phase to exist in an equilibrium state at a specific temperature without undergoing phase transformation. α stabilising elements cause the transus temperature to increase (more energy is needed to transform the stabilised α phase) while β-stabilising elements cause the transus temperature to decrease (less energy is needed since the β-stabilising element 'aids' the transformational process to the β phase).

α stabilizing alloy additions tend to be simple metals such as Al, Ga, Ge, and Sn (substitutional) and non-metals O, C, N (interstitial). Oxygen is a very effective (sometimes unwanted) α stabiliser that is always present in titanium alloys to some degree. Typically, very pure Ti will have an oxygen level of around 500 parts per million weight (ppmw), whereas heavily oxygen enriched alloys will have up to 2500 ppmw oxygen (Dye, 2015). β-stabilising elements are transition, refractory and noble metals. A comparison of the stabilising effect of different β-stabilising elements can be made through the so-called molybdenum equivalence (Stráský, 2014):

$$[Mo]_{eq} = [Mo] + 0{,}67\,[V] + 0{,}44\,[W] + 0{,}28\,[Nb] + 0{,}22\,[Ta] + 2{,}9\,[Fe] + 1{,}6\,[Cr] + 1{,}25\,[Ni] + 1{,}7\,[Mn] + 1{,}7\,[Co]. \quad (1)$$

This chemical balance shows that vanadium content must be at least one and a half times that of molybdenum to achieve the same β-stabilising effect. Iron is three times stronger at stabilising β than Mo and four times stronger than V. It must be noted that the molybdenum equivalence is an empirical rule based on analysis of binary alloys and therefore cannot be used to calculate β-transus temperatures or equilibrium phase composition. An analogy to the molybdenum equivalence for the α-stabilising alloys is the Al equivalence (Stráský, 2014):

$$[Al]_{eq} = [Al] + 0{,}33\,[Sn] + 0{,}17\,[Zr] + 10\,[O + C + 2N] \quad (2)$$

It is important to note the high stabilisation effect of oxygen, carbon and nitrogen. Oxygen is ten times stronger in α-stabilisation than aluminium. Electronic and thermodynamic theories for α and β phase stabilization have been studied by Boyer, Collings and Welsch (1994).

2.1.2. Titanium alloys classification

Titanium can be alloyed with a range of α and/or β-stabilising elements which subsequently allow titanium alloys to take on a α or β or a combination of both phases, in an equilibrium condition at room temperature. Ti alloys are therefore classified to belong to one of three broad groups: α , β- or (α+β)-alloys, depending on their equilibrium phase constitution at room temperature after processing.

Ti alloys composed of stabilising elements which cause them to lie near the α → (α+β) or the β → (α+β) transi temperatures (represented by the solid curves on Figure 2.2) at room temperature, are classified as near-α or near-β, respectively. Commercially pure (CP) Ti is classified as an α alloy due to the unavoidable presence of interstitial impurities: O, C, N, and H and the substitutional impurity, Fe (Kelly, 2002: 6). Pure Ti or α-Ti alloys are considered the most corrosive resistant and most weldable of the Ti-alloys. They cannot, however be heat treated to improve mechanical properties (such as ductility) since cooling from the β phase would transform back into a fully α-Ti microstructure.

Classification of common Ti-alloys is compared schematically on the popular pseudobinary β-isomorphous phase diagram in Figure 2.2(a). This figure indicates the four common Ti-alloy classifications: α-Ti, (α+β)-Ti, metastable β-Ti and stable β-Ti. Common alloys and where they lie within their classification groups are depicted in this figure. Broken lines labelled 'M_s' and 'M_f' indicate martensite start- and finish temperatures respectively.

Discussion of the properties and attributes of α-Ti and β-Ti alloys as well as near α-Ti and near β-Ti alloys, are outside the scope of the thesis and can be found in work by various authors such as Donachie (2000), Lütjering and Williams (2007) and Boyer, Collings and Welsch (1994).

Auxiliary / descendant phases

While α-and β phases are defined according to their different crystal structures (HCP and BCC respectively) each has its own group of descendant or auxiliary phases. The auxiliary phases that pertain to the scope of the thesis are: α', α'', α_2 and β'. Each phase's respective starting temperature with respect to β-stabilising wt % is represented by the labels curves on Figure 2.2(b). The process by which these phases form is called phase partitioning. Phase partitioning occurs due to elemental diffusion and phases are either identified per their distinguished elemental composition or crystal structure. These phases are distinguished from parent α and β phases through the addition of either an apostrophe or subscript to the representative symbol.

(a)

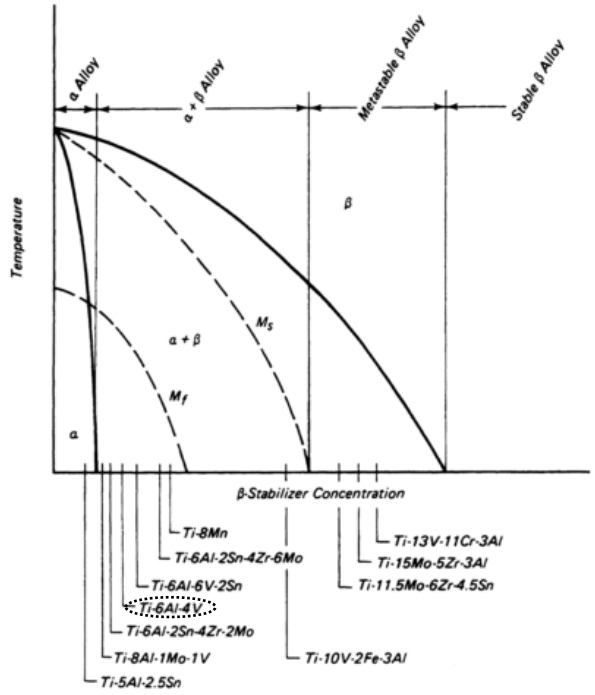

(b)

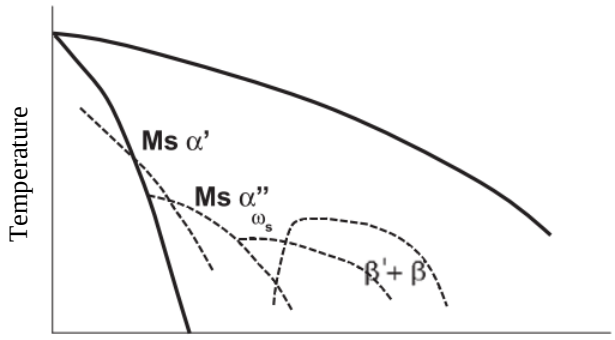

Figure 2.2: (a) β-isomorphous diagram divided into alloy classifications and comparing commercial β stabilised alloys (Donachie 2000: 13) (b) A schematic of the β-isomorphous phase diagram of metastable products and their respective phase fields (Banerjee and Williams, 2013)

Metastable martensites – α' and α''

These metastable phases form through a diffusionless transformation upon fast cooling such as quenching, welding or SLM. This transformation is almost instant and therefore considered independent of time. Whereas α and β phases form through nucleation and 'slow' diffusion, martensite forms through the simultaneous mass movement of atoms in a shear-like motion. This causes the martensitic phase in Ti6Al4V to essentially have the same wt % as the initial alloying percentage, i.e. ~6 % Al and 4 % V. The formation and decomposition of these phases are critically important to the scope of this thesis and are therefore discussed in more detail in Sections 2.5 and 2.6.

Titanium-aluminium Precipitate (α_2)

Ti_3Al is an intermetallic compound that precipitates during long holding times (8 - 24 hours) in the presence of more than 5 wt % Al and at a temperature of between 500 º to 550 ºC (Lütjering, 1998). These particles are hexagonal in structure ($D0_{19}$ superstructure), Figure 2.3. The precipitation of this ordered second phase within the primary alpha phase is a form of precipitation hardening (Stráský, 2014). This has a strengthening effect on the α phase. Lattice parameters for this compound are: a = 5.765 Å and c = 4.625 Å (Karkina and Yakovenkova, 2012).

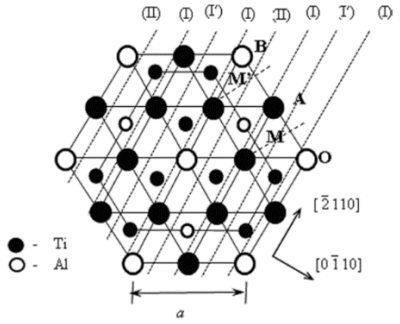

Figure 2.3: Projection of the unit cell of the Ti_3Al crystal structure onto the basal plane (Karkina and Yakovenkova, 2012)

In order to avoid too much precipitating of Ti_3Al particles, the aluminium content in most Ti alloys are limited to a maximum of 6 wt % (Lütjerinag & Williams 2007: 25). Although these participates are incredibly hard to see under optical microscope and SEM, their effect on microhardness can be measured. Annealing at this temperature range is called age-hardening and is usually the last step in annealing process.

Vanadium enriched precipitate (β')

β'-phase is classified as a phase that is rich in a β-stabilising alloying element. While it is commonly observed in metastable β-alloys, precipitation has been observed in (α+β)-alloys too. Figure 2.4(a) and (b) show SEM micrographs of observed β' formed during MAM. Chlebus *et al.* (2011) proposed that their formation was due the inherent reheating of each layer and the subsequent decomposing of α'/α''. The precipitates grow along grain boundaries as temperature is elevated as observed by Sallica-Leva *et al.* (2016) as depicted in Figure 2.4(c).

(a) (b) (c)

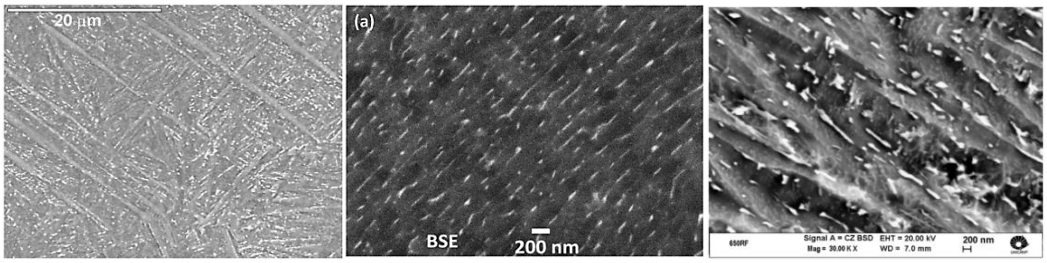

Figure 2.4: (a) SEM images of vanadium rich precipitates (white particles) in as-build SLM Ti-6AL-7Nb (Chlebus *et al.* 2011: 491), (b) of as-built EBM Ti6Al4V (Lu *et al.* 2016: 307) (c) SLM Ti6Al4V sample heat treated at 650 ºC for 2 hours (Sallica-Leva *et al.* 2016)

2.2. TI6AL4V METALLURGY

Ti6Al4V gives the best combination of mechanical properties balancing both strength/stiffness (attributed to the α phase which is solid solution strengthening with by Al) and ductility/toughness (attributed to the β phase). Formability is improved at high temperatures near the β-transus due to the high percentage of ductile β phase.

The Young's modulus and microhardness of Ti6Al4V have been calculated from the phase constitution of the alloy using the rule of mixtures. These values are tabulated in Table 2.1.

Table 2.1: Theoretical properties of Ti6Al4V phases (Crespo 2011: 326)

Phase	**α**	**β**	**α'**
Young's modulus [GPa]	117	82	114
Vicker's microhardness [HV]	320	140	350

Ti6Al4V, like all Ti-alloys are non-toxic and bio-compatible (although, vanadium and aluminium on their own are toxic). In cryogenic applications, interstitial alloy element percentages need to be carefully controlled to improve ductility and fracture toughness.

Extra-low interstitial (ELI)

Alloys in which careful control is maintained to reduce interstitial elements (oxygen, nitrogen and carbon) are designated extra-low interstitial (ELI) and are generally a tougher, more ductile form of Ti6Al4V (at the cost of yield strength). Ti6Al4V ELI is given the designation: Grade 23. These alloys generally contains 0.08 – 0.11 wt % oxygen and 0.01 wt % nitrogen as opposed to regular Ti6Al4V

which contain 0.18 - 0.19 wt % oxygen and 0.015 wt % nitrogen (Boyer, Collings and Welsch, 1994; Lütjering and Williams, 2007).

The standard specification for wrought Ti6Al4V ELI alloy for surgical implant applications, (ASTM F1472-08, 2008), require the elemental composition of powder to be as tabulated in Table 2.2. For a comparison to powder manufactured for MAM, the elemental composition of Ti6Al4V ELI powder, manufactured for Electron Beam Melting (EBM), is tabulated in Table 2.3.

Table 2.2: Required elemental composition for Ti6Al4V ELI per ASTM F136

Element	**Al**	**V**	**C**	**Fe**	**O**	**N**	**H**	**Ti**
[wt %]	5.5-6.5	3.5-4.5	< 0.08	< 0.25	< 0.13	< 0.05	< 0.012	Balance

Table 2.3: Claimed typical elemental composition of ARCAM Ti6Al4V ELI powder (Arcam, 2016)

Element	**Al**	**V**	**C**	**Fe**	**O**	**N**	**H**	**Ti**
[wt %]	6.0	4.0	< 0.03	< 0.1	< 0.10	< 0.01	< 0.003	Balance

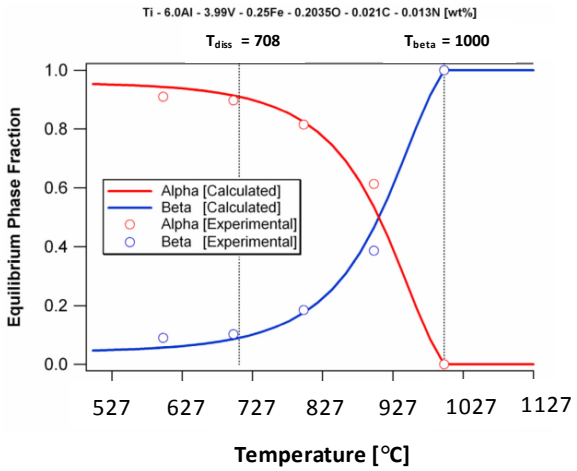

Figure 2.5: Equilibrium phase fractions at elevated temperatures by *ThermoCalc* simulation (T_{diss}– dissolution temperature, T_{β}– β-transus) adapted from (Kelly, 2004)

Ti6Al4V and Ti6Al4V ELI: phase and elemental percentage composition

The wt % of phases (α and β) in Ti6Al4V and Ti6Al4V ELI is fundamental in both the transformational characteristics and mechanical properties of the material. The

wt % of respective phases as a function of temperature and alloy elemental composition is discussed.

Increase in wt % of β-stabilising element lowers the β-transus temperature due to its diffusional characteristic from the β to α phase as the alloys is cooled. The alloy's composition (in wt % V or Al) influences the phase percentage of β in the alloy at room temperature (or any arbitrary temperature). During diffusional phase transformation, Al diffuses from the β phase to the α phase while at the same time; the Vanadium diffuses from the α phase to the β phase, until an equilibrium composition is achieved.

Elmer *et al.* (2004) measured the phase fraction of β in wrought (fully equiaxed microstructure) Ti6Al4V to be 12 %. (Chemical composition of the material was: 6.0 Al, 4.2 V, 0.11 O, 0.17 Fe, 0.0028 H, 0.014 C, 0.009 N, 0.03 Si, bal. Ti by wt %). Ti6Al4V phase percentage as a function of temperature was calculated by Kelly (2004) and is depicted in Figure 2.5.

Seshacharyulu *et al.* (2000) observed that at a temperature range of around 920ºC equal volume fractions of the two phases exist. An increase in ductility beyond 920º is caused by a rapid increase in the β volume fraction above 920 ºC.

Alloy elemental composition concentrations

Individual alloy constituency of the phases was measured by Elmer *et al.* (2004: 8329) of an equilibrium Ti6Al4V microstructure at room temperature. Results thereof are tabulated in Table 2.4. It should be noted that the β phase is stabilised by a wt % of ≥15wt % V, as indicated in Table 2.4. This correspond to β-Ti alloys which require this wt % (out of total alloy weight) of β-stabilising element to retain their β phase when quenched from above the β-transus (for example the alloy Ti-2Al-15V would be considered a stable β-alloy).

Table 2.4: Chemical composition of the α and β phases of an wrought Ti6Al4V sample measured by microprobe analysis (Elmer *et al.* 2004)

	Al [wt %]	**V [wt %]**	**Fe [wt %]**	**Ti [wt %]**
Nominal composition	6.2	4.0	0.17	92.5
β phase	2.92 ± 0.11	15.43 ± 0.86	1.32 ± 0.11	80.7 ± 0.7
α phase	6.73 ±0.33	1.42 ± 0.73	0.04 ± 0.02	91.2 ± 0.47

Elmer *et al.* (2005) furthermore simulated the theoretical alloy composition of elements in α and β as a function of temperature. Figure 2.6(a) illustrates the swop in β composition of V at low temperature and Ti at high temperatures.

Figure 2.6(b) illustrates that while the change in V mole % is minor and α reaches a maximum at about 750 ºC, V mole % in β changes drastically with a change in temperature.

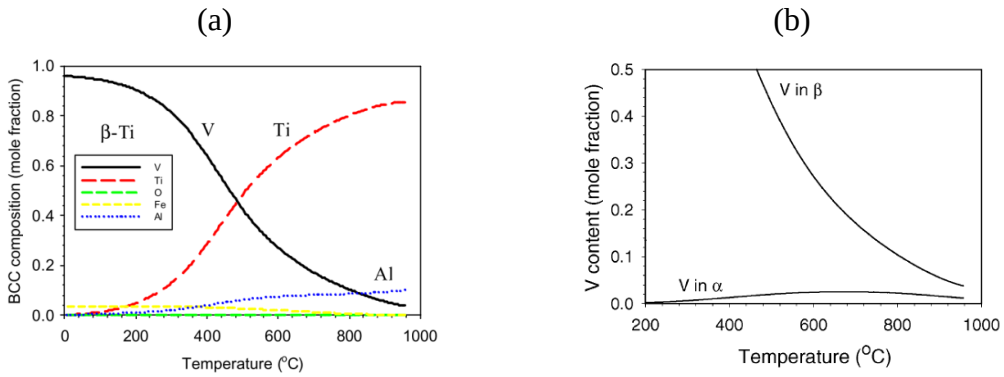

Figure 2.6: *ThermoCalc* simulation of theoretical mole fraction of elements as function of temperature of (a) all elements in β (b) vanadium content in α and β (Elmer *et al.* 2005)

In order convert between mole fraction and wt % (for sake of comparison to previous discussions), the mole fraction (or atomic fraction) of alloy elements in phases can be calculated through:

$$X = wt\%(i)\frac{M_{total}}{M_i} \qquad (3)$$

Where M_i is the molecular mass of the element (50.942 g/mol for V), and M_{total} is the total molecular mass of the system (45.86 g/mol for Ti6Al4V).

2.3. TI6AL4V CRYSTALLOGRAPHY

Due to the anisotropic nature of the HCP crystal (as will be discussed), mechanical properties are heavily dependent on microstructure morphology and crystallographic texture.

2.3.1. Crystallographic inheritance

A single crystal plane is indicated with '( )'-brackets and a family of planes with '{}'-brackets. A vector direction is indicated with '[ ]'-brackets and directional family is indicated by '< >'-brackets.

The existence of a fixed crystallographic transformation relationship between a HCP crystal structure forming from the BCC structure on cooling was first published by Burgers (1934). The Burgers Orientation Relationship (BOR), as it has become widely known, describes the crystal orientation relationship between the HCP α phase and the BCC β phase.

The BOR states that the formation of the HCP α phase will be such that any basal crystal plane (0 0 0 1) is parallel to that of any of the 6 planes in the BCC {1 0 1}

family, depicted in Figure 2.7 and Figure 2.8. Furthermore, any one of the vector directions in the family of BCC $< 1\ 1\ 1 >$ lies parallel to one of the $< 2\ \bar{1}\ \bar{1}\ 0 >$ vector direction in the HCP crystal. Since there are six {1 0 1} planes in any BCC unit cell and two $< 1\ 1\ 1 >$ direction in each of these planes, a total of 12 distinct α-variants could form from within a single BCC β grain. Simply put: a prior-β grain can have a total of 12 unique HCP crystal orientations which strictly follow that of the BOR.

2.3.2. α variants and grain boundary angles

A combination of any 12 variants gives a total of 12x12=144 possible grain boundary formations of α crystals. Out of the 144, 132 combinations are considered high angle grain boundaries (HAGB) and 12 are considered low angle grain boundaries (LAGB). The orientation matrix of each variant (1-12) calculated from a single β orientation is attached in Appendix I.4.

Usually not all 12 variants are present in a single prior β grain. The process of preferential existence of variants is called variant selection and has been studied extensively (Wang, Aindow and Starink, 2003; Shi and Wang, 2013; Qiu *et al.* 2015; Li *et al.* 2016).

Of the twelve variants, five different angles (excluding 0 º) can form between a pair of α grains. Variant types are defined by variants that share the same rotational axis and angle pair from a reference orientation (variant 1). Variant types of I-V and their crystallographic properties are included in Appendix I.4.

A misorientation histogram of all α crystals in a Ti6Al4V sample are plotted in Figure 2.9(a). The peak frequencies and their relative magnitude reflect the percentage of HAGB possible at the respective misorientation angles. Random, evenly distributed 'noise' misorientation that fall between these peaks are due to α-pairs that form from the boundaries of two different β grains. These boundaries can therefore be used to identify (and reconstruct) prior-β grain boundaries. Prior-β grain boundaries identified due to random HAGB's are depicted in Figure 2.9(b) by the black lines.

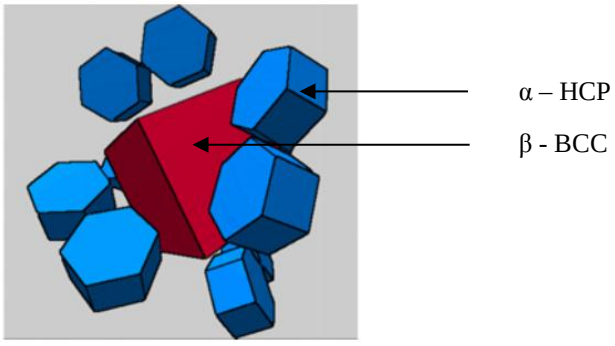

Figure 2.7: 3D depiction of the BOR (Cayron, 2008: 517)

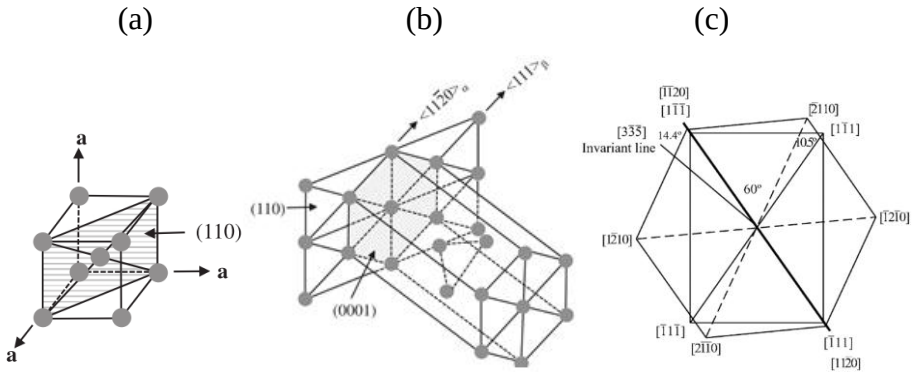

Figure 2.8: Burgers orientation relationship crystallography: (a) One of the six BCC planes in the BOR (Beladi, Chao and Rohrer, 2014: 479) (b) Superimposed BCC plane and a HCP crystal orientated with each other in terms of BOR (Bhattacharyya *et al.* 2003: 4690) (c) 2D geometry of BOR i.t.o. relative crystal directions and angles

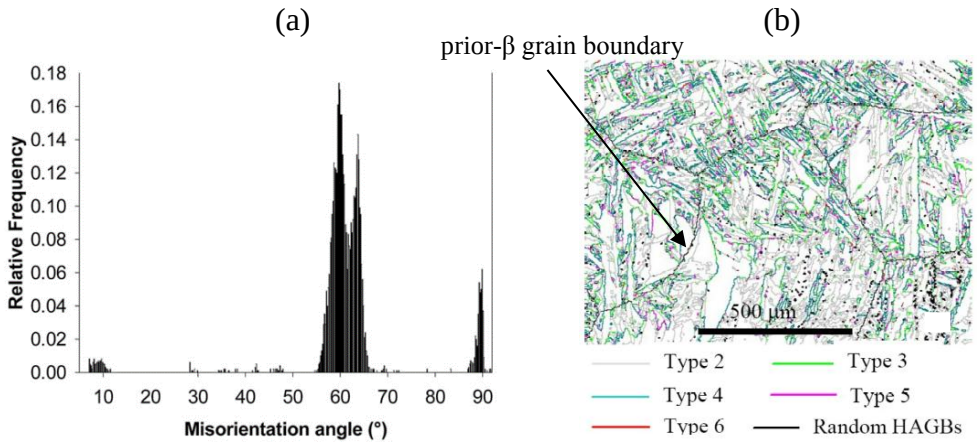

Figure 2.9: (a) Frequency vs orientation angle between of α grains. (b) Colour overlay plot of various misorientation types. Black misorientation lines coincide with prior-β grain boundaries (Wang *et al.* 2012)

2.3.3. HCP crystal properties

Mechanical properties of the HCP crystal are the fundamental building blocks determining strength and ductility of Ti and Ti-alloys. It is well established that yielding of metal structures is due to the applied force exceeding the overall critical resolved shear stress (CRSS) of the atom bonds in a crystal slip system. The ease at which theses slip systems can move in a structure depends, among other, on the CRSS of a slip system and relative angle between applied load and the slip plane (Schmid factor).

The strength of a metal is due, in part, to the number of slip systems in the metal's crystal structure. HCP slips systems are illustrated in Figure 2.10(a). The total

number of slip directions is indicated by the separate number. The CRSS of each slip system varies as a function of temperature as depicted in Figure 2.10(b).

Titanium's HCP crystal structure is highly anisotropic. It is in fact the highest anisotropic metal from a range of metals HCP metals. Anisotropy factors, f_E and f_G for a range of HCP metals are depicted in Appendix I.5 and are calculated from elastic compliance constants (the values of which are also included in Appendix I.5) (Tromans, 2011):

$$f_E = S_{11}/S_{33} \tag{4}$$

$$f_G = (S_{44} + 2S_{11} - 2S_{12})/\, S_{44} \tag{5}$$

The theoretical Young's modulus for a randomly orientated Ti polycrystalline is 114.6 GPa. Larson and Zarkades (1974) investigated the texture dependency of α-Ti and showed that the Young's modulus perpendicular to the C-axis is 100 GPa

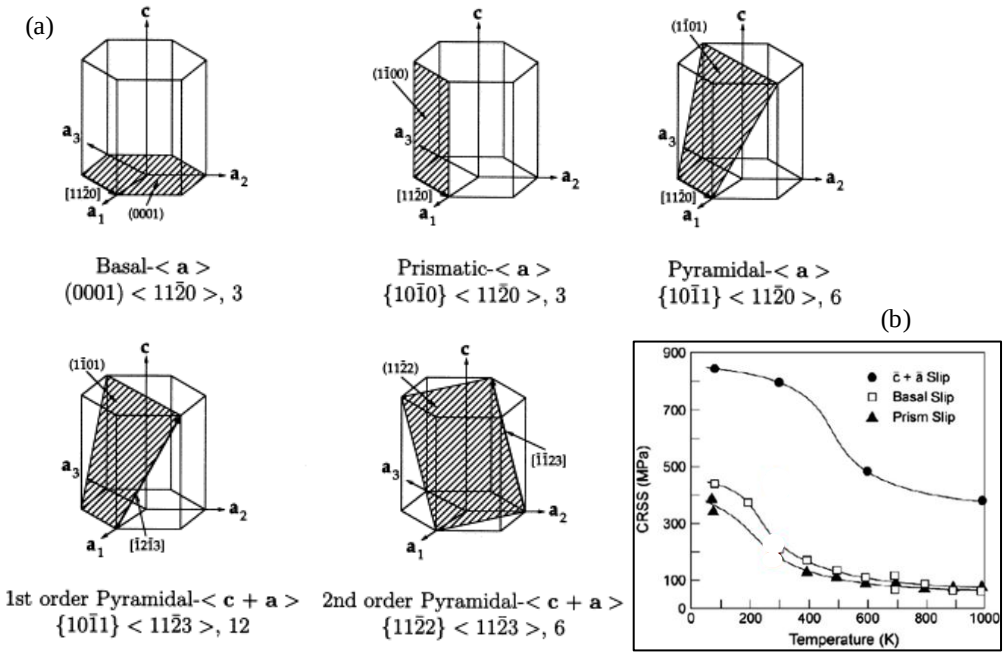

Figure 2.10: (a) Slip systems in HCP structure: (Balasubramanian & Anand, 2002). (b) Critical resolved shear stress(CRSS) vs temperature of Ti-HCP crystal slip systems. Adapted from Banerjee and Williams (2013)

compared to 145 GPa parallel to the C-axis. A study by Tromans (2011) found these values to be 104 GPa and 146.2 GPa respectively.

This dependency of mechanical properties on orientation can be tailored to strengthen parts in a preferential direction by thermomechanical processing (TMP).

Working the material causes the HCP crystals to assume a preferential orientation (due to preferential slip systems in the HCP crystal) and thus texture. This process and the effect of TMP on tensile behaviour of Ti-HCP is discussed in Chapter 2.9.

2.4. PHASE TRANSFORMATION DURING COOLING OF TI6AL4V

Through fundamental understanding of phase transformation in Ti6Al4V, heat treatment strategies can be manipulated to bring about a superior microstructure and therefore superior mechanical properties. The kinetics of phase transformation is governed by a complex set of thermodynamic and diffusional physics. Key aspects thereof will be discussed.

Phase transformation during cooling from the β phase can occur through one of two processes: diffusional and non-diffusional transformation. Diffusional transformation of $\beta \rightarrow (\alpha+\beta)$ results in a stable, dual-phase alloy, while the non-diffusional transformation results in martensite $\beta \rightarrow \alpha'/\alpha''$. The amount of diffusion depends on the cooling rate from β. If the cooling rate is slow, complete diffusion occurs, while if the cooling rate is too fast, not enough time is allowed for atomic diffusion and the martensitic transformation occurs. Martensitic transformation is described as mass lattice 'shearing' to the HCP crystal structure. Filip *et al.* (2003) determined the phases resulting from different cooling rates from the β phase as depicted in Figure 2.11.

Cooling rate ($K\ s^{-1}$)	Phase composition
	Ti–6Al–4V
48	$\alpha'(\alpha'')$
40	$\alpha'(\alpha'')$
18	$\alpha'(\alpha'')$
9	$\alpha + \alpha'(\alpha'')$
7	$\alpha + \alpha'(\alpha'')$
3.5	$\alpha + \alpha'(\alpha'')_{trace} + \beta$
1.2	$\alpha + \beta$
0.08	$\alpha + \beta$
0.04	$\alpha + \beta$
0.024	$\alpha + \beta$
0.008	$\alpha + \beta$
0.004	$\alpha + \beta$

Figure 2.11: Cooling rates from β phase and resulting phases (Filip *et al.* 2003: 86)

The following section gives an overview of transformation physics of stable nucleation followed by diffusional growth to an equilibrium phase and elemental composition at a set temperature. Understanding of this is applicable to post-process heat treatments.

Diffusional transformation occurs at slow to intermediate cooling rates that allow sufficient time for stabilising elements to diffuse (especially vanadium). The temperature-time-transformation (TTT) diagram in Figure 2.12 depicts the slow cooling process and the resultant microstructure. While the TTT diagram on Figure 2.12 is for illustration purposes, a more comprehensive TTT diagram for

Ti6Al4V has been modelled by Kelly (2004) (included in the Appendix K.1) and Murgau, Pederson and Lindgren (2012).

When cooled slowly from the β phase, Figure 2.12(a), α phase preferentially nucleates at β grain boundaries, Figure 2.12(b). α phase grows along grain boundaries (called grain boundary α) until the temperature has decreased low enough, Figure 2.12(c). At this temperature, α grains nucleate and grow in colonies perpendicular to the β grain boundary, Figure 2.12(d). Since a slow cooling rate causes grain growth. The rate of cooling from β will determine individual size, grain boundary-α thickness, and colony size.

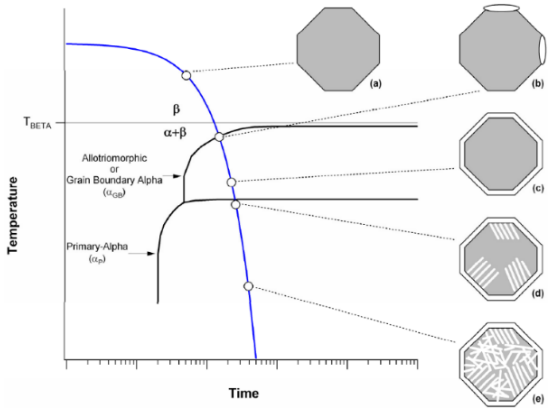

Figure 2.12: A schematic of diffusion controlled phase transformation during continuous cooling from the β phase to room temperature (Kelly, 2004)

(a) (b)

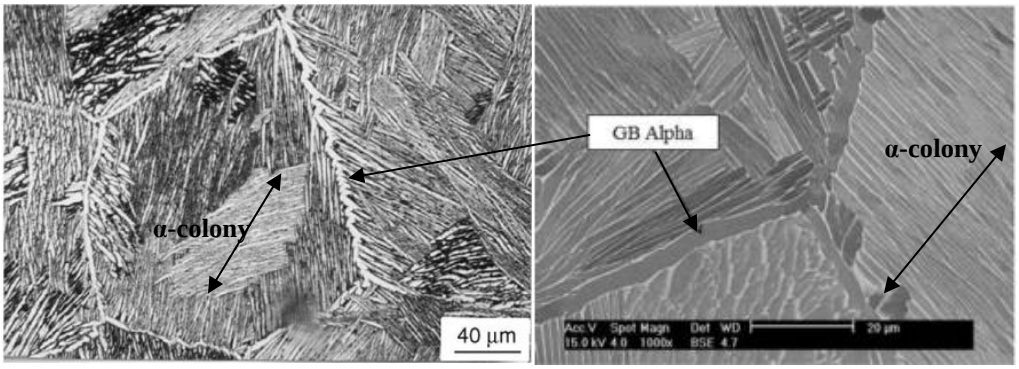

Figure 2.13: Microstructure resulting from slow cooling from β phase (a) micrograph including whole prior-β grain (Filip *et al.* 2003), (b) SEM image of grain boundary α and α colonies (Makiewicz, 2013)

When the cooling rate from β is at intermediate rate (such as air cooling), α-nucleation and growth starts to occur within the β phase instead of at the boundary. Resultant α grain size is much smaller and grains do not grow in colonies but rather in a unique 'basket weave' pattern, also termed the Widmanstätten texture, Figure 2.14.

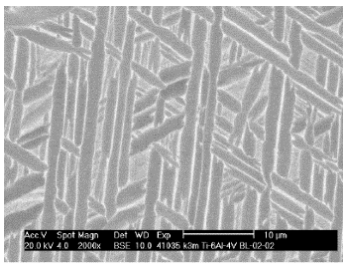

Figure 2.14: SEM images of microstructure resulting from intermediate cooling (air cooling) (Kelly, 2004)

The reverse transformation takes place upon heating, although the starting microstructure (α+β vs α'/α'') influences the nature of the transformation. Phase transformation of an equilibrium (α+β) microstructure occurs through diffusion without nucleation since the β phase is already present between α-laths.

If the starting microstructure is martensite, nucleation of β first occurs at α'/α'' boundaries and dislocation sites after which phase transformation occurs through simultaneous α'→β and α'→α transformation. This is further discussed in Section 2.6. Since martensite and its unique phase transformation occurs during annealing of SLM Ti6Al4V, the kinetics thereof is of great importance to the current research and is discussed in detail in the next section.

2.5. MARTENSITIC TRANSFORMATION

Titanium martensite is defined as a fine needle-like microstructure that forms upon rapid cooling such as water or oil quenching (athermal martensite), or by inducing an external stress (stress-induced martensite). Martensite forms through a displacive shear mechanism rather than atomic diffusion. This lattice shearing mechanism has been studied in detail by Wang, Aindow and Starink (2003). Martensitic transformation is considered independent of time (forms almost instantaneously) and is therefore simply characterised by start and finish temperatures (denoted as M_s and M_f, respectively) which signify the range in which the transformation takes place.

The start of α'/α'' formation is quoted at two conflicting temperatures in literature. While authors such as Kelly (2014), Sallica-Leva *et al.* (2016) and Lu *et al.* (2016) quote the M_s at ~800 ºC, authors such as Ahmed and Rack (1998) quote the temperature at 575 ºC. The decomposition of α'/α'' phase is also quoted to decompose at both these temperatures, as discussed in the next section.

Due to the non-diffusive nature of the formation of the HCP structure, the BCC β phase has a negligible presence in the phase constitution of the Ti6Al4V martensite. This, and its ultra-fine grain size, are key factors that determined as-produced SLM Ti6Al4V's high strength and low ductility properties. The extreme fineness of the laths directly translates to a high yield and ultimate tensile strength (UTS). This is due to the phenomenon of grain boundary strengthening (also called Hall-Petch strengthening). The Hall-Petch Relation is quantified by:

$$\sigma_y = \sigma_0 + \frac{k_y}{\sqrt{d}} \quad (6)$$

where σ_y is the yield stress, σ_0 the materials constant for the starting stress for dislocation movement, k_y the strengthening coefficient of the material and d the average grain diameter. A more specific Hall-Petch relation which takes into account dislocation density and partitioning dimensions has been used by Murr, Esquivel, *et al.* (2009).

The understanding of the martensitic transformation mechanisms is limited due to the difficulty in in situ observation of the transformation due to its incredible speed. Nonetheless, a study of the crystal texture and orientation characteristics of the microstructure will aid in understanding the formation of the structure.

There are two types of metastable martensite structures that can form: α' - which has a HCP crystal structure, and α'' - which has an orthorhombic crystal structure, Figure 2.15. Whereas the width of α' was measured at ~2 µm, α'' was measured as much as ten times smaller (0.1 µm and 0.3 µm) (Murr, Quinones, *et al.*, 2009). Research has shown that α'' is softer phase than α'. This can be seen by measuring micro-hardness, as found by Huang *et al.* (2015). Unlike α', α'' is able to form through the application of an external stress (Gammon *et al.* 2004). The precipitation of α'' is difficult to reveal by transmission electron microscopy (TEM) and is not detectable by X-ray diffraction (XRD).

Pederson (2002: 13) showed that orthorhombic α'' martensite forms when β phase with 10 ± 2 wt % vanadium is quenched, Figure 2.16. This V wt % exists in the temperature range of 750 – 900 ºC. At higher temperatures, the V wt % in β drops further leading to the formation of α' upon quenching. In reality a mixture of α', α'' and β will form depending on local elemental composition (Pederson, 2002).

Dislocation twinning inside α' are commonly observed as depicted by the SEM images of martensite in Figure 2.17. Two types of laths are present in martensite based on grain size: primary - large parallel-sided laths and secondary - smaller randomly distributed laths. The first is formed at an early stage of martensitic transformation, while the secondary laths are formed at a later stage (and lower temperature). The distinguishing size difference between the two has an important influence on the nature of recrystallisation during heat treatments, as discussed in the next section.

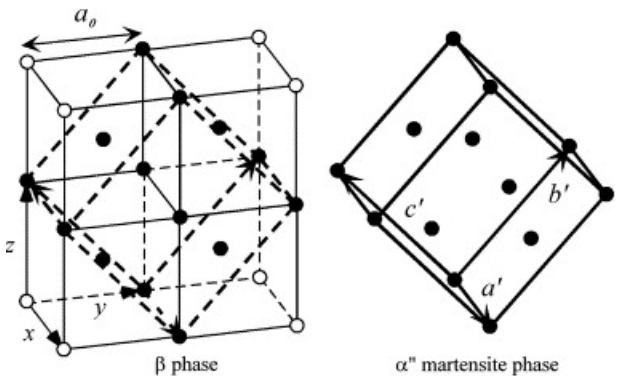

Figure 2.15: Schematic of the lattice relationship between β and α'' (Kim *et al.* 2006) where a' = 0.30 nm, b' = 0.49nm, c' = 0.46 nm (Murr, Quinones, *et al.* 2009)

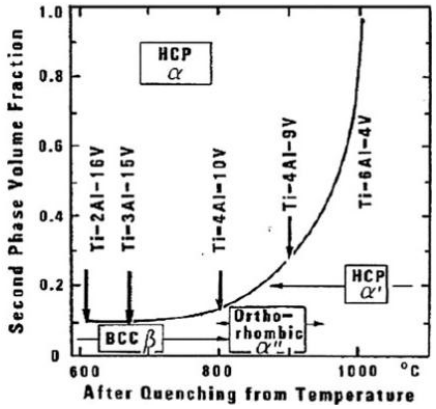

Figure 2.16: Secondary phase (α' and α'') formation upon quenching from different temperature ranges (Lee and Welsch, 1990)

(a) (b)

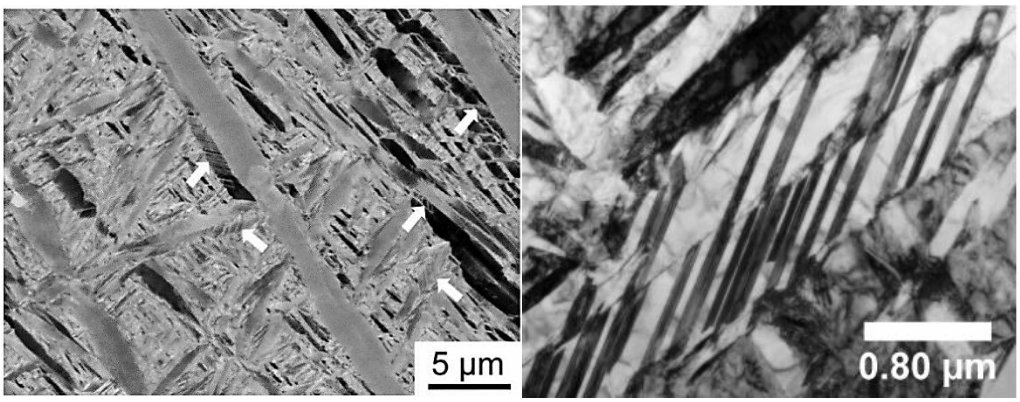

Figure 2.17: SEM images of martensitic microstructure: (a) arrows point out twins (Beladi, Chao and Rohrer, 2014) (b) fine twinning structure inside α' grains observed

2.6. MARTENSITIC DECOMPOSITION AND RECRYSTALLISATION

The process of martensitic decomposition is of great concern to SLM-produced Ti6Al4V research since martensite is starting microstructure for SLM-produced Ti6Al4V. Therefore, SLM-produced Ti6Al4V phase transformation all go through martensite transformations (decomposition) during heating. Literature has conflicting definitions of martensite decomposition and tends to use the terms 'martensite decomposition' and 'recrystallisation' interchangeably.

Martensite has, by definition, been decomposed when α'/α'' has transformed to a dual phase (α+β). Ivasishin & Teliovich (1999) claimed that martensite decomposes via an α''→ β → α+β route, instead of α'' → α+β. Although β phase has been shown to form at a temperature of 650 ºC, (Sallica-Leva *et al.* 2016), the formation of α from α' is not as easy to verify since both are HCP crystal structures.

Verification of whether the phase is α or α' has been done by measuring the elemental composition of the phases in question. Tan *et al.* (2016) measured the

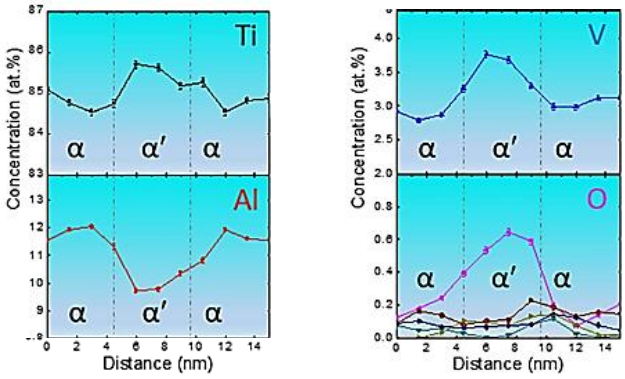

Figure 2.18: Distinguishing between α' and α using atom probe tomography (Tan *et al.* 2016)

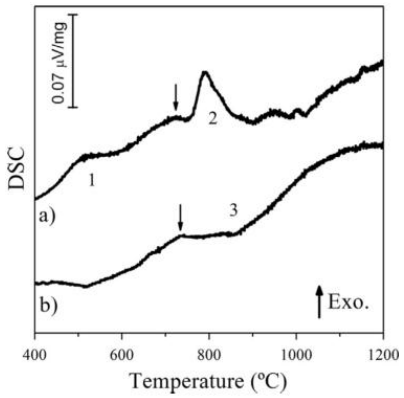

Figure 2.19: Differential scanning calorimetry (DSC) plot (a) as-build SLM-produced Ti6Al4V (b) fully annealed SLM TI6AL4V reference material (Sallica-Leva *et al.* 2016)

element partitioning due to de decomposition of martensite. These results are depicted in Figure 2.18.

A clear difference in the kinetics of transformation upon heating (heat rate of 10 º per min) between as-built SLM-produced Ti6Al4V and wrought Ti6Al4V can be seen by a study done by Sallica-Leva *et al.* (2016). A comparison of differential scanning calorimetry (DSC) results of as-build, Figure 2.19(a), and fully annealed (1050 ºC furnace cooled) SLM-produced Ti6Al4V, Figure 2.19(b), is illustrated. The exothermic peak indicated by '1' in the as-built sample is argued to be due to relaxation of residual stress. Inflection points indicated by the arrows represent the start of α'/α'' → (α+β) transformation. In the fully annealed sample, this transformation is simply a diffusional process of the already present β phase. In the as-build martensite, the exothermic peak at point '2' is argued to be due to the decomposition of α' through mass recrystallisation/transformation of α'/α'' → (α+β).

While Gil Mur, Rodríguez and Planell (1996) reported little to no martensitic decomposition of forged Ti6Al4V at 400 ºC (water quenched from 1050ºC to induce martensitic microstructure at room temp), as depicted in Figure 2.20(a), recent conflicting results by Xu *et al.* (2015) claimed that martensite produced by the SLM process was decomposed into a ultrafine (α+β) (near) equilibrium lamellar microstructure at 400ºC.

Vilaro, Colin and Bartout (2011) measured the hardness of Ti6Al4V samples cooled using furnace cooling (FC) and air cooling (AC) methods. A decrease in hardness for the temperature range of 780 º - 875 ºC was measured. The lower hardness was argued to be due to α'' phase.

The effect of recrystallisation-type phase transformation becomes apparent at temperature of 750 ºC and above. A larger amount of recrystallisation allows for smaller α' grains to dissolve to β and thereby allow larger α grains to grow. This can be seen by the measured increase in α grain size as shown in Figure 2.21.

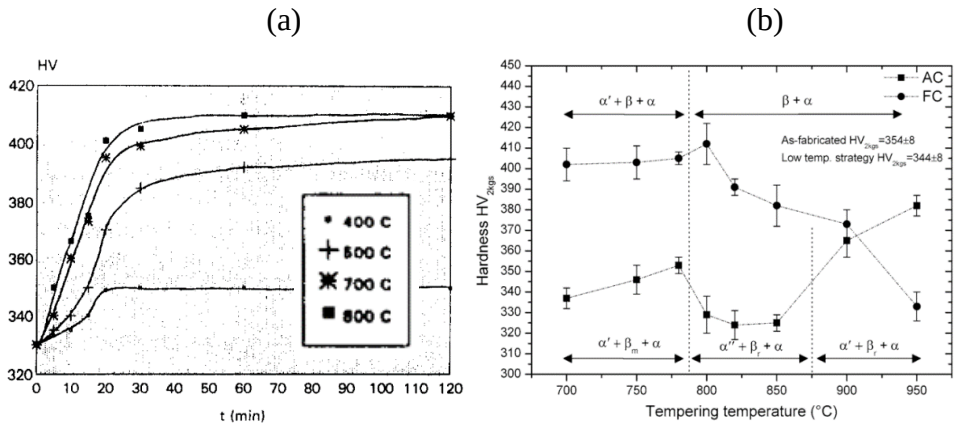

Figure 2.20: WQ Martensite decomposition of samples (a) Hardness evolution for four different holding temperatures (furnace cooled) (Gil Mur, Rodríguez and Planell, 1996) (b) hardness evolution for a range of temperature and cooling methods (hold time 2 hours) (Vilaro, Colin and Bartout, 2011)

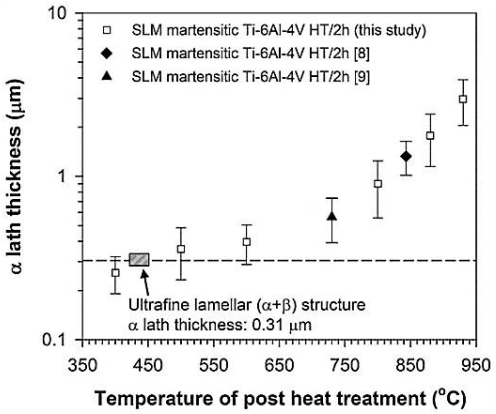

Figure 2.21: Influence of annealing temperature on α grain size (Xu *et al.* 2015)

2.7. FULL BETA PHASE – MICROSTRUCTURAL KINEMATICS

The nature of the fully β phase Ti6Al4V (i.e. above the β-transus temperature) in terms of grain size and orientation, has a significant impact on the morphology of the final room temperature HCP microstructure (α'/α'' or α). Knowledge of the β phase microstructure and behaviour is therefore of importance.

The β-transus temperature acts as a 'reference' temperature for annealing strategies. Due to the sensitivity and difficulty in measuring the temperature in situ, literature quotes the temperate at a range of values.

Elmer *et al.* (2005) calculated the β-transus of TI6AL4V ELI containing:

6.0Al, 4.2V, 0.11O, 0.17Fe, 0.0028H, 0.014C, 0.009N, <0.03Si, bal. Ti, (by wt %)

using *ThermoCalc*® with the Ti-data data base (distributed by *UES Software*). The transus was found to be 956 ºC. In comparison, the β-transus of Ti6Al4V ELI containing 0.13 weight % oxygen was found to be 975ºC by Sefer *et al.* (2014). The transus was found by Seshacharyulu *et al.* (2000) to be 20 ºC lower than commercial grades. Lee and Welsch (1990) determined the correlation between oxygen wt % in Ti6Al4V and β-transus to be of the form:

$$T_{transus} = 937 + 243[O] \quad (7)$$

Where [O] is in wt % oxygen and temperature values are in ºC. The correlation equation however does not consider other phase stabilising elements such as nitrogen.

Grains grow during super-β-transus annealing. The magnitude of time above β-transus is directly proportional to the square of the β grain diameter as described by Semiatin *et al.* (2013: 3855):

$$d^2 - d_0^2 = k(t - t_0)\exp(-Q/RT) \quad (8)$$

In which d and d_0 denote the instantaneous and initial β grain sizes at times t and t_0 respectively, the rate constant k equals 1110 m^2/s. Q is an apparent activation energy (312 kJ/mol), R is the gas constant, and T the annealing temperature in Kelvin.

β grain growth was investigated by Elmer *et al.* (2004) in Ti6Al4V welds who found that the β grains in the fusion zone grew epitaxially from large β grains in the heat affected zone, as depicted in Figure 2.22. Grain size was furthermore shown to decrease with distance from the fusion zone. This is attributed to the microstructure further from the fusion being less affected by (and reaching lower maximum temperature) the melting of material in the fusion zone.

The same β grain shape has been observed for SLM-produced Ti6Al4V parts. Elmer *et al.* (2004) showed that upon weld solidification, β grains orientate themselves in the direction of heat flow. The grains therefore grow epitaxial in the direction of heat flow. This causes a {100} BCC texture to develop as observed by Simonelli (2014).

Up until now, planar solidification has only been found in SLM parts made from pure metals: Ta and W, and (α+β) titanium alloys (Thijs, 2014: 57). This results in long columnar grains growth across printing layers such as those observed in the EBSD maps by Antonysamy, Meyer and Prangnell (2013), Figure 2.23. The nature of β grains in SLM-produced Ti6Al4V is of great significance to the current research and is further discussed in 2.12.3.

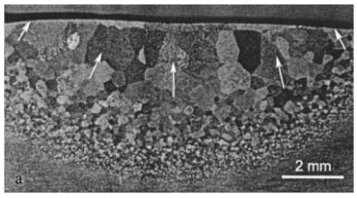

Figure 2.22: (a) Micrographs of the cross-section of a Ti6Al4V weld. White arrows indicate faint dark line of the fusion zone boundary (and also indecently the direction of β grain growth) (Elmer *et al.* 2004)

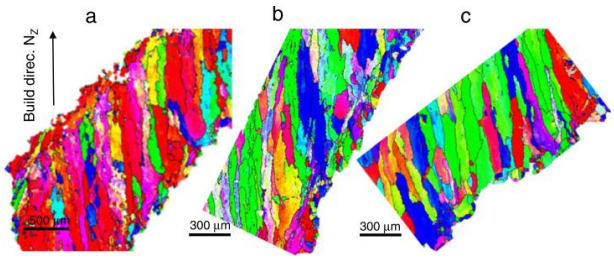

Figure 2.23: EBSD orientation maps of columnar β grains orientated in the direction of heat flow (a) built at 45 ° to base plate, (b) 60 ° and (c) 30 ° (Antonysamy, Meyer and Prangnell, 2013)

2.8. SURFACE OXIDATION (SCALE) AND FORMATION OF OXYGEN RICH ALPHA CASE

Titanium alloys are extremely corrosion resistant at room temperature due to the formation of a thin oxide TiO_2 layer (2 – 7 nm thick) which prevents the diffusion of oxygen to the inner material. The diffusion of oxygen and nitrogen and the influence thereof on microstructure start to become prominent at temperatures exceeding 500 °C (Lütjering and Williams, 2007). Nitrogen and especially oxygen diffusion is therefore of concern during heat treatments. In cases where the removal of contaminated material through machining or chemical means (or both) is not feasible, special precautions need to be taken to prevent the contamination with oxygen.

Oxidation at elevated temperatures starts with formation of a micro-thin layer of TiO_2 referred to as oxide scale. The further diffusion of oxygen or nitrogen into the outer thin layer of the Ti-alloy acts as a α phase stabilising alloy preventing β phase from forming. This outer layer of α phase is known as α case, as depicted by Figure 2.24. α case also strengthens the phase by solid solution strengthening. While a harder outer surface layer increases strength, it reduces part ductility.

Chretien *et al.* (2010) showed that for Ti6Al4V ELI prism sample of dimensions: 25,4 by 25,4 by 127 mm, α case did not grow more than 57 µm for heat treating in atmospheric air for 6 hrs and 955 °C (AC). The micrograph from which this was measured is depicted in Figure 2.24(b). Microhardness is also an effective parameter used to evaluate α case depth. The measured microhardness and corresponding micrograph of a Ti6Al4V sample treated for 500 hrs at 700 ºC is depicted in Figure 2.24(a).

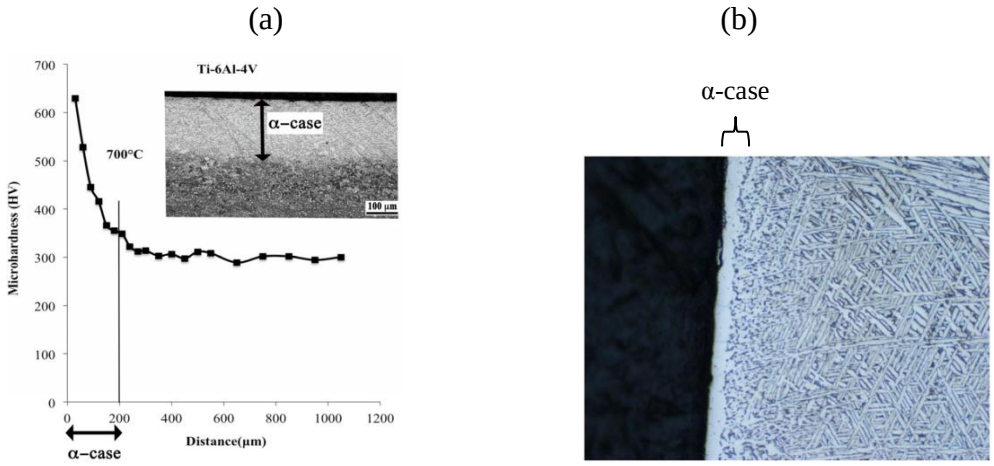

Figure 2.24: (a) Change in hardness through α case layer (700 ºC for 500 hours) (Sefer, 2014) (b) α case outer layer measured thickness 57 µm (6 hours at 955 ºC) (Chretien *et al.* 2010: 31)

Surface oxidation during heat treatments can be reduced through means suggested by AMS H81200 (Heat Treating of Titanium and Titanium Alloys). These include

annealing in an inert atmosphere such as argon, using ceramic coatings, and/or annealing in high vacuum. Ceramic coatings are a popular material used to preventing α case formation. These are especially used for metal casting moulds, but are also used to coat SLM Ti6Al4V during annealing. Commercial ceramics include: calcium oxide (CaO) zirconium oxide (ZrO_2), zirconium orthosilicate ($ZrSiO_4$), and aluminium oxide (Al_2O_3).

2.9. THERMOMECHANICAL PROCESSING

Tradition processing of Ti6Al4V involves mechanical forming and annealing (usually at an elevated temperature) of an ingot or bloom into final or near-net shape. Thermomechanical processing (TMP) starts with mill forming through either rolling or forging the ingot. TMP thereafter depends on application and process parameters can be varied such as deformation percentage, and temperature cycles. Annealing temperature and cooling rate are key factors in controlling the morphology of the final microstructure.

CP titanium (ASTM and ASME grades 1 through 4) and titanium alloy ingots are produced from high-purity grade titanium sponge through the vacuum arc remelting (VAR) process. Alloying elements in their powder form are added during this process. Both the purity of the sponge material and the alloy additions is crucial for the structural integrity of the final billet/ingot. The steps of bloom production is schematically illustrated by Donachie (2000: 26) and included in Appendix L.1. Donachie furthermore defines processing as:

"…the wrought, cast, or powder methods used to produce the alloy in the appropriate condition for the intended application, as well as the heat treatments that are applied to the alloy."

The processing of Ti6Al4V has been researched and developed extensively. Standard specifications pertaining to Ti6Al4V include:

- UNS: R56400,
- AMS: 4911, 4920, 4928, 4934-4935, 4965, 4967, 6930-6931, T9046
- ASTM: B265, B348, B381 F136
- MIL: T9046-T9047
- MMS: 1217, 1233
- DMS: 1570, 1583, 1592, 2285, 2442 R-1
- BMS: 7-348

Due to the long holding time and slow cooling rate of Ti during bloom production, the final microstructure is extremely coarse (often more than a millimetre in grain diameter). Waziers *et al.* (2009) reiterated that the primary problem in wrought processing is such course grain size. The microstructure therefore is extensively refined through deformation processing above and below the β-transus. This process, popularly known as 'ingot breakdown' increases the production cost of

the finished titanium products, which limits their wide-ranging use (Waziers *et al.* 2009).

Ti6Al4V processing can be divided into four main operations. A schematic illustration of each process is depicted in Figure 2.25. Operation 1 aims to attain a homogenous microstructure throughout the part. Plastic deformation during the second operation breaks down the large α colonies. The degree of plastic deformation determines the fineness and texture strength of the microstructure. Figure 2.26 illustrates 50% plastic working and 80% plastic working to compare the difference in grain morphology.

High plastic deformation such as depicted in Figure 2.26 break up the large α laths by introducing large amount of dislocations. Operation 3 allows for β phase to grow along newly introduced dislocations and thereby globularise the microstructure. This process is schematically illustrated on Figure 2.28. Small α grains are 'consumed' by β during operation 3 and globularisation of larger grains occur. The final heat treatment operation 4 is at a low temperature to strengthening and/or stress relieving the material.

Bi-modal microstructures (a microstructure with two different grain morphologies), such as depicted Figure 2.27, are popular in their application in areas where high strength and toughness are required, such as aerospace. The formation of this microstructure goes through the traditional operation steps. A fast to intermediate cooling rate during operation 3 allows for new (secondary) α to grow in-between the globularised (primary) α.

If the final globularisation is performed very low in the (α+β) field and/or the cooling rate from the globularisation is very slow (furnace cool), then instead of a bi-modal microstructure, a fully equiaxed microstructure is produced, consisting only of (globular) primary α.

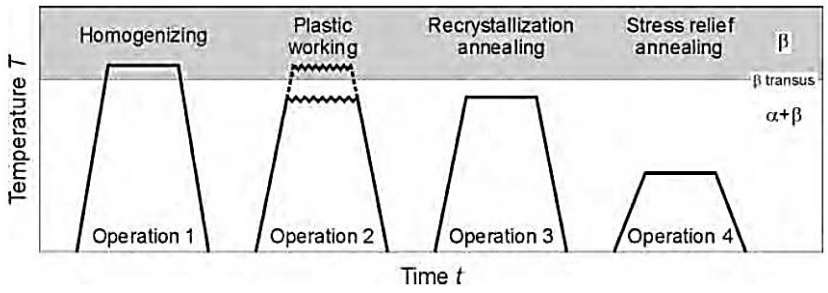

Figure 2.25: Operational steps of traditional Ti-alloy processing (Motyka *et al.* 2012)

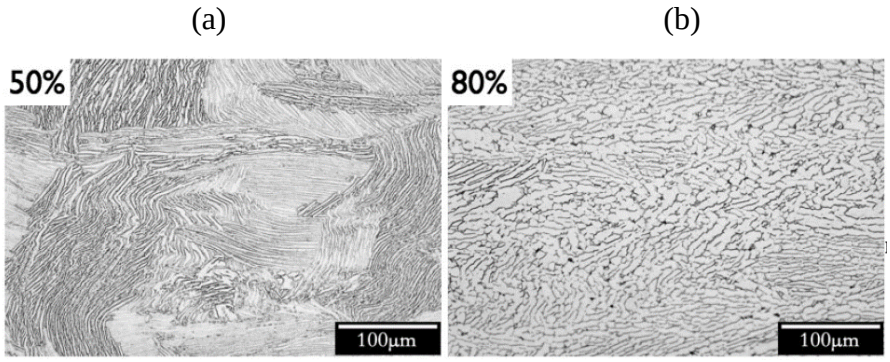

Figure 2.26: Ingot breakdown of α colonies during operation 2. (a) optical micrograph of 50 % strained material, and (b) 80 % strained material (Weaver, 2011)

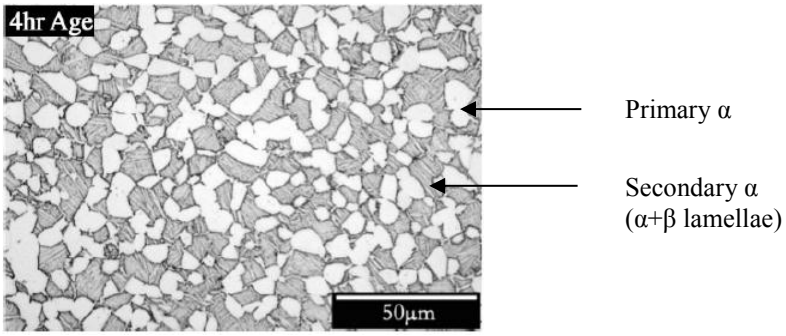

Figure 2.27: Optical micrograph of a bi-modal microstructure. 50% deformed and annealed at 950 °C for 4 hrs followed by air cooling. Thereafter annealed at 700 °C for 2 hrs) (Weaver, 2011)

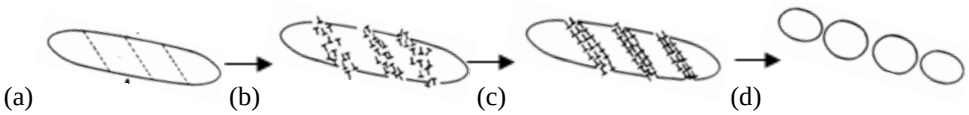

Figure 2.28: Schematic of the deformation process of α lamellae into globular grains during TMP (sub-β-transus Operation 2) (a) applied load, (b) introduction of dislocations, (c) coalescence of dislocations, (d) globularisation during recrystallisation annealing. Adapted from (Seshacharyulu *et al.* 2000).

2.10. TEXTURE AND THE INFLUENCE OF TEXTURE AND GRAIN MORPHOLOGY ON TENSILE BEHAVIOUR

When material is thermomechanically processed, crystal structure becomes textured. Texture in crystallography can be defined as a repetitive and preferential crystal orientation taken on by the microstructure. Crystallographic texture is a by-

product of forming and aids in strengthening the material in a certain direction. Crystallographic texture caused mechanical properties to be anisotropic in nature.

TMP causes HCP and BCC crystals to deform per their preferential slip systems. This causes the crystal structure to take on a set orientation with respect to the working / rolling direction. The orientation of the HCP and BCC crystals with respect to the rolling direction is depicted in Figure 2.29 (Zeng and Bieler, 2005).

Lütjering and Williams (2007) illustrate both the achievable texture during different rolling processes in Figure 2.30(a), (RD – Roll Direction) and the effect of texture on directional tensile behaviour as shown in Figure 2.30(b). Pole figure plots are explained in Chapter 2.13.3.

Sefer (2014) summarised the influence of different microstructural morphologies (lamellar and equiaxed) and their respective size on different mechanical and physical properties of Ti6Al4V as tabulated in Table 2.5.

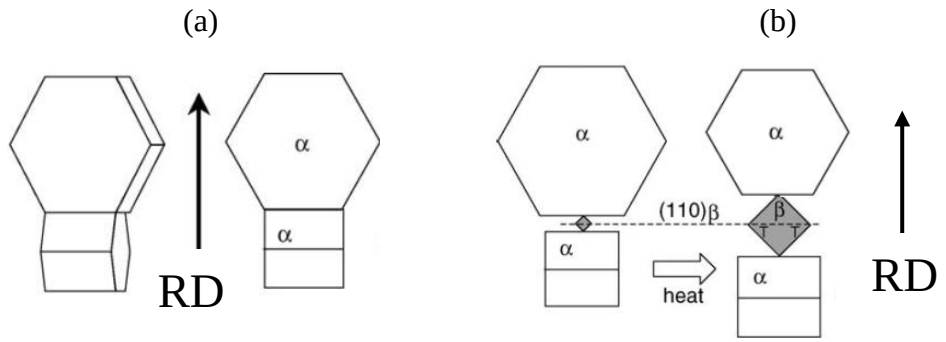

Figure 2.29: Relative crystal orientation formed due to working in the (a) α phase field, (b) α+β phase field. Adapted from (Zeng and Bieler, 2005)

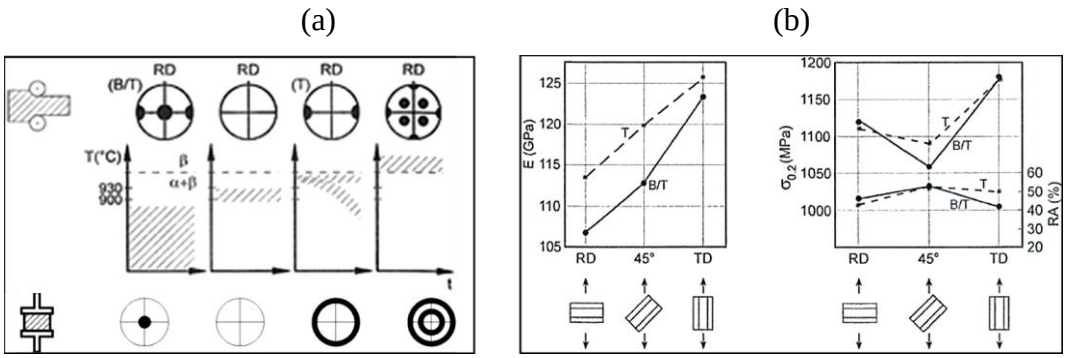

Figure 2.30: (a) Crystallographic texture ((0001) pole figures) resulting from different rolling processing routes (B/T) Basal/Transverse texture, (T) Transverse texture. (b) Correlation between tensile direction and texture for different rolled Ti6Al4V (Lütjering and Williams, 2007)

Table 2.5: Influence of microstructural characteristics on mechanical properties (Sefer, 2014)

Property	Lamellar	Equiaxed	Fine	Coarse
Young's Modulus	No effect	Positive/negative (texture)	No effect	No effect
Strength	Negative	Positive	Positive	Negative
Ductility	Negative	Positive	Positive	Negative
Fracture Toughness	Positive	Negative	Negative	Positive
Fracture Crack Initiation	Negative	Positive	Positive	Negative
Fracture Crack Propagation	Positive	Negative	Negative	Positive
Creep Strength	Positive	Negative	Negative	Positive
Super–plasticity	Negative	Positive	Positive	Negative
Oxidation rate	Positive	Negative	Positive	Negative

2.11. INDUSTRIAL HEAT TREATMENT STRATEGIES

This section revises traditional annealing processes of Ti6Al4V utilised in industry. Since these processes have been specifically designed to produce the desired microstructure in wrought Ti6Al4V they are less applicable to SLM-produced Ti6Al4V. Knowledge of the way in which the heat treatments are applied remain relevant and therefore serve as guidelines in developing heat treatment strategies for SLM-produced Ti6Al4V material. The extraction and production of Ti and Ti billet/ingot from raw ore has been excluded from the discussion since it falls outside the scope of the thesis.

A table of common annealing processes (other than stress relief) are is included in Appendix L.2 and contain the processes of:

- Mill annealing (MA) (working the material at an elevated temperature)
- Duplex (and Triplex) annealing which can consist of a combination of:
- Beta annealing (also called normalisation) and/or
- Recrystallisation annealing (also referred to as solid-solution anneal) and/or
- Aging (below the α dissolution temperature ~700 - 750 ºC)

The following industrial Ti and Ti-alloy heat treatments are summarised based on work by Donachie (2000).

2.11.1. Mill annealing (MA)

Mill annealing is a general term used for describing a common heat treatment performed on products formed in a mill. The final microstructure is globular in nature and the material is relatively soft and machinable. The TMP commonly used for this type of annealing is: 730 ºC held for 4 hours, then furnace cooled.

Mill-anneal (MA) is the most commonly used starting state for Ti6Al4V. Mechanical properties according to Donachie (2000) of mill annealed products are: 945 MPa yields stress, 1069 MPa UTS and 10 % elongation-to-fracture. Mill-annealing is often the pre-curser to 'formal' heat treatment strategies.

2.11.2. Solution treated and aged (STA)

STA is the most common heat treatment for titanium alloys. Best mechanical strength is achieved by STA of the mill-annealed material when heated between 25 to 85 ºC below the β-transus thereafter quenched in water and aged at 480 to 595 ºC for 4 to 8 hrs (or 705-760 ºC for 2 hours) thereafter air cooled. Table 2.6 gives the mechanical properties of Ti6Al4V bar-stock quenched from a range of temperatures and aged at 480 ºC.

Table 2.6: STA - tensile properties of 13mm Ti6Al4V barstock (Aging treatment 8 hrs at 480ºC air cooled) (Donachie, 2000)

Solution-treating temperature		Room-temperature tensile properties(a)				
		Tensile strength		Yield strength (b)		Elongation in 4D(c),
°C	°F	MPa	ksi	MPa	ksi	%
845	1550	1025	149	980	142	18
870	1600	1060	154	985	143	17
900	1650	1095	159	995	144	16
925	1700	1110	161	1000	145	16
940	1725	1140	165	1055	153	16

2.11.3. Full anneal / β-anneal (BA)

Full annealing (homogenisation) is the first operation in the traditional heat treatment process of Ti6Al4V (refer to Figure 2.25) and entails heating above the β-transus temperature and holding (Donachie, 2000). Full annealing essentially ‘resets’ the α phase microstructure of the material. Room temperature α-Ti is very sensitive to the cooling rate from the β phase (as discussed in Section 1.5).

2.11.4. Hot isostatic press (HIP)

Hot isostatic pressing is a specialised post-process which uses high temperature and high pressure to improve sample density while at the same time coarsening the microstructure. Hot isostatic pressing is a popular heat treatment strategy for SLM-produced components due to the inherent micro-defects in the part resulting from process parameters (discussed in Section 2.12.2). A typical HIP process used on SLM-produced Ti6Al4V is at 920 ºC and at a pressure of 103 MPa for 4 hrs followed by furnace cooling (Qiu, Adkins and Attallah, 2013).

2.12. SELECTIVE LASER MELTING

2.12.1. Process description

Manufacturing techniques are traditionally subdivided per the state of their starting material. Based on this classification, four types of AM systems exist: liquid-based systems, filament/paste-based systems, solid-based systems and powder-based

systems. A discussion of each individually is outside the scope of the study and the processes and characteristic of each system is included in Appendix J. Whereas the first three types are more commonly used for forming non-metallic parts (polymers, ceramics, biomaterial), all metallic parts are formed through a powder based AM process (MAM).

A discussion of MAM techniques of SLS and EBM as well as the working principles of the SLM laser is included in Appendix J.2. A discussion of laser focal offset distance and its application in reducing thermal gradients, is included in Appendix J.2.

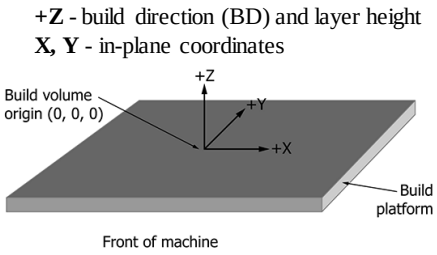

Figure 2.31: Reference coordinate system of SLM build platform (ASTM F2924 – 14)

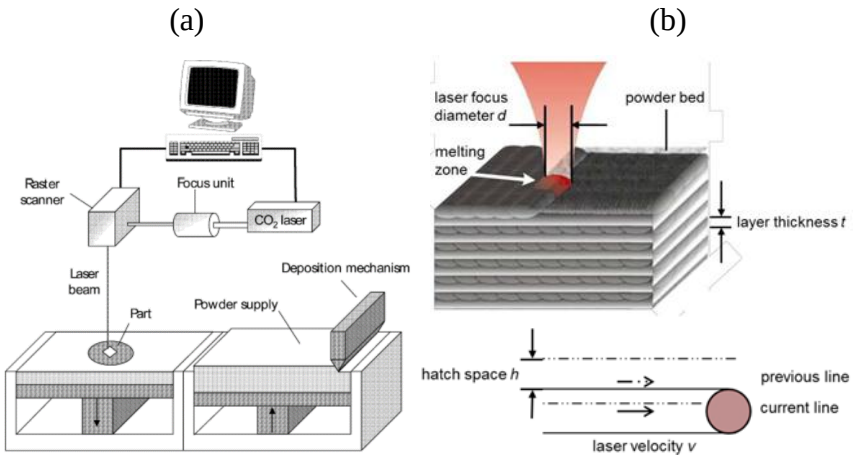

Figure 2.32:(a) Schematic for a laser melting and/or laser sintering machine setup (Simchi & Pohl, 2003), (b) SLM process parameters (Hahn, 2012)

2.12.2. SLM part porosity

Porosity in SLM-produced parts has been a major drawback to the technology. The cause of porosity in SLM-produced parts is broad and complex. Thanks to a large research effort into optimising the process parameters of SLM, a large improvement has been made with most SLM machines capable of achieving >99 % density part. Kruth *et al*. (2010) however argue that a *"…small amount of porosity could still be*

unacceptable in certain application areas where fatigue loading or excellent strength ductility is necessary".

Kruth *et al.* (2010) found that the high roughness of peaks and valleys formed during each layer can cause the coater to deposit a non-homogeneous layer of powder over the previously printed layer. This causes powder to be too thick in some valleys for laser power successfully melt the powder. This causes insufficient fusion between layers and a 'lack of fusion' porosity.

Rough surfaces furthermore cause the entrapment of gas between printed layers and newly deposited powder (Morgan, Sutcliffe and O'Neill, 2004). When the new layer is being scanned, the entrapped gas superheats and rapidly expands removing the liquid metal above it. This causes a pore to form.

Porosity has also been found to be caused by melting-pool collapse at the end of the scan vector. Modelling of pore formation in SLM by Khairallah *et al* (2016) gives insight into the kinetics of pore formation, Figure J.4.

Qiu, Adkins and Attallah (2013) found the two main process parameters that influence porosity to be scan speed and laser power. Furthermore, their investigation into different scan speeds and laser power parameters found that a higher scan speed and laser power had the effect of decreasing porosity, Figure J.5.

Scanning strategies

The laser scan strategy is the pattern which the printer uses to build the part. Research into various scan strategies, shown in Figure 2.33, and their effect on part density and residual stress has been researched by Thijs (2014).

Kruth *et al.* (2010) found that a bi-directional, alternating scan strategy, Figure 2.33(C-F), produced a higher part density than compared to unidirectional or non-alternating scanning strategies.

Concept Laser's *M2* machine uses a patented 'islands' scan strategy in which the scan surface is divided into 5x5mm block, Figure J.6.

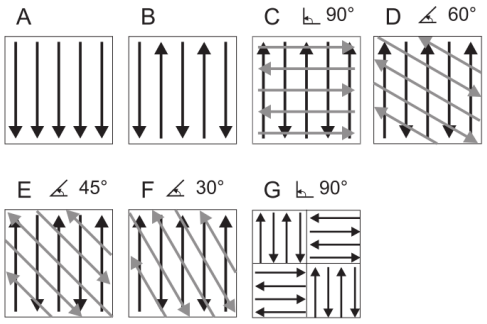

Figure 2.33: Various scan strategies. Arrows represent scan vectors (Thijs, 2014: 153)

Re-melting scan strategy

The remelt scan strategy can be used to further improve density by remelting each layer (at the cost of increasing the fabrication time and the amount of residual stress) and adjusting parameters from a single scan strategy (Kruth *et al.* 2010). Surface re-melting is used to improve surface quality.

Influence of scanning strategy on residual stress

In a study by Kruth *et al.* (2010) it was found that part-edge angle-curl from base plate, and hence residual stress, was reduced when shorter scan lengths were used (below 10 mm). Furthermore, it was found that the 'islands' scan strategy reduced residual stress compared to bi-directional (zigzag) scanning; however decreasing island size did not have a significant influence on residual stress. Rotating the 'islands' was shown to decrease residual stress with and rotation of β=45º to the part x axis, Figure 2.34, achieving the best reduction in residual stress of 36 % compared to reference bi-directional (zigzag).

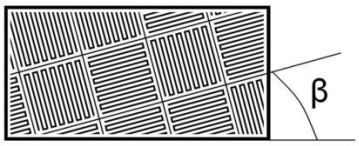

Figure 2.34: Angle of rotation β of 'island' scan strategy (Kruth *et al.* 2010)

2.12.3. Physical and mechanical properties

Various studies have been conducted in determining the mechanical properties of as-built SLM-produced Ti6Al4V. A table of various SLM machine parameters and their resulting porosity and mechanical properties is attached in Appendix J.1.

UTS and Ductility

Yan and Yu (2015) compared findings of densification, mechanical properties and microstructure of over 100 different studies on the four most popular AM Ti6Al4V techniques – SLM, EBM, SLS and LMD. A summary of the achievable UTS and elongation to fracture by various authors is plotted in Figure 2.35. SLM-produced Ti6Al4V achieves a high strength but low elongation % compared to the other MAM methods.

Influence of build orientation on anisotropy of tensile behaviour

Various studies have shown that the β grains grow epitaxially through successive layer depositions, Figure 2.36. This has been investigated in studies by Carroll, Palmer and Beese (2015) and Antonysamy, Meyer and Prangnell (2013). Since build orientation influences microstructural properties (long columnar grains) mechanical properties have been found to be anisotropic.

Influence of SLM-produced microstructure on mechanical properties

Vickers hardness in SLM-produced Ti6Al4V samples were measured and found to be influenced by prior-β grain size and orientation (Chlebus *et al.* 2011). Chlebus *et al.* (2011) measure a lower hardness on the ZX face of the build direction than compared to the XY face. This is due to the relative size of the β grain.

Due to the axial growth of the β phase in the direction of the build, the cross-sectional size of the prior-β grains in the ZX plane is larger. This has the effect of longer and thicker α' grains in this face and therefore a lower Vickers hardness. Hardness is also effected by the degree of martensite decomposition during building. Waziers *et al.* (2009) furthermore found the α phase texture in SLM-produced Ti6Al4V to be fairly weak.

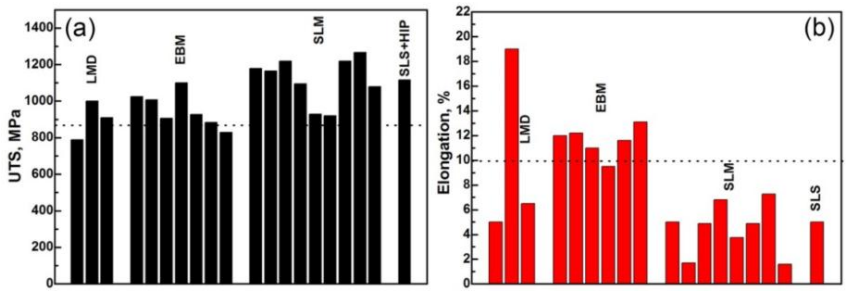

Figure 2.35: A comparison of mechanical properties of as-built MAM Ti6Al4V achieved by various techniques (a) UTS and (b) elongation to break percentage. Dotted lines indicate ASTM specifications. (Yan and Yu 2015: 90)

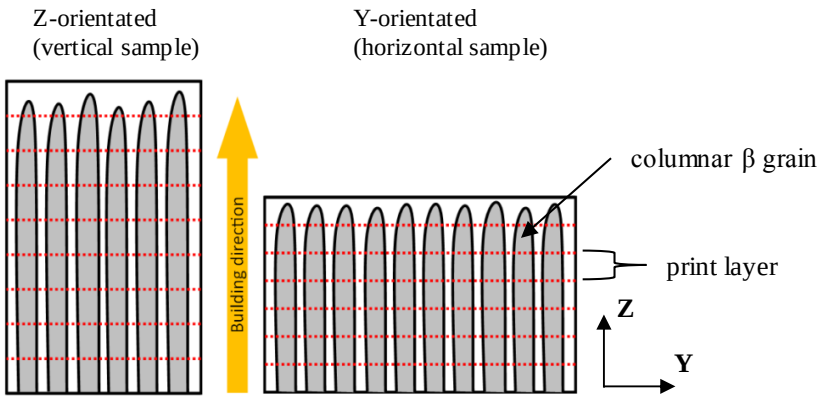

Figure 2.36: The influence of build direction on β grain shape

2.13. ANALYSIS AND REPRESENTATION OF MICROSTRUCTURE AND CRYSTALLOGRAPHIC TEXTURE

This section gives a brief overview of microstructural analysis techniques applicable to Ti6Al4V. Detail discussion on analysing EBSD data is presented.

Microstructural analysis of Ti6Al4V is complex due to the features spanning a wide range of size scales. This makes quantification of the microstructure challenging.

Furthermore, the information available from a two-dimensional section of the microstructure image using optical microscopy is limited in terms of understanding its three-dimensional structure. Methods such as polarised light microscopy have been implemented to better detect lamellae colonies.

Stereology analysis procedures have been used to quantify titanium alloy Ti6Al4V microstructure. Software such as Adobe Photoshop with FoveaPro add-in allows for a set of functions for computer-based image processing and measurement.

2.13.1. Optical microscopy

The use of optical microscopy for analysing Ti microstructures, is an effective way to determine microstructural characteristics. While the analysis tool itself is more of a subjective tool, certain quantitative analysis procedures can be used such as image processing. Through processing of a digital image of the microstructure using computer software tools such as *Matlab*, certain quantitative data can be extracted such as average grain size and average geometric alignment.

The reader is encouraged to consult the ASM handbook on non-ferrous metals (Gammon *et al.*, 2004) for insightful methodology of sample preparation and the resulting optical quality of the microstructure. Sample etching techniques for titanium alloys are included in Appendix I.1.

Tools such as Differential Image Contrasting (DIC) are useful in improving the contrast of crystal features such as α' grains. The Nomarski prism, Appendix I.2, is a DIC tool that splits the incoming light into two non-parallel beams. These beams of light then hit the sample at two different angles thereby enhancing, for example, the topography of the crystals in the specimen.

2.13.2. Principles of electron backscatter diffraction (EBSD)

EBSD is used to obtain crystallographic orientation information of a metallic sample. EBSD works on the principle of constructive and destructive interference of backscattering electrons reflecting off the crystal lattice surface. The constructive interference of electrons cause bands of lines called Kikuchi bands, Figure 2.37. Since the Kikuchi bands relate directly back to the crystal structure and orientation, the bands are indexed per a database of patterns, of which the orientation is known, to identify the crystal phase and orientation, Figure 2.37.

(a) (b)

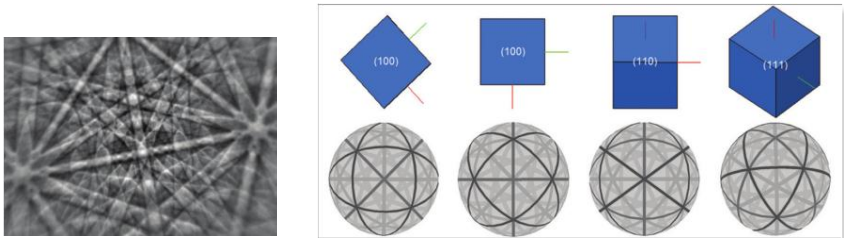

Figure 2.37: (a) Kikuchi bands and (b) their relation to cubic orientation (EBSD Explained - From data acquisition to advanced analysis, 2015)

2.13.3. Crystallographic orientation representation

There are two reference co-ordinate systems that are used to describe orientation: the sample reference system (K_s) and the crystal reference system (K_c), Figure 2.38(a). Sample axis are the Roll Direction (RD) = X, Transverse Direction (TD) = Y and Normal Direction (ND) = Z. The orientation of each crystal in the sample can be described by an orientation matrix:

$$\boldsymbol{g} = \begin{pmatrix} cos\alpha_1 & cos\beta_1 & cos\gamma_1 \\ cos\alpha_2 & cos\beta_2 & cos\gamma_2 \\ cos\alpha_3 & cos\beta_3 & cos\gamma_3 \end{pmatrix} = \begin{pmatrix} g_{11} & g_{12} & g_{13} \\ g_{21} & g_{22} & g_{32} \\ g_{31} & g_{32} & g_{33} \end{pmatrix} \quad (9)$$

Where $\alpha_{(1\text{-}3)}$ and $\beta_{(1\text{-}3)}$ are the angles between the crystal axis and sample axis as depicted on Figure 2.38(b). Letters (α, β, γ) refer to the sample axes (X, Y, Z) and subscript (1-3) refer to the crystal axis [100], [010] and [001]. For example, $\gamma_2$refers to the positive angle from crystal's [010] axis to the sample's Z-axis.

(a) (b)

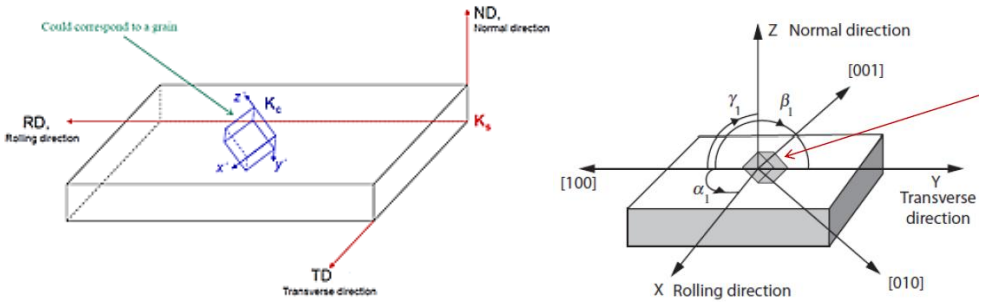

Figure 2.38: Relating sample and crystal reference systems (a) axes and (b) reference angles (Weaver, 2011)

A useful property of the orientation matrix is that the rows represent crystal axis vectors with respect to sample axis and the matrix columns represent sample axes with respect to crystal axis (as illustrated in Figure: 2.39).

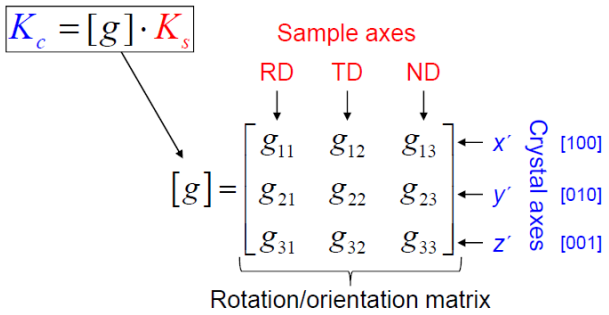

Figure: 2.39: The crystal orientation matrix (Weaver, 2011)

Bunge Euler Orientation convention

A common way to describe crystal orientation is through Euler angles. Euler angles describe the rotation of a crystal through angles: φ_1, Φ and φ_2 from a reference crystal orientation of (φ_1, Φ, φ_2) = (0, 0, 0) with respect to a certain specimen axis arrangement. This reference orientation is chosen per convention in which crystal axis are aligned with reference co-ordinate system axis.

Typically, in commercial EBSD and texture analysis software such as *Oxford Instruments* the HCP crystal's [2 $\bar{1}$ $\bar{1}$ 0] direction is aligned with that of the roll direction (RD), and the [0001] is aligned with the normal direction (ND), Figure 2.40(a).

Since the *Matlab* toolbox *MTex* uses the convention of TD//[2 $\bar{1}$ $\bar{1}$ 0], Figure 2.40(b), the burgers orientation relationship of φ_1 =135 º, ϕ =90 º and φ_2=325 º needs to be adjusted to φ_2 =355 º to accommodate the 30 º rotation difference between Figure 2.40(a) and Figure 2.40(b).

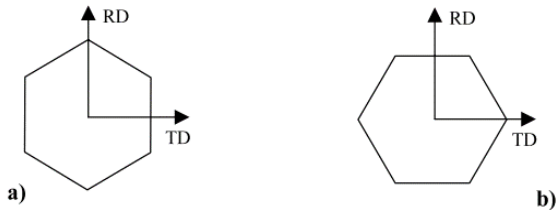

Figure 2.40: HCP reference orientation conventions (a) TD//[10-10], (b) TD//[2-1-10] (Glavicic *et al.* 2003)

Euler angles are determined by the following consecutive steps:

1. Rotation counter clockwise about crystal z-axis (c-axis) through φ_1
2. Rotation counter clockwise about crystal x-axis (a-axis) through Φ
3. Rotation counter clockwise about crystal z-axis (c-axis) through φ_2

Orientation matrix values are related to the Euler angles through:

$g_{11} = \cos\varphi_1 \cos\varphi_2 - \sin\varphi_2 \sin\varphi_2 \cos\phi$

$g_{21} = -\cos\varphi_1 \sin\varphi_2 - \sin\varphi_1 \cos\varphi_2 \cos\phi$

$g_{31} = \sin\varphi_1 \sin\phi$

$g_{12} = \sin\varphi_1 \cos\varphi_2 + \cos\varphi_1 \sin\varphi_2 \cos\phi$

$g_{22} = -\sin\varphi_1 \sin\varphi_2 + \cos\varphi_1 \cos\varphi_2 \cos\phi$

$g_{32} = -\cos\varphi_1 \sin\phi$

$g_{13} = \sin\varphi_2 \sin\phi$

$g_{32} = \cos\varphi_2 \sin\phi$

$g_{33} = \cos\phi$

Pole figures (PF)

Pole figures are a useful way of portraying 3D orientation information on a 2D surface. Pole figures describe the sample's crystal orientation with respect to the sample reference frame. Figure 2.41 illustrates how a pole figure is constructed for a single crystal (unit cell). The three orthogonal pole orientation vectors (100, 010, 001) are taken from the crystal orientation matrix rows.

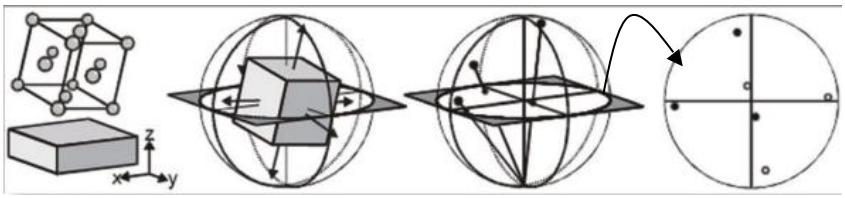

Figure 2.41: Schematic explanation of a stereographic projection of a single crystal and the resulting (1 0 0) pole figure (EBSD Explained - From data acquisition to advanced analysis, 2015)

Metallic parts usually contain many crystals. Each crystal has a different orientation. The orientation distribution of the poles can be effectively visualised with a pole contour plot. Pole contour plots are calculated from orientation density information. High orientation intensities are coloured red while low orientation distribution intensities are coloured blue.

Inverse pole figures (IPF)

An inverse pole figure is a pole figure of the sample direction with respect to the crystal orientation. Due to crystal symmetry, the IPF plots consists of orientation-identical areas (symmetrical regions). EBSD crystal orientation maps are coloured per IPF orientation colours. IPF plots use hue-saturation-value (HSV) colour sections as depicted in Figure 2.42. Each unique crystal orientation is therefore coloured per its IPF orientation.

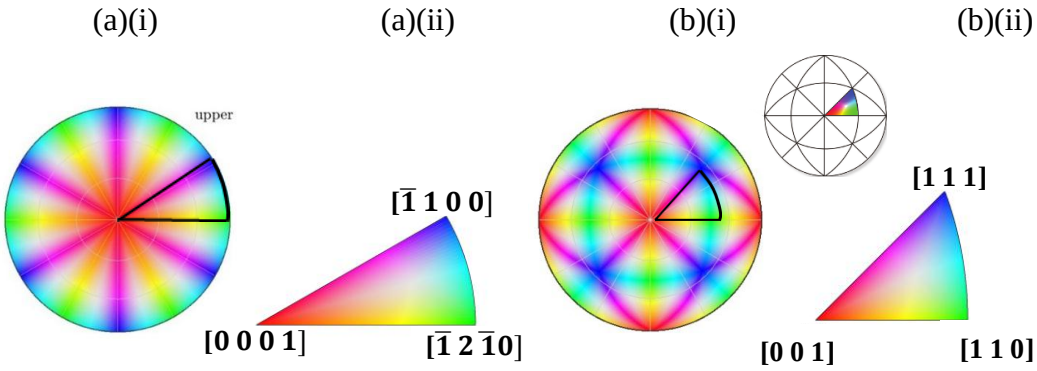

Figure 2.42: IPF HSV plots of (a) HCP six-fold symmetry and (b) BCC 16-fold symmetry (i) complete hemisphere plot (ii) unique section

3. EXPERIMENTAL METHODS

Through careful consideration of project objectives and the reviewed literature, experimental methods were developed to achieve these objectives and project aim. This chapter lays out the methodological steps followed to achieve the set objectives.

3.1. POWDER CHARACTERISATION

3.1.1. Background

Ti6Al4V ELI powder used in SLM-processing is manufactured through a gas atomisation process. Simonelli (2014) investigated the nature of the atomised Ti6Al4V ELI powder particles (depicted in Figure 3.1(a)) by slicing a single particle and doing EBSD scans on the cross-sectional surface, as shown in Figure 3.1(b). Microstructure of the powder is α' in nature, as seen on Figure 3.1(b) and (c). Powder size distribution claimed by *TLS Technik GmbH & Co* plotted in Figure 3.2(d).

Powder quality and size distribution varies with suppliers. Rafi *et.al.* (2013) analysed particle size spread with a *Microtarc 3000* particle analyser and found that powder supplied by *EOS* had and average particle size diameter of 36 µm while the powder supplied by *Arcam* had an average particle size of 60 µm with a larger spread of large particle sizes.

Metal powder used in MAM is extremely expensive. Fine metal powder used for SLM is more expensive than powder used for powder metallurgy sintering. SLM powder costs roughly $400 per kg compared to conventional PM Ti metal powder which is around $30 per kg (Yan and Yu, 2015). Yan and Yu (2015) considered this a bottle-neck issue for MAM.

(a) **(b)** **(c)**

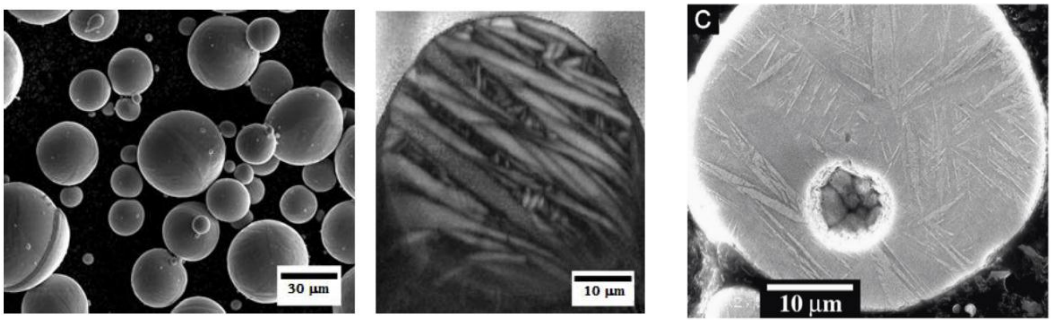

(d)

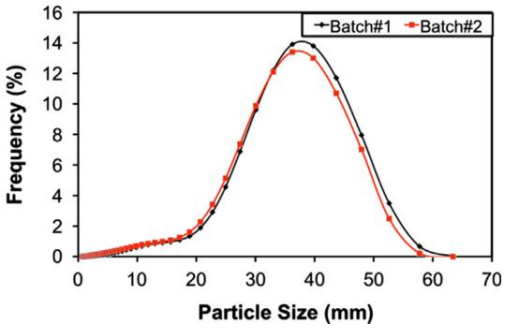

Figure 3.1: Gas-atomised Ti6Al4V powder (a) shape and morphology (b) image quality map of ion-beam milled powder particle (Simonelli, Tse and Tuck, 2012) (c) Martensitic microstructure surface topology (Qiu, Adkins and Attallah, 2013) (d) Particle size distribution of powder supplied by *TLS Technik GmbH & Co* (Qiu, Adkins and Attallah, 2013)

3.1.2. Powder used in the current study

Pre-alloyed Ti6Al4V ELI powder for the current study was acquired from *TLS Technik GmbH & Co.* Elemental, morphology and particle size analysis was performed according to ASTM F3049-14 using the methods and instruments tabulated in Table 3.1. Throughout the thesis, it is automatically inferred that that the ELI version of Ti6Al4V is referred to when referring to SLM-produced Ti6Al4V.

The morphology of new and used powder is presented in Figure 3.2 for comparative purposes (Thejane, Chikosha and du Preez, 2016). While powder particles from the new powder were predominantly spherical in shape, the used powder contained fused powder particles (indicated by arrows) that were much larger than the individual powder particles.

Table 3.1: Powder characterisation analysis techniques and instrumentation

Characteristic	**Method/Technique**	**Instrument**
Elemental analysis	Inductively Coupled Plasma-Optical Emission Spectroscopy (ICP-EOS)	SPECTRO ARCOS
Gas elemental composition	Inert gas fusion	ELTRA OHN 2000
Morphology	Scanning Electron Microscope	JEOL JSM-6510
Size distribution	Laser scanning	MICROTRAC SI/S3500

(a) (b)

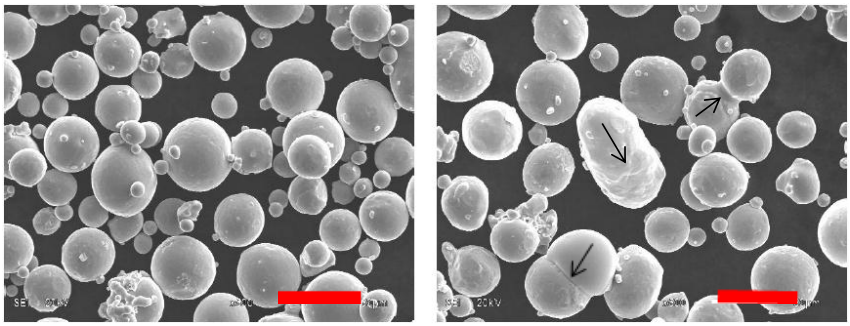

Figure 3.2: Powder morphology (a) new powder and (b) the powder after 3 cycles (red lines represent a length of 50 µm) (Thejane, Chikosha and du Preez, 2016)

The particle size distribution of the new and used powder, as measured by laser diffraction, is shown in Appendix A.3 (Thejane, Chikosha and de Preez, 2016). Both the new powder, as sampled powder from three different containers, and the old powder, as sampled from the bed after three consecutive builds, respectively, were plotted on the same set of axes. Consecutive builds result in an increase in the number of fused powder particles; this affects the particle size distribution by shifting the peak of the distribution to the right. Additionally, as can be seen from the cycle 3 results, additional peaks emerge at larger particle sizes. New powder samples displayed similar particle size distributions that correlate to the supplier specified particle size distribution. The figure furthermore shows that all fresh powder from the three containers were of the same size distribution and agree with the powder particle size claimed by the supplier (see Figure 3.1(d)).

The results of elemental analysis of powder from three newly opened canisters and three build cycles, is tabulated in Appendix A.1. The results show that the alloy elements in the powder are within the required standard set by ASTM F3001. The powders were also analysed through X-ray micro computed tomography scans. Details of equipment and scan settings are given in Section 3.7 and Appendix G.1 Results of these scans are presented in Chapter 3.7.

3.1.3. Scans of powder

CT scan results showed that the average powder particle diameter was 34 µm. This correlates to the laser diffraction results (Appendix A.3) and agrees with the supplier powder specification. Pores inside some of the powder particles could be seen and quantified. The average pore diameter inside powder particles was 12.6 µm. The results of three powder scans are attached in Appendix A.2.

3.2. SLM MANUFACTURING PROCEDURES

Sample geometry was modelled in *AutoCAD Inventor 2015*. CAD data files were exported in the Stereolithography (STL) format and loaded onto a Personal Computer (PC) for post-processing. Samples were automatically sliced into 30 µm

slices (the build layer thickness) using the software *Magics* (version 15.0.0.85) from the software company *Materialse*. Sliced data files were then exported in the format CLS (**C**ONCEPT **L**aser **s**lice file) and loaded onto the SLM machine's computer for printing.

A *LaserCusing M2* machine from *Concept Laser* was used for building of samples. The machine has a single fibre laser with a maximum power 200 W in continuous laser pulse mode. The laser is supplied by *Rofin* and is a model *Starfiber 200*. The printer's build volume is 250 x 250 x 280 mm^3 (x, y, z) and build layer thickness ranger from 20 – 50 µm. The maximum laser speed is 7 m/s and laser focal diameter is adjustable in the range of 70 – 200 µm. European Commission (EC) machine conformity declaration and *M2* machine specification are found in Appendix D.2 and Appendix E respectively.

Samples were built in a chamber flooded by a continuous flow of argon gas supplied by *Afrox* of grade: technical. Gas flow rate was ~45 litres / min and flowed from the right to the left across the build plate (X-axis) to remove burn-gasses and metal/powder splatter. The amount of oxygen in the build volume was automatically controlled by the machine and kept below 1 % ppm by switching argon gas flow on or off as required.

The *M2* machine by default uses a patented 'island' scan strategy. This strategy scans the surface in 5 mm-sized squares called islands. The squares are at 45 ° to the baseplate's X/Y-axis and are each scanned in a 'zigzag' pattern with each adjacent square being scanned at 90 ° relative to its neighbours, as shown Figure 3.3(a).

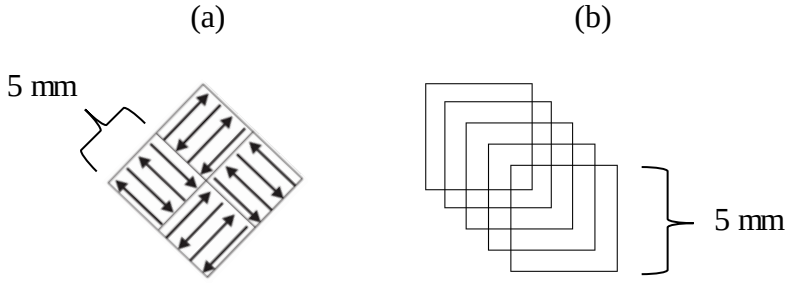

Figure 3.3: (a) *M2* island hatch strategy (Thijs, 2014), (b) island shift strategy

Consecutive build layers are scanned at 90 ° to the previous layer and shifted 1 mm (or 0.2 × D_1 where D_1 is the island side-length) in the XY-plane away from the previously scanned square. When the scanning of a layer is complete, the sample perimeter is scanned with a single vector, using the same laser setting, to improve surface quality of the finished part.

Default process parameters recommended by *Concept Laser* for their own manufactured powder (CP Ti6Al4V ELI) was used. These parameters are tabulated in Table 3.2. Hatch spacing refers to the distance between the centres of two parallel scan vectors. Beam compensation refers to the island overlap distance.

Table 3.2: Printing process parameters

Power (P) [W]	**Velocity (V) [mm/s]**	**Layer thickness (t) [µm]**	**Laser spot diameter (d) [µm]**	**Hatch spacing (h) [µm]**	**Beam compensation (a_2) [µm]**
100	600	30	150	105	22.5

3.3. TENSILE SAMPLE GEOMETRY AND BUILD LAYOUT

While it is possible to manufacture samples with final 'dog-bone' tensile dimensions using SLM, the lack of a smooth surface finish (as required by standard ASTM E8M (ASTM E8/EM-11, 2011)) means that post process machining will be necessary. This, and the fact that samples might be used for future projects which might require a larger sample diameter, was motivation to add additional material in radial direction of the samples and thereby build the samples in cylindrical shape.

Cylindrical samples, from which tensile samples were later cut, were built in three separate build sessions. A summary of the build-layout is tabulated in Table 3.3. Vertically printed samples (or Z-orientated according the ASTM F2924 – 14 (ASTM International, 2014) reference coordinate system) were designed in the form of simple cylinders with an outer diameter 15 mm and lengths of 20, 93 and 103 mm, respectively. These samples were built during all three build sessions, as noted by the "vertical" samples in Table 3.3. Horizontally printed samples (or X-orientated according the ASTM F2924 – 14 reference coordinate system) were designed with an outer dimension of 15 mm and lengths of 93 and 103 mm, respectively. These were built during the third build session. While most samples were designed with a length of 93 mm, the 103 mm length samples allow for a 10 mm off-cut to be made after heat treatment for microstructural analysis.

Sample labels designate (a) from which build session (B1, B2, B3) the part originates and (b) the position on the build plate (1-50), as depicted in the photographs of the sample builds in Table 3.3. For example, the sample #34 from build session 2 was labelled: B2-34.

Tensile (dog-bone shaped) sample geometry design (Figure 3.4) was based tensile test standards: ASTM E8M and the ISO 6892. Part gauge design diameter (G) was limited to a maximum tensile load of 30 kN. This is the load limit of the available tensile testing machine.

Per the calibration done on the load cell on the 10th November 2016 (calibration certificate number SHQ – 56868 C), the calculated uncertainty is ± 0.26 % of the reading. So, on a reading of 20 kN, for example, the error is 52 N. This in stress is 52 N÷(gauge area) = 2.6 MPa.

A large gauge diameter (D) allows for a greater achievable machining dimensional tolerance and a lower influence of microscopic defects on tensile properties. Gauge length (L) was chosen to accommodate the extensometer length (25.4 mm) in accordance with ISO 6892, to compare the fracture elongation to that of the required fracture elongation in ASTM F2924–14. The extensometer was used in the elastic region of the test to determine the elastic strain in order to calculate the samples' Young's modulus.

The maximum extension of the extensometer during experiments was under 1 mm. If ones round up to the conservative value of 1 mm extension for the extensometer, the absolute error is 3.5 µm. (This is per the manufacturer's test done on the 17th Feb 2012). The absolute error of 3.5 µm in terms of elongation percentage is: (0.0035mm÷25mm) × 100 = 0.014 %. This is a negligible error for the results obtained.

Final sample dimensions after machining are tabulated in Table 3.4. A technical drawing of tensile sample can be found in Appendix C.

Table 3.3: Sample build summary

Build Session	**Build 1**	**Build 2**	**Build 3**
Types of samples (length) [samples]	Vertical (L = 93 mm) [samples # 11-50]	Vertical (L = 93 mm) [50 samples]	Horizontal (L = 93 mm) [samples # 2-7, 9 and 10]
	Vertical (L = 103 mm) [samples # 1-10]		Horizontal (L = 103 mm) [samples # 1 and 8]
			Vertical (L = 20 mm) [20 samples]
Photo of build 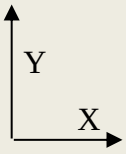		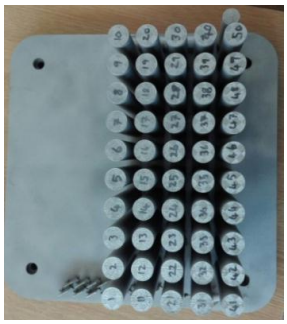	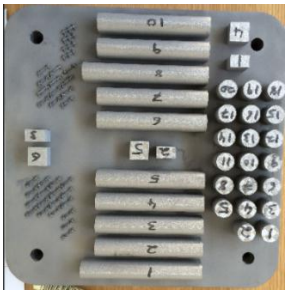

Table 3.4: Final tensile sample dimensions

Design UTS [MPa]	D [mm]	Maximum Load [kN]	G [mm]	A [mm]	R [mm]	B [mm]	L [mm]	C [mm]
1250	5	24.54	25	40	5	26.5	93	M12x1.75

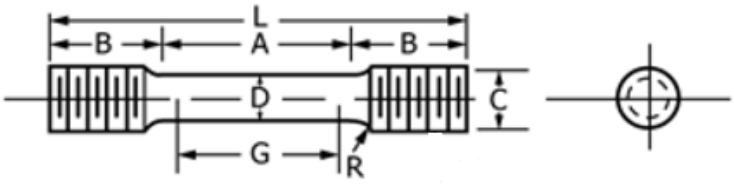

Figure 3.4: Machined sample labelling (ASTM E8/EM-11, 2011)

3.4. HEAT TREATMENT DESIGN

This chapter presents details about the furnace used, furnace calibration, as well as oxidation depth during heat treatments.

All samples were heat treated in one of the two identical 5 kW *Gallenkamp* muffle furnaces (model: *Type 2*). These furnaces are capable of heating, in air only, at a maximum rate of 10 ° C/min up to 1200 ° C and are controlled by EUROTHERM temperature controllers. While the preferred furnace used by researchers for heat treatment of SLM-produced Ti6Al4V ELI is an argon or vacuum furnace (due to titanium's high affinity for oxidation), the muffle furnaces were chosen for a couple of reasons. Firstly, the box furnace can take a greater number of samples simultaneously as opposed to the available argon/vacuum furnace and secondly, since the samples can be taken out promptly, cooling methods such as air cooling and water quenching are possible (unlike in the vacuum furnace which only allows for furnace cooling).

3.4.1. Furnace calibration

Initial heat treatments produced unexpected results, leading to evaluation of the actual furnace temperature as well as the temperature profile within the furnace chamber. The evaluation showed that the actual sample temperatures were much higher than the temperature reading on the furnace controller. The design flaw was revealed after several heat treatments were conducted. This temperature difference between the actual sample temperature and the furnace controller reading was due to the furnace thermocouple's reference junction being fastened / bolted to the back metal-casing of the furnace (see Figure 3.5 for schematic of thermocouple).

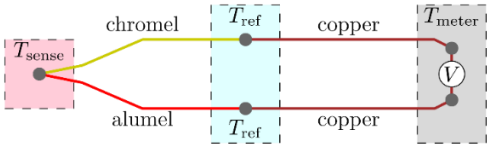

Figure 3.5: Type K thermocouple standard configuration (Nanite, 2014)

The thermocouple used for the temperature control of the furnace is a K-type thermocouple, a general-purpose thermocouple, applicable for measuring temperatures from -200 to 1350 ° C. The furnace design flaw caused the reference

junction to conduct heat from the furnace casing and therefore be at a much higher temperature than anticipated. The sensing temperature, T_{sense} (i.e. the actual sample temperature) is calculated per Equation (10), relative to the reference temperature (T_{ref}), by measuring the potential difference, *V*, at the meter and knowing the relationship between electrical potential, E_p, and temperature, *T*, for the thermocouple.

If the reference temperature is assumed to be at room temperature, but is in fact at a higher temperature, as was the case in the setup used, the calculation of the sensing temperature will be incorrect. This fault can be corrected by adjusting the equation for the correct reference temperature.

$$E_p(T_{sense}) = V(T_{meter}) + E_p(T_{ref}) \quad (10)$$

Determining the reference junction temperature is impractical and therefore a more direct solution to the problem was designed. To determine sample temperature (i.e. furnace centre temperature) accurately, a thermocouple (TC) was used to measure the centre temperature of the furnace. A hole was drilled through the centre of the furnace door and a long TC was inserted. Room temperature was measured externally as ~22 ºC and since the long TC's reference junction was far away from the furnace, the reference temperature of the long TC was assumed to be 22 ºC and added to the long TC's voltage reading (see Equation (10)). The multimeter used was a *Hewlett Packard* model: 3457A. All the thermocouples used were type-K thermocouples.

During initial temperature measurements, it was revealed that the temperature varied more than 100 °C from the back to the front of the furnace. Since samples were heat treated in batches of five, the thermal profile through the furnace needed to be known. A thermal profile of the centre-line of the furnace was generated by measuring the temperature (in situ) at 2 cm intervals from the back-centre to the front-centre of the furnace, Figure 3.6 and Figure 3.7(b). The temperature measurement data is included in Appendix B.1. The furnace was calibrated for furnace controller temperature readings at 600 ºC, 700 ºC and 800 ºC as these were the temperature range at which most samples were annealed. Temperature measurement for annealing at lower temperatures was performed by first measuring the temperature of the centre of the furnace and then adjusting the furnace controller temperature accordingly. The temperature difference (or error) between the furnace controller reading and the centre of each sample was therefore determined.

Both furnaces are identical and experience the same temperature measurement flaw. Centre temperatures measured from the non-calibrated furnace compared well with that of the calibrated furnace and therefore the temperature profile calibration determined for the one furnace was applied to the other.

Figure 3.6: External thermocouple measurement set-up

3.4.2. Furnace thermal profile and sample temperature

Once the temperature measurement data was collected, *Matlab*'s *Curve Fitting Tool* was used to generate a thermal profile model of the average temperature difference between the temperature measurements from the furnace and external, positional TC. A cubic spline interpolation function was used to generate the temperature difference profile. The furnace temperature difference profile was used to accurately determine each sample's annealing temperature based on their position relative to the back wall of the furnace.

A plot of the average temperature difference profile is shown on Figure 3.7(a). Samples were placed on a brick and spaced 30 - 32 mm apart from each other, as illustrated on Figure 3.7(b). The brick allowed for the samples to be in the centre of the furnace, both from vertically (top to bottom) and transversely (side to side). Single samples were placed in the centre of the furnace. Sample temperature was adjusted to the correct value per the furnace temperature difference profile. The average temperature difference for the fives samples from the back of the furnace to the front are: 81 ºC, 76 ºC, 70 ºC, 62 ºC, 51 ºC positions 13, 16, 19, 22 and 25 cm from the back of the furnace wall, respectively.

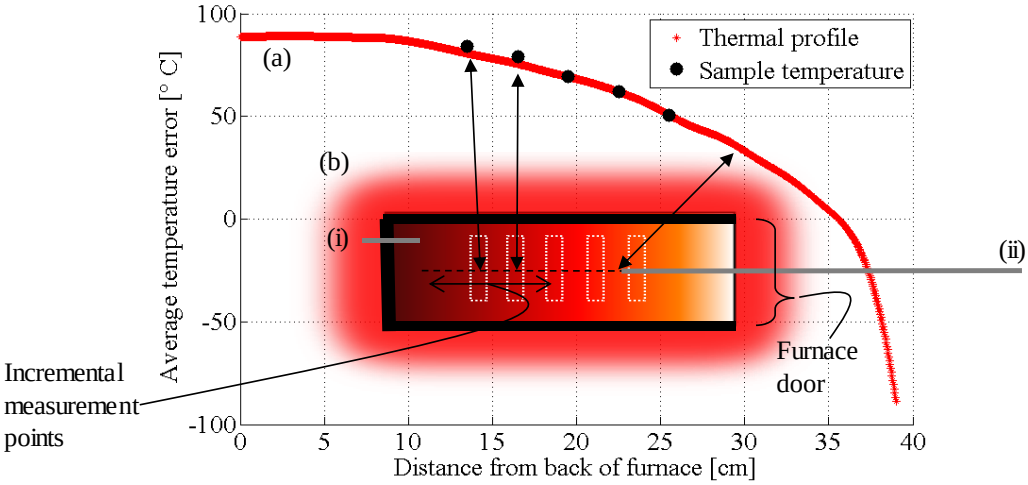

Figure 3.7: (a) Furnace temperature difference profile and (b) Schematic of sample position in furnace (sectional top view). Broken lines represent cylindrical sample outlines. (i) Furnace TC and (ii) External TC

3.5. ANNEALING STRATEGIES

This section presents the annealing strategies chosen to

Investigate transformation kinetics of the SLM-produced Ti6Al4V material

Evaluate the tensile properties of the heat treated SLM Ti6Al4V material.

In addition to samples being labelled per their build session (as noted in Section 3.3), samples were also labelled per their respective annealing strategy. Samples were identified by the label T#-G#-#, where

T# indicates the tensile test (1 or 2),

G# indicates the annealing group, and

The final # indicates the sample number from within the annealing group.

For example, a sample (#3 in the batch of 5 samples) from heat treatment group 4 of test 1 would be given the identification T1-G4-3. As-built sample groups were designated a group number of 0. The four, different heat treatment or annealing strategies followed are described in the next sections.

3.5.1. Strategy 1: Low temperature annealing

Low temperature annealing (also referred to as a stress relief) occurs at a temperature below the temperature range commonly associated with Ti6Al4V ELI recrystallisation. The aim of this heat treatment is to relieve residual stress caused by thermal gradients in the samples during printing, while maintaining the as-built microstructure. This strategy entailed a 600 ºC anneal for 8 hours followed by furnace cooling (FC), as tabulated in Table 3.5. For this heat treatment, three samples were packed close to each other instead of being spaced 3 cm apart.

Therefore, each sample was assumed to have reached a temperature of 600 ºC. This group was labelled: T2-G2. An additional sample was also annealed at 510 °C and subject to the same holding time and cooling rate. Full details of the annealing strategy and the labels of the samples used for this annealing study are given in Table 3.5.

Table 3.5: Annealing specifications of first annealing strategy. All samples were furnace cooled.

Tensile test #	**T2**	**Heat treatment group #**	**G2**
Heat treatment procedure	Furnace controller set-point temperature:		530 °C
	Hold at 600 °C for 8 hours, followed by FC		
Sample labels	**Tensile test and annealing**	**Build**	**Sample temperature [°C]**
	T2-G2-1	B1-6	600
	T2-G2-2	B1-7	600
	T2-G2-3	B1-20	600
	T2-G2-4	B3-8	510

3.5.2. Strategy 2: Recrystallisation annealing

As presented in Chapter 2.7, recrystallization of Ti6Al4V describes the martensitic decomposition of the alloy into a dual-phase α-β microstructure by heat treatment. Typically, recrystallization refers to the process whereby a prior microstructure is converted into a new microstructure by the formation of a new set of grains, from within the prior grains, by a specific heat treatment process. In Ti6Al4V, the initial martensitic α'/α'' microstructure decomposes into both α and β grains after heat treatment at a temperature above the specified recrystallization temperature. Recrystallization annealing is therefore defined in this study as heat treatment at a temperature that is sufficiently high enough to allow α grains to grow and consume (recrystallise) smaller grains.

This can only take place through the transformation of the smaller α grains to β phase to allow "space" for α grains to grow / consume. β phase percentage significantly increases at the temperature range above ~750 ºC and therefore this temperature was assumed to be the start of the recrystallisation temperature range for Ti6Al4V.

The aim of this heat treatment s was to decompose the as-built martensite phase (α') into dual-phase (α+β) microstructure. This takes place through the simultaneous transformation of $\alpha' \rightarrow \alpha$ and $\alpha' \rightarrow \beta$. The appropriate heat treatment temperature is claimed to be between 760 - 850 °C (Sallica-Leva *et al.* 2016), which coincides with the martensite transformation (M_s/M_f) temperature (Gil Mur, Rodríguez and Planell, 1996) (Lu *et al.* 2016) for a holding time of 4 hours (Huang *et al.* 2015). Due to α grain growth, a decrease in strength, according to the Hall-Petch relationship, is expected. A lower holding temperature was selected in order to limit grain growth and so limit the anticipated loss in material strength; but since the time

for full martensite decomposition at lower temperatures (below 800 ºC) is uncertain, the holding time was increased to 8 hours for these samples. All samples were air cooled (AC). The specifications of this annealing strategy are tabulated in Table 3.6.

A wide range of recrystallisation temperatures were selected aimed at:

(a) determining the trend in annealing temperature with tensile properties
(b) aiding the understanding of the martensitic decomposition kinetics
(c) determining the effect of cooling rate from different sub-β-transus temperatures on the final microstructure development

Table 3.6 presents the heat treatment procedures, along with the labels of the samples used for these heat treatments.

Table 3.6: Annealing strategy 2: Recrystallization annealing parameters, including labels for samples used in these tests.

Tensile test #	**T1**	**Heat treatment group #**	**G1**
Heat treatment procedure	Furnace controller set-point temperature:		800 °C
	Hold at 800 °C for 4 hours, followed by AC		
Sample labels	**Tensile test and annealing**	**Build**	**Sample temperature [°C]**
	T1-G1-1	B1-1	870
	T1-G1-2	B1-23	880
	T1-G1-3	B1-29	876
	T1-G1-4	B1-34	862
	T1-G1-5	B1-42	850
Tensile test #	**T1**	**Heat treatment group #**	**G3**
Heat treatment procedure	Furnace controller set-point temperature:		750 °C
	Hold at 750 °C for 4 hours, followed by AC		
Sample labels	**Tensile test and annealing**	**Build**	**Sample temperature [°C]**
	T1-G3-1	B1-4	820
	T1-G3-2	B1-25	830
	T1-G3-3	B1-32	825
	T1-G3-4	B1-37	812
	T1-G3-5	B1-49	800

Tensile test #	**T1**	**Heat treatment group #**	**G4**
Heat treatment procedure	Furnace controller set-point temperature:		700 °C
	Hold at 700 °C for 4 hours, followed by AC		
Sample labels	**Tensile test and annealing**	**Build**	**Sample temperature [°C]**
	T1-G4-1	B1-3	770
	T1-G4-2	B1-28	780
	T1-G4-3	B1-35	775
	T1-G4-4	B1-40	762
	T1-G4-5	B1-46	750
Tensile test #	**T2**	**Heat treatment group #**	**G4**
Heat treatment procedure	Furnace controller set-point temperature:		850 °C
	Hold at 850 °C for 4 hours, followed by AC		
Sample labels	**Tensile test and annealing**	**Build**	**Sample temperature [°C]**
	T2-G4-1	B1-12	930
	T2-G4-2	B2-20	940
	T2-G4-3	B2-32	935
	T2-G4-4	B2-43	912
	T2-G4-5	B2-9	900

3.5.3. Strategy 3: β annealing and β-duplex anneal

Annealing above the β-transus temperature transforms all α phase to β phase. β phase grain growth is also expected above the β-transus. While cooling rate has less of an effect on tensile properties once the temperature has dropped below the β transus, it is the key factor that determines α grain size and therefore material tensile strength during cooling above the β-transus temperature. Samples were furnace cooled from above the β-transus to achieve a colony microstructure. Table 3.7 summarises the samples and their annealing temperature of this group.

β-duplex annealing is an annealing strategy where the sample is first heated above the β-transus, cooled and then subjected to a recrystallisation heat treatment. The aim of this heat treatment was homogenise the columnar β phase grain shape during the first annealing stage, then fast cool to achieve a fine grain structure and then anneal again to decompose the α' to α+β. The effect of homogenisation would be measurable in the horizontal and vertical samples achieving the same mechanical properties and therefore the anisotropic effect of the columnar grain shape eliminated. Due to the high level of porosity of samples from the third build, the mechanical properties of build 3 were not reliable enough to compare to that of the vertical samples. The outcome of this comparison was therefore not included in the results. Table 3.7 summarises the samples and their annealing temperature of these groups.

Table 3.7: Annealing specifications of the groups from the third annealing strategy. Samples were either furnace cooled at a rate of ~ 5-10 ° C/min, or air cooled.

Tensile test #	**T1**	**Heat treatment group #**	**G2**	
Heat treatment procedure	Furnace controller set-point temperature:			950 °C
	Hold at 950 °C for 3 hours, followed by FC			
Sample labels	**Tensile test and annealing**		**Build**	**Sample temperature [°C]**
	T1-G2-1		B1-2	1020
	T1-G2-2		B1-22	1030
	T1-G2-3		B1-30	1025
	T1-G2-4		B1-39	1012
	T1-G2-5		B1-43	1000
Tensile test #	**T2**	**Heat treatment group #**	**G5**	
Heat treatment procedures	Furnace controller set-point temperature:			(a) 950 °C
	Hold at 950 °C for 4 hours, followed by WQ			
	Furnace controller set-point temperature:			(b) 800 °C
	Hold at 800 °C for 4 hours, followed by AC			
Sample labels	**Tensile test and annealing**		**Build**	**Sample temperature [°C]**
				(a) / **(b)**
	T2-G5-1		B2-10	1020 / 870
	T2-G5-2		B2-38	1030 / 862
	T2-G5-3		B2-49	1025 / 850

Tensile test #	**T2**	**Heat treatment group #**	**G6**	
Heat treatment procedures	Furnace controller set-point temperature:			(a) 950 °C
	Hold at 950 °C for 4 hours, followed by WQ			
	Furnace controller set-point temperature:			(b) 800 °C
	Hold at 800 °C for 4 hours, followed by AC			
Sample labels	**Tensile test and annealing**		**Build**	**Sample temperature [°C]**
				(a) / **(b)**
	T2-G6-1		B3-1 (H)	1025 / 870
	T2-G6-2		B3-6 (H)	1030 / 862
	T2-G6-3		B3-3 (H)	1020 / 850

3.5.4. Strategy 4: Bi-lamellar and bi-modal microstructures

The final group of heat treatments are duplex recrystallisation annealing heat treatments that were aimed at achieving a bi-lamellar or bi-modal microstructure.

Bi-modal microstructures are the preferred Ti6Al4V microstructure used in industry due the microstructure's high combination of strength and ductility. Bi-microstructures are achieved through fast or intermediate cooling from high solid solution temperature in which the microstructure is (α+β). As cooling proceeds the beta transforms towards α by Widmanstätten growth giving rise to small lamellar (α+β) colonies between the primary alpha grains.

The first batch was therefore air cooled from around 950 - 986 ºC after eight hours and then annealed at 750 ºC for four hours followed by air cool. The second batch was water quenched from 910 - 930 ºC after 8 hours and then annealed at 750 ºC for 4 hours, followed by furnace cooling. During the second stage of the heat treatment, samples were placed side-by-side in the centre of the furnace. The effective temperature of all the samples were therefore assumed to be at the same temperature. The specifications of this heat treatment strategy are tabulated in Table 3.8.

Table 3.8: Specifications of the forth annealing strategy. Samples were water quenched (WQ) and air cooled (AC) or furnace cooled (FC).

<table>
<tr><td>Tensile test #</td><td colspan="2">T2</td><td>Heat treatment group #</td><td colspan="2">G1</td></tr>
<tr><td rowspan="4">Heat treatment procedures</td><td colspan="4">Furnace controller set-point temperature:</td><td>(a) 900 °C</td></tr>
<tr><td colspan="5">Hold at 900 °C for 8 hours, followed by WQ</td></tr>
<tr><td colspan="4">Furnace controller set-point temperature:</td><td>(b) 670 °C</td></tr>
<tr><td colspan="5">Hold at 670 °C for 4 hours, followed by AC</td></tr>
<tr><td rowspan="5">Sample labels</td><td colspan="2" rowspan="2">Tensile test and annealing</td><td rowspan="2">Build</td><td colspan="2">Sample temperature [°C]</td></tr>
<tr><td>(a)</td><td>(b)</td></tr>
<tr><td colspan="2">T2-G1-1</td><td>B1-17</td><td>970</td><td>740</td></tr>
<tr><td colspan="2">T2-G1-2</td><td>B1-19</td><td>950</td><td>740</td></tr>
<tr><td colspan="2">T2-G1-3</td><td>B1-8</td><td>986</td><td>740</td></tr>
<tr><td>Tensile test #</td><td colspan="2">T2</td><td>Heat treatment group #</td><td colspan="2">G3</td></tr>
<tr><td rowspan="4">Heat treatment procedures</td><td colspan="4">Furnace controller set-point temperature:</td><td>(a) 860 °C</td></tr>
<tr><td colspan="5">Hold at 860 °C for 8 hours, followed by WQ</td></tr>
<tr><td colspan="4">Furnace controller set-point temperature:</td><td>(b) 680 °C</td></tr>
<tr><td colspan="5">Hold at 680 °C for 4 hours, followed by FC</td></tr>
<tr><td rowspan="5">Sample labels</td><td colspan="2" rowspan="2">Tensile test and annealing</td><td rowspan="2">Build</td><td colspan="2">Sample temperature [°C]</td></tr>
<tr><td>(a)</td><td>(b)</td></tr>
<tr><td colspan="2">T2-G3-1</td><td>B1-6</td><td>930</td><td>750</td></tr>
<tr><td colspan="2">T2-G3-2</td><td>B1-9</td><td>922</td><td>750</td></tr>
<tr><td colspan="2">T2-G3-3</td><td>B1-10</td><td>910</td><td>750</td></tr>
</table>

3.6. ARCHIMEDES DENSITY MEASUREMENTS

Sample density was measured to:

a) Correlate density with tensile behaviour

b) Correlate the density with sample position on the base plate

A precision scale from *Kern & Sohn GmbH* was used model ABT 120-5DM that complies with measurements standards as attached in Appendix D.1. For the sample mass measured, the scale had a sensitivity of 0.0001 g.

Sample density was measured according to ASTM B311-13. The suspension liquid used was iso-propanol, instead of water, to prevent the formation of air bubbles on the surface of the samples. Sample porosity percentage was calculated through,

$$\varepsilon = 1 - \rho \tag{11}$$

where ρ is the equal to the measured density of the sample divided by the theoretical density of Ti6Al4V (4.43 g/cm^3). The density of the iso-propanol at room temperature was taken from the manufacturer's specification as 0.786 g/cm^3. The density of all the samples from build 1 was measured, along with the density of six horizontal samples from build 3 and seven samples from build 2.

3.7. X-RAY MICRO COMPUTED TOMOGRAPHY SCANS

X-ray computed tomography scans (CT scans) were performed for three powder samples and two as-built cylindrical off-cuts from build sessions 1 and 2.

Scans were performed according to ASTM E1570-11 by Dr Anton du Plessis and Mr Stephan le Roux at the Central Analytical Facilities (CAF), Stellenbosch, using a *General Electric Nanotom S.* Further specification of the CT scanner can be found in Appendix G.1.

While post-scanning analysis can determine the density of a scanned object, the resolution of CT scanning causes small defects to be missed. Scan resolution is limited by sample size, and available time. Scan resolution achieved was ~20 μm. This makes the Archimedes method a more accurate method of determining overall sample density.

3.8. MICROHARDNESS MEASUREMENTS

Vickers microhardness was measured using an *Emcotest DuraScan* automatic indentation machine. Hardness was measurements according to ASTM standard E348-10. A diamond-shaped indenter type 556 was used. Load application was 2 kg force for 10 seconds. Viewing lens used was a 40x/0.65 *Nikon* lens with a depth of field of ∞/0.17 and a width of field of 0.6.

Indentations were taken in the centre of the XY plane of samples. Software used to measure indentation diagonals was: *ECOS Workflow* V2.10. A total of 10 measurements per sample were made across the sample surface.

3.9. MICROSTRUCTUAL ANALYSIS

Microstructural analysis was accomplished through three techniques:

(a) Optical microscopy at SU

(b) SEM and electron backscatter (EBS) at SU

(c) Electron Backscatter Diffraction (EBSD) at NMMU

All analysis methods required the preparation of sample off-cut surfaces. The process of sample preparation was as follows:

A sample from the centre of the furnace of each annealed batch was chosen to represent a typical part annealed in the muffle furnace. A single cylindrical end-offcut of length 10 mm long was cut along the vertical specimens' XY-plane. The offcut was also cut perpendicular to its XY-plane to reveal the ZX-plane. Horizontal samples were cut along their ZY-planes. The offcuts were mounted in either *Buehler EPOMET* or *Bakelit S* moulding compound. An automatic mounting press (*Buehler SimpliMet 1000*) was programmed to heat to a temperature of 180 ºC and hold for 3.5 minutes at a pressure of 280 bar. Samples were then automatically cooled under flowing water for 3 minutes.

The sample surface was ground using either the *Buehler Alpha* or *Struers LaboPol-1* machine. Grinding took place sequentially for 1 minute with 340, 800 and 1200 grid SiC paper with an applied load of 25 N while flushing with water. The samples were polished with 9 µm *DiaPro Allegro/Largo* suspension liquid for 5 minutes on *Struers Largo* grinding disk and then a final polish was performed using 0.04 µm *OP-S* solution for 5 minutes both with an applied load of 30 N on a *Struers DAC* polishing cloth. Samples were cleaned in-between grinding steps with running water. Samples were cleaned in between polishing steps using an ultrasonic cleaner, by *Integrated Systems*, with the sample placed in a beaker of iso-propanol.

3.9.1. Optical microscopy

Samples were etched using Kroll's Reagent. Etching time was between 5 and 10 seconds. β phase etches/corrodes preferentially allowing contrast between the α and β phases. Dark areas in the micrograph are caused by the scattering of light due the inclined surface that was etched away (such as β phase). The microstructure was observed using an *Olympus GX51* optical microscope. The microscope's differential imaging contrast (DIC) tool was used to increase contrast of α' grains since these grains are not distinguishable using etching.

An *Olympus SC30* camera connected to the microscope allowed for images to be captured digitally. Micrographs could then be taken of the sample using the software: *Olympus Stream Essentials (version 1.9.1)*. Software measurement tools allow for measurement of grain size while the image filtering tools allow for

enhanced micrograph contrast. Samples were also analysed using a stereoscopic microscope: *Olympus SZ7* stereo microscope couple with an *Olympus SC30* Camera.

3.9.2. Oxygen penetration depth

α case thickness and the effect of oxygen on α stabilisation at the sample surface was measured to determine the depth of oxygen diffusion into the samples during heat treatments. Oxygen contamination in different environments was compared to evaluate the influence of oxygen contamination of different annealing methods.

Micrographs of samples that were heat treated in air and vacuum as well as a sample coated in ceramic slurry (zirconia oxide, ZrO_2), prior to heat treatment in air, were compared. Since oxygen contamination depth increases with an increase in temperature, the highest heat treatment temperature foreseen to be done during the study was chosen for the air and slurry coated samples. Although all microstructural sample preparation and analysis was done by the author, the vacuum annealing treatment was done by a final year mechanical engineering student (Luke Davis).

Table 3.9: Annealing strategies to determine oxygen contamination

	Air	**Slurry coated**	**Vacuum**
Temperature [ºC]	1050	1050	950
Hold time [hours]	3	3	2

3.9.3. SEM and EBS

SEM work and EBS analysis was performed at the Centre for Analytics Facility (CAF) at SU using a *ZEISS EVO MA15VP* which is equipped with an electron backscatter detector (EBD). Software used to analyse SEM images at the facility was *Oxford Instruments*.

3.9.4. EBSD

EBSD scans were performed at NMMU's Centre for High Resolution Transmission Electron Microscopy (CHRTM) using a *JEOL JSM-7001F* SEM with software: *Oxford Instruments HKL-channel 5*. More information about the microscope can be found on CHRTM's website. Acquisition settings used for all the scans are tabulated in Appendix G.2. A total of ten scans were done of samples from build 1:

2 orientations of a vertical as-built sample: B1-15

2 orientations of sample T1-G4-1 (Strategy 2: ~770 °C)

2 orientations of sample T1-G1-1 (Strategy 2: ~870 °C)

2 orientations of sample T1-G2-1 (Full anneal: ~1020 °C)

Scan size was chosen to be large enough to capture several prior-β grains. EBSD data obtained for analysis is in the form of: the measurement point x-y coordinate, the point's three Euler angles and image quality value for the measurement point. All EBSD maps scanned had a total of 1 960 000 measurement points (= scan area ÷ step area).

The percentage of successfully indexed points varied from sample to sample due to factors such as surface quality, microstructural fineness and SEM acquisition settings affecting the quality of the patterns. Sample T1-G4-1 achieved an indexing percentage of 93 % in both planes. Sample T1-G1-1 achieved 90 % and 88% in XY and ZX planes respectively. The as-built sample achieved a much lower indexing percentage of only 63% for both orientations. This is argued to be due to the as-built's much finer microstructure and possible due to residual stress in the sample.

In-depth analysis of the EBSD orientation data (such as orientation and pole figure plots) was performed by the author using self-written *Matlab* code with the aid of toolbox functions provided by the open-source *Matlab* toolbox: *MTex (version 4.4)*. Various *MTex* toolbox functions were used and a detailed discussion thereof is outside of the scope of the thesis. Information of *MTex* toolbox functionality can be found on their webpage (Hielscher *et al.*, 2016)

3.9.5. β phase reconstruction and variant selection

Due to the noted influence of the building process on the β phase microstructure (β phase morphology is directly a result of the melt-pool formation and cooling) and since the β phase morphology influences both the α morphology and tensile properties, investigation into β phase orientation is of great interest.

Matlab code to reconstruct the β phase microstructure was developed. The mathematics behind the β phase reconstruction is summarised below; it is adapted from Glavicic *et al.* (2003). The *Matlab* code developed by the author to reconstruct the β phase from EBSD α data can be found in Appendix M.

The BOR can be mathematically described by:

$$\boldsymbol{D}\boldsymbol{S}_k^{\beta}\boldsymbol{B}^{\beta} = \boldsymbol{S}_j^{\alpha}\boldsymbol{P}^{\alpha} \qquad (12)$$

Where $\boldsymbol{P}^{\alpha}$ and $\mathbf{B}^{\beta}$ are the orientation matrices of α and β grains respectively. $\boldsymbol{S}_j^{\alpha}$ and $\boldsymbol{S}_k^{\beta}$ are the α and β rotational symmetry operators, respectively (tabulated in the Appendix I.3). Matrix $\boldsymbol{D}$ is a rotation matrix which describes the burgers relationship. When the orientation convention RD//[2 $\bar{1}$ $\bar{1}$ 0] is used, the BOR Euler angle φ_2 is 325 °, but since *MTex* uses the convention of TD//[2 $\bar{1}$ $\bar{1}$ 0], φ2 is increased by 30 ° to account for the difference in reference orientation conventions. The BOR Euler angles used are therefore: (135 °, 90 °, 355 °).

For a single α phase orientation, there are six unique ways, designated by $l = 1,\ldots 6$, to transform the α phase orientation into β phase:

$$\boldsymbol{T}_{l=1,\ldots,6}^{\alpha} = \boldsymbol{D}^{-1}\boldsymbol{S}_{l=1,\ldots,6}^{\alpha} \qquad (13)$$

The rotational matrix of the β phase is then calculated through:

$$\boldsymbol{B}_{li}^{\beta} = \boldsymbol{T}_{l}^{\alpha}\boldsymbol{G}_{i}^{\alpha}\boldsymbol{P}^{\alpha}$$
$$l = 1, \dots, 6 \qquad (14)$$
$$i = 1, \dots, 6$$

Where $\boldsymbol{G}_{i}^{\alpha}$ is the six-fold symmetry operator of the hexagonal system that operates on $\boldsymbol{P}^{\alpha}$ to determine the orientation-equivalent set of Euler angles within the reduced angular range. While Glavicic *et al.* (2003) used an iterative process by which an approximate solution is first determined by making $l = 1, \dots, 3$, in this study a more direct, but computational expensive route was followed through making $l = 1, \dots, 6$.

To have a high probability of finding the correct prior-β orientation, the β orientation solutions of three α grains (a triple point) were determined of which the lowest misorientation between the β solutions was chosen as the correct prior-β phase from which the three grains originated. The probability of finding a unique β orientation from three α grains is 98.18 % (Germain, Gey and Humbert, 2007). The misorientation angles between all possible β pairs are calculated by first calculating the misorientation matrix $\Delta\boldsymbol{g}_{\boldsymbol{i}}$,

$$\Delta\boldsymbol{g}_{\boldsymbol{i}} = \boldsymbol{g}_{\boldsymbol{2}} \cdot \boldsymbol{g}_{\boldsymbol{1}} \equiv \begin{pmatrix} \Delta g_{11} & \Delta g_{12} & \Delta g_{31} \\ \Delta g_{21} & \Delta g_{22} & \Delta g_{32} \\ \Delta g_{23} & \Delta g_{32} & \Delta g_{33} \end{pmatrix} \qquad (15)$$

where $\boldsymbol{g}_{\boldsymbol{i}}$ refers to the orientation matrix of the i^{th} α grain. The misorientation angle between two β grains is calculated through:

$$\gamma_i = \cos^{-1}\{(\Delta g_{11} + \Delta g_{22} + \Delta g_{33} - 1)/2\} \qquad (16)$$

The calculation is performed for all β orientations of α triple points. The β orientation with the lowest γ is chosen as the 'correct' prior-β orientation.

Implementation and variant selection

The discussed phase reconstruction was programmed in *Matlab*. *Matlab's Parallel Toolbox* was used to reduce the reconstruction time of a single map to ~8 hours using an Intel(R) Xeon(R) CPU with two quad-core processors each with hyper threading capabilities. The PC also had 40 GB's of RAM.

Once the β orientation of each triple point was determined, β grain boundaries were calculated from misorientation larger than 10 °. β grains containing less than 5 points were excluded. The map was then smoothed using a spline smoothing filter.

The variant that each α grain belongs to (attached in Appendix I.4) was determined during β phase reconstruction. This was done through calculating all 12 α-variants of each reconstructed β grain and then calculating the misorientation angle of each

α grain with each of the 12 variants. The variant with the lowest misorientation angle was identified as that to which the α grain belongs.

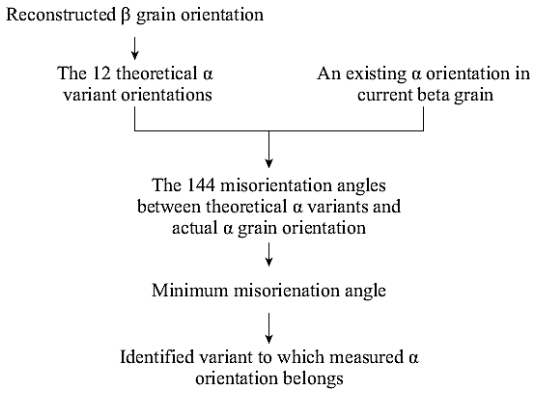

Figure 3.8: Flow diagram of the steps in determining α variants

3.10. TENSILE TESTS

Samples were machined to the standard dimensions indicated in Table 3.4, after heat treatments at SU's Mechanical and Mechatronics Engineering workshop using a manual lathe.

Samples were ground down to be 2 - 5 µm thinner (in diameter) in the centre of the gauge section (25 mm). The grinding process was undertaken by sequentially moving to a finer grid SiC sand paper (180, 330, 380, 800, 1200, fine polish) over the centre length while the sample turned in the lathe. While the centre diameter was reduced, the rest of the reduced section (40 mm) was also lightly ground to remove tool marks and scratches that could act as potential stress concentrations during testing.

Uniaxial tensile tests were carried out on a *MTS Criterion* Model 44 machine. The speed of crosshead displacement was 1.3 mm/min. The software used for capturing data was *TestWorks 4*. To measure local displacement and calculate Young's modulus, an extensometer (MFA 25) with a length of 25.4 mm was attached to the gauge length, away from the reduced section, during testing. The extensometer has an accuracy class of 0.5. The extensometer was removed from the sample once a neck began to form. Tensile test data was processed and plotted using *Matlab 2014a*.

Fracture strain was calculated by measuring the gauge length after fracture (by putting the two halves back together) and dividing by the original gauge length of 25 mm. Fracture strain is therefore presented as a percentage and along 5D (five times the gauge diameter).

4. RESULTS

This chapter lays out the results of experiments conducted as described in the methodology chapter.

4.1. SLM MACHINE ERROR

An error in the printer's functionality was discovered after samples were built. While the default hatch spacing (h) between scan tracks should be 105 µm, as shown in Figure 4.1(d) of build 1, due the machine error, two consecutive scans overlapped and the next scan skipped a track spacing, causing a gap between adjacent scan tracks of 210 µm, as shown in (b) as well as a 322 µm spacing between islands, depicted in Figure 4.1(a)). The influence of the error was noticed in samples from the second and third build but not from the first build (Figure 4.1(d)).

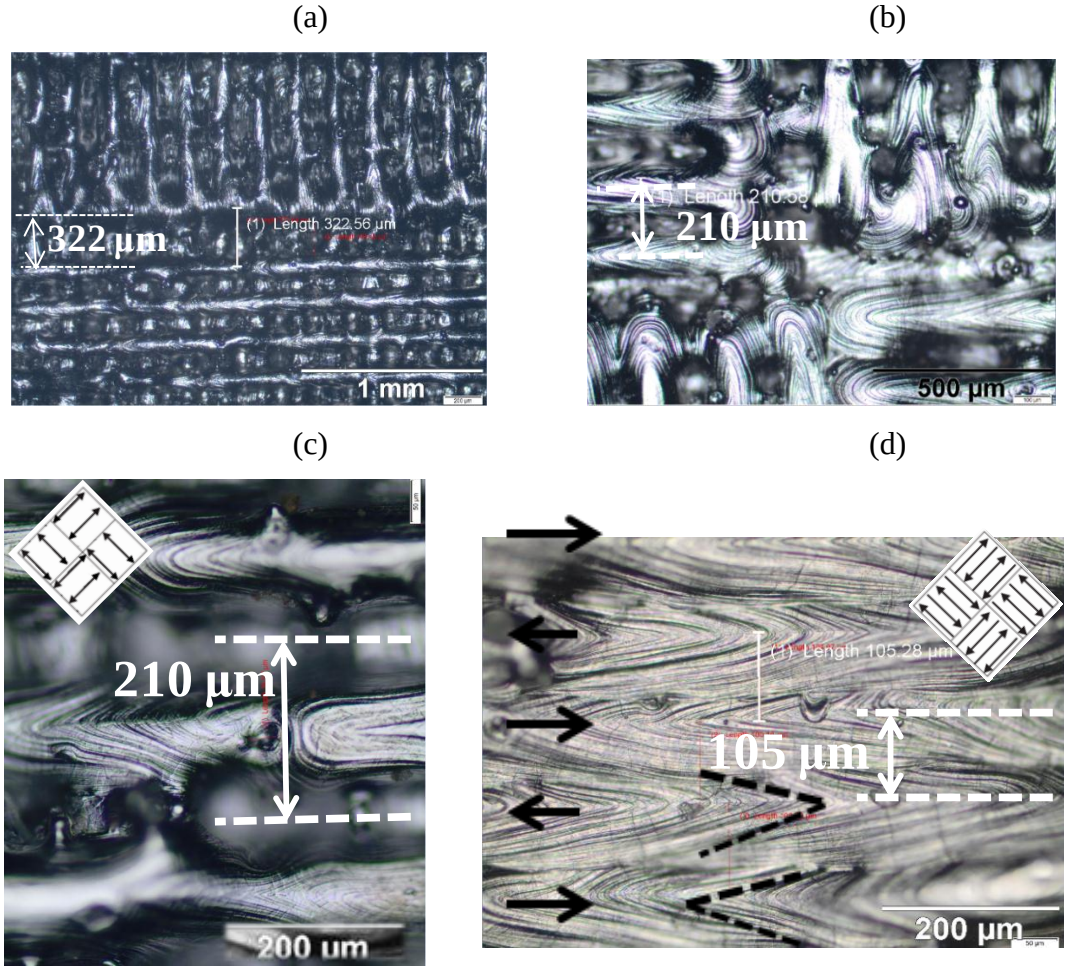

Figure 4.1: (a-c) Micrographs of affected scan track of samples from build 2 and build 3 (d) unaffected scanning surface from build 1

The effect of the SLM machine error was seen to degrade sample density of build 2 and build 3, as presented in the next section.

4.2. SAMPLE DENSITY AND DEFECTS

4.2.1. Porosity pattern and shape

Optical micrographs of the XY-plane of samples B1-7 and B2-45 in the as-built condition are depicted in Figure 4.2(a) and 2(b), respectively. A qualitative comparison of the porosity of the surfaces shows that the sample from build 2, Figure 4.2(b) has more porosity. A square-like pattern in the porosity is also apparent (emphasised by broken lines). The shape of the pores for both samples was observed to be spherical in shape and is known as a "key-hole" type defect. This type of defect is caused by an higher than optimal energy input (Kasperovich *et al.*, 2016).

(a)

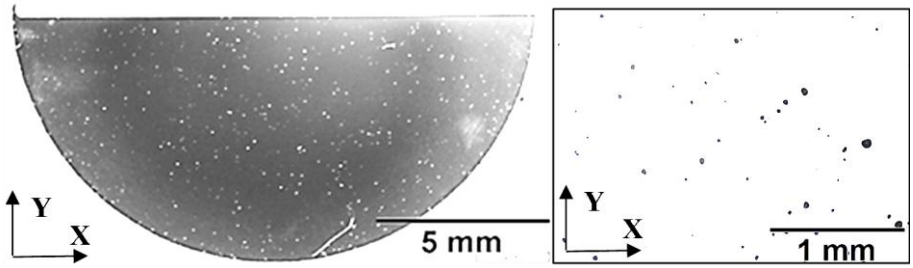

(b)

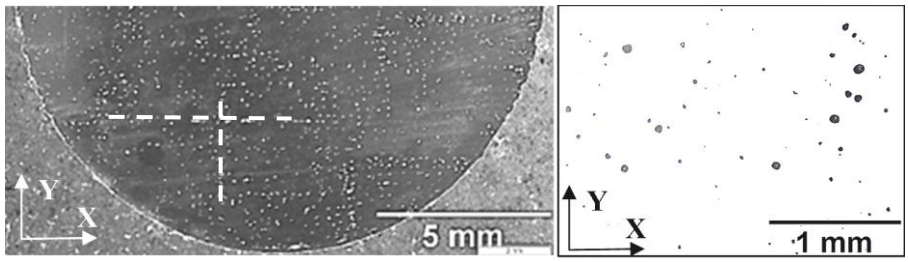

Figure 4.2: Optical micrograph of defects in XY plane (a) build 1, (b) build 2

The porosity of the horizontal sample from build 3, T2-G0-1, was evaluated and is depicted in Figure 4.3. Defect bands were observed along the ZY-plane of the sample. The pore shape was observed to be non-spherical with sharp corners. This is an indication of lack of fusion during building.

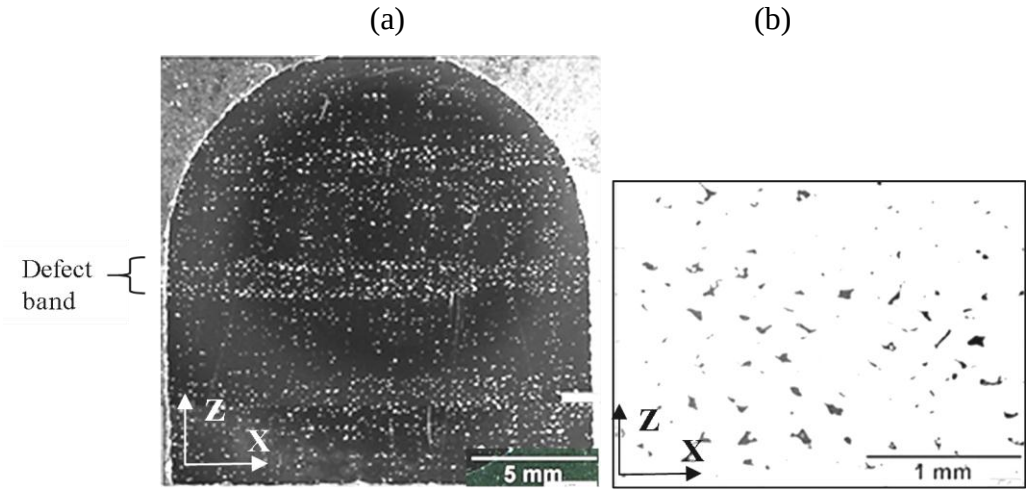

Figure 4.3: Optical micrograph of horizontal sample in ZY-plane from build 3 showing (a) defect bands and (b) defects shape

4.2.2. Sample density using the Archimedes method

Figure 4.4 illustrates a contour plot of porosity percentage of all samples from the first build superimposed with a photograph of the build itself. The measured porosity percentage of each sample is included in Appendix F. It is clear from Figure 4.4 that there is a decrease in sample density in a radial direction from the right to the left-centre of the build. Broken lines drawn on the contour plot emphasis the density contour pattern observed. The centre of the radial contour pattern coincides with the centre of the build chamber as well as the centre of argon gas flow. Sample density therefore decreases in the direction of gas flow.

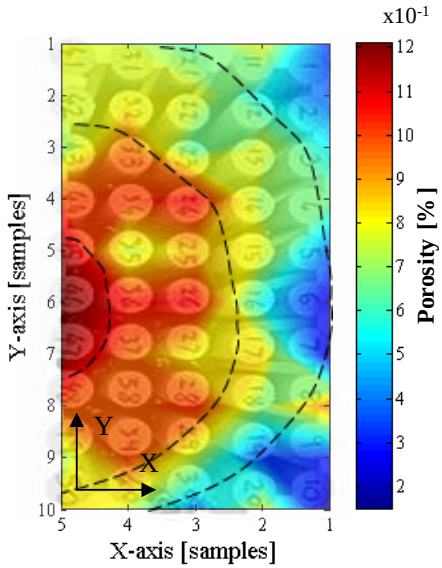

Figure 4.4: Contour plot of the measured sample porosity (broken contour lines emphasise overall trend in density)

The density of samples from builds 2 and 3, chosen for tensile tests, were also measured. Seven samples from build 2 and six from build 3 were investigated. These and density results from build 1 are tabulated in Table 4.1.

Table 4.1: Sample porosity results

Porosity statistics	**Build 1**	**Build 2**	**Build 3**
Mean [%]	0.75	0.97	1.93
Median [%]	0.78	1.00	1.89
Minimum [%]	0.15	0.69	1.60
Maximum [%]	1.22	1.29	2.42
Number of samples	50	7	6

Since build 1 achieved the best density of parts and showed no printer error influence, samples were chosen preferentially from this build for annealing and tensile tests. Although key-hole type defects are present in samples from build 1 and build 2, literature has shown that key-hole type defect with a porosity below 1 % do not have a significant impact on mechanical properties (see Section 2.12.2)

4.3. X-RAY MICRO COMPUTED TOMOGRAPHY SCANS

4.3.1. Scans of samples

A post-processed region of interest (ROI) of the CT scans of samples B1-7 and B2-45 are presented in this section. The two samples were picked from identical positions on the base plate (see Table 3.3) and are the same samples observed in Figure 4.2.

Broken lines drawn on Figure 4.5(a) and (b) emphasise two observed defect patterns. The first observed pattern is a checker-like pattern defect, shown by the small square in Figure 4.5 (a) and (b). This pattern corresponds to the repeated 1 x 1 mm square that is created by the island shift strategy. Furthermore, an increase in defect size and quantity can be seen at the boundary of 1 x 1 mm squares. This indicates that the porosity is higher at the end of a scan vector. This has also been found by Khairallah *et al*. (2016). This is most probably due to the laser (speed) slowing down to make the turn. Due to a slower laser speed at the end of the vector, the laser energy density is higher and therefore above optimal. This causes the melt pool to boil over which causes material to evaporate and a “key-hole” melt pool mode to form (Yang *et al.*, 2016).

The parallel cross-shaped lines, shown in Figure 4.5(b), emphasise the second observed defect pattern. The spacing of the defect lines measure double the set process hatch spacing (of 105 µm) and is most likely caused by the missed scan vector error observed in build 2. This pattern is not observed in build 1, Figure

4.5(c), since the printer error was absent in this build session. Porosity data obtained from the CT scans are tabulated in Table 4.2.

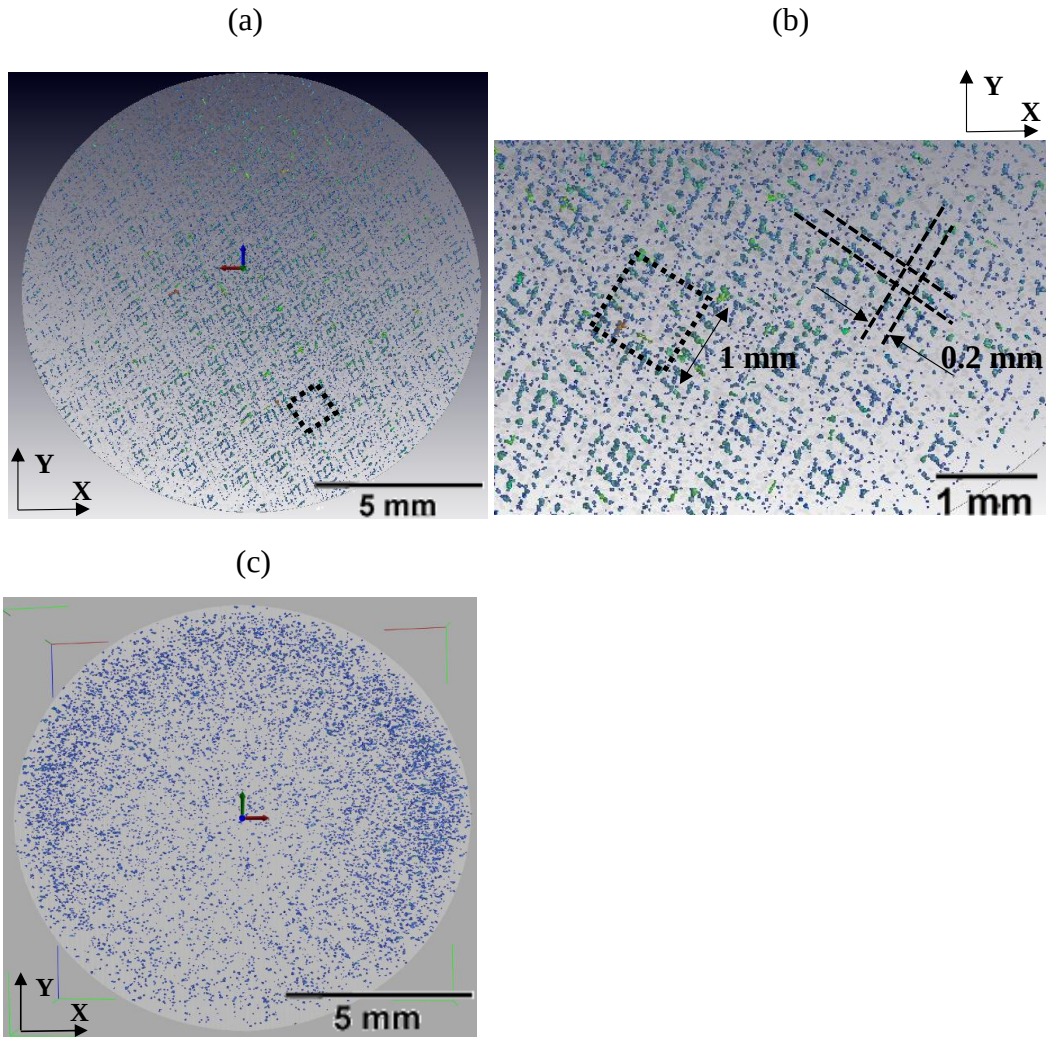

Figure 4.5: CT scan ROI of (a) B2-45 top view (b) Magnified view of top view, (c) B1-7 top view

Table 4.2: CT scan graphical analysis statistics

	Sample B1-7	**Sample B2-45**
Porosity measured from CT software [%]	0.23	0.50
Maximum detected defect diameter [mm]	0.25	0.31

Histograms of defect diameter size, as determined using the CT scan post-processing graphical software, of the two samples are depicted in Figure 4.6(a) and (b), respectively. Both samples have approximately the same defect size

distribution. While the sample from build 1, Figure 4.6(a), shows a peak frequency at approximately 50 µm diameter, and then a decrease in frequency below 50 µm, the sample from build 2, Figure 4.6(a), does not show a decrease in porosity frequency for low defect diameters. This indicates that build 2 had a higher number of smaller size defects. The defect diameter distribution of build 2 appears denser than build 1.

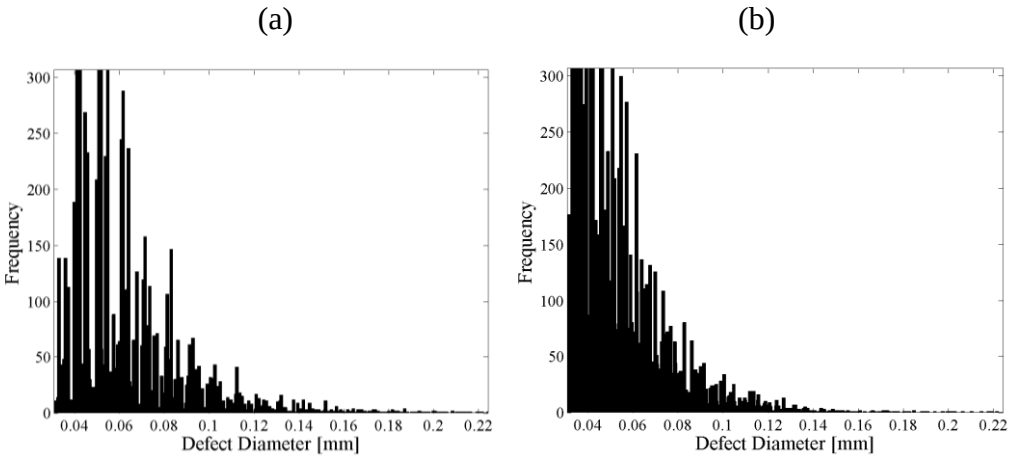

Figure 4.6: Histogram of defect diameter size of RIO: (a) B1-7 (b) B2-45

4.4. OPTICAL MICROSTRUCTURAL ANALYSIS

Optical micrographs are useful to obtain qualitative information about microstructural features such as grain size and phase distribution. Since the as-built samples do not contain a significant amount of β phase, etching does not bring out grain structure. DIC, as discussed in the literature review (Section 2.13.1 and 3.9.1), was used to distinguish α' grains. Micrographs of annealed samples were taken at the same magnification to compare grain size between samples.

4.4.1. Oxygen penetration depth

Measurements of α case depth and total penetration depth of oxygen is tabulated in Table 4.3. All micrographs from which the measurements were made are included in Appendix B.2. The results show that the hardness decreases from the α case region ~800 HV0.05 to the sample's internal hardness of ~350 HV0.05 after approximately 300 µm. The micrographs of this micro-indentations made from the surface are attached in Appendix B.2. Both the air and slurry coated samples underwent a heat treatment at ~1030 °C for 4 hours followed by furnace cooling, while the vacuum annealed sample was annealed at 950 °C for 4 hours followed by furnace cooling.

In a sample with the highest oxygen penetration measured a penetration of 351 µm. This is well below the depth of material removed from the tensile samples in the study and therefore validated the use of an air environment for heat treatments.

Table 4.3: Oxygen contamination results

	Air (Figure B.2)	Slurry coated (Figure B.3)	Vacuum (Figure B.4)
α case [µm]	109	21	negligible
Total penetration [µm]	351	252	~50

4.4.2. As-built microstructure

Figure 4.7 depicts a micrograph of sample B1-15. The expected fine needle-like α' phase of the as-built sample can be seen. The observed black lines in the figure are shadows caused by the topography of the crystal structure (contrasted using DIC). Grains predominantly span the shortest length of the prior-β grain. The primary and secondary α' are distinguishable. Primary α' grains are the large grains (0.5 - 1 µm) that have a twin-like appearance, while the secondary α' grains take up the space between the primary α' grains and are much smaller in scale (<0.5 µm).

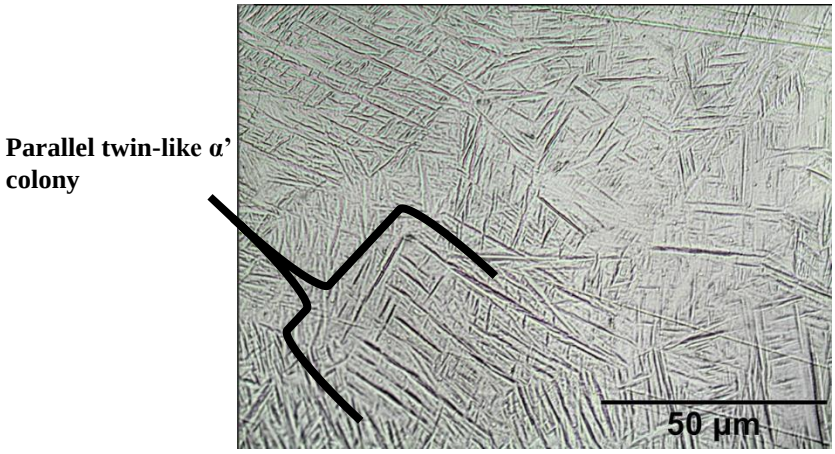

Figure 4.7: XY-plane of as-built sample B1-15

4.4.3. Low temperature strategy T2-G2 (~600 ºC)

This strategy was aimed at relieving residual stress as well as investigating the influence of the heat treatments on the microstructure of the samples.

β phase precipitation is visible in the micrograph of sample T2-G2-1 depicted in Figure 4.8 (small black particles). The precipitation also appears to be more concentrated at prior-β grain boundaries. The samples were analysed using SEM to confirm that these particles are in fact vanadium-rich and therefore β phase (Section 4.6). The low temperature stress relief strategy therefore does cause a microstructural change from as-built, and does not only relieve the residual stresses in the sample (as previously assumed).

4.4.4. Recrystallisation annealing strategy

Recrystallisation annealing was conducted by heating the samples in the solid-solution temperature region (between ~750 ºC to $\beta_{transus}$) to decompose α'/α'' → (α+β).

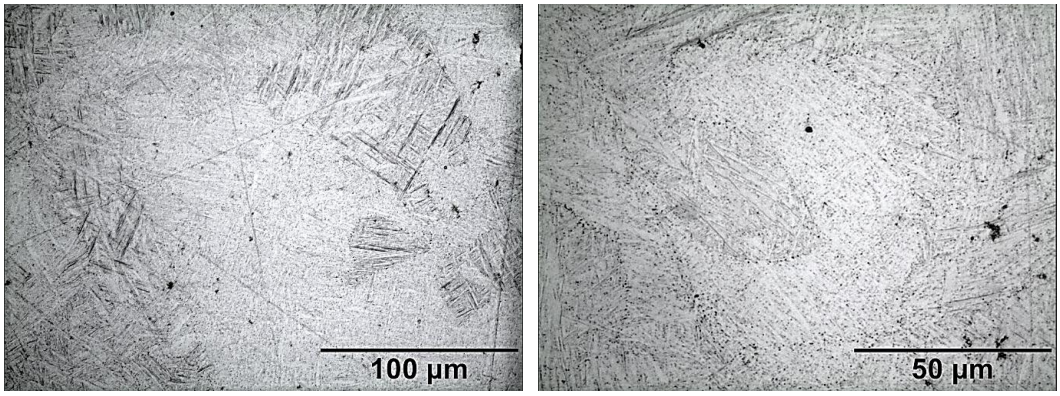

Figure 4.8: Ultra-fine β precipitation of sample T2-G2-1

T1-G4 (furnace centre temperature ~770 ºC)

Micrographs of sample T1-G4-1 are presented in Figure 4.9(a). The β phase is observed at α triple points and grain boundaries (black particles). The particle/precipitate-like appearance of the phase suggests that the phase is more concentrated at triple points. Identification of complete α grains is challenging due to the fineness of the α grain structure and the lack of β phase on the boundaries of some grains.

T1-G1 (furnace centre temperature ~870 ºC)

Micrographs of the sample T1-G1-1 are displayed in Figure 4.9(b). Increased decomposition of small α'/α grains is apparent. The grain structure is more pronounced as compared to that observed in the previous sample (T1-G4-1). It appears that the fineness of the α'/α'' structure has decomposed to a lamellar-like (α+β). The grain sizes of samples T1-G4-1 and T1-G1-1 were measured using the line intercept method (automated in *Matlab*). The average grain diameter of sample T1-G4-1 was measured as 1.87 um, while that of sample T1-G1-1 was 2.94 um. Globularisation of grains was observed, as indicated by the black arrows in Figure 4.9(b). The globularisation appeared preferentially at prior-β grain boundaries.

Additional sample annealed at 950 ºC

An additional sample was annealed at 950 ºC for one hour, followed by furnace cooling, by the final year mechanical engineering student, Luke Davis. Micrographs of the sample, Figure 4.9(c), reveal a large amount of grain growth. Complete recrystallisation of small grains to large α gains is visible when compared to the micrograph of T1-G1-1.

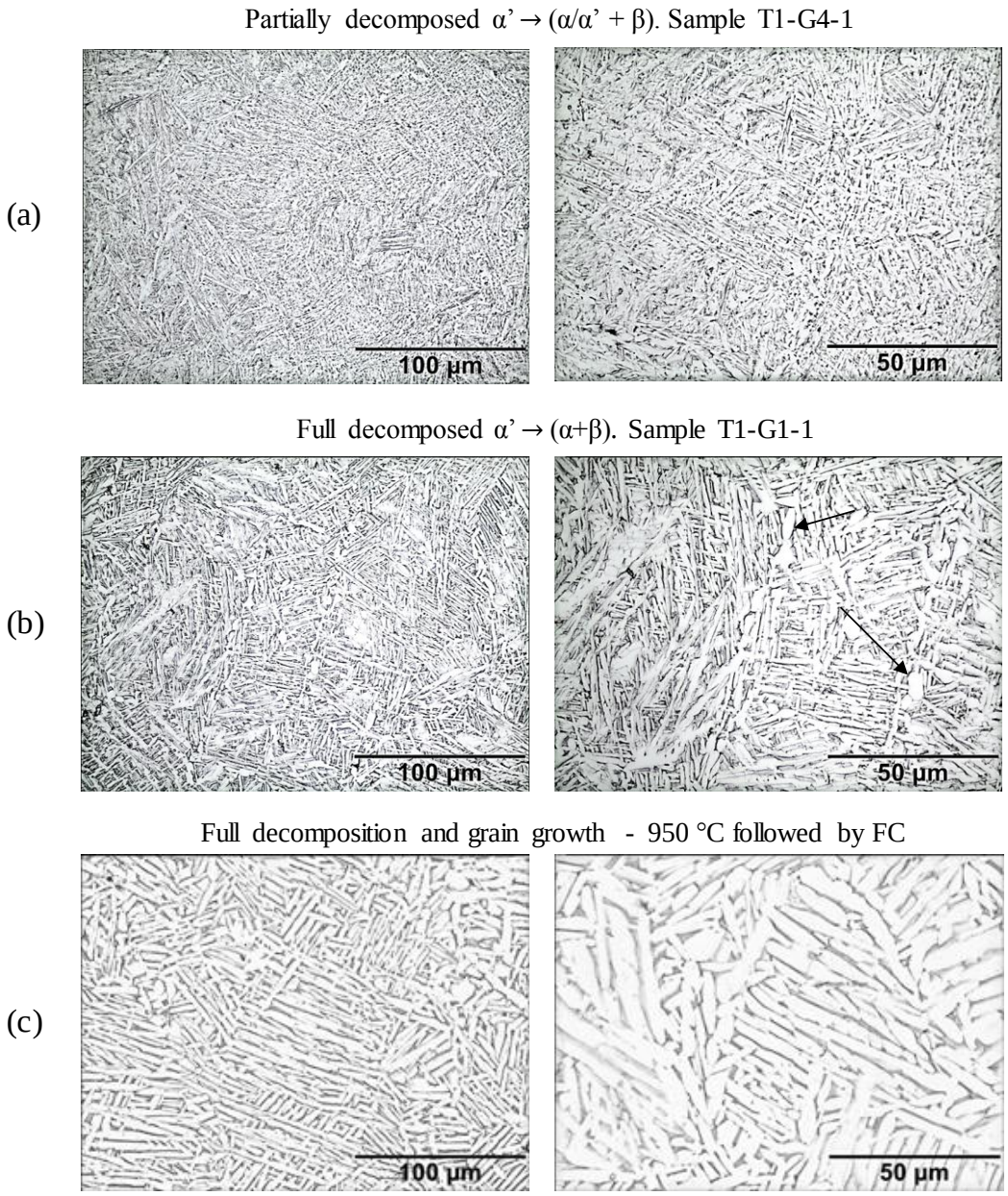

Figure 4.9: Micrographs showing α' decomposition and grain growth kinetics as a function of annealing temperature of (a) T1-G4-1, (b) T1-G1-1, (c) additional sample

4.5. BI-MODAL AND BI-LAMELLAR MICROSTRUCTURES

Bi-modal microstructures were achieved in three heat treatment strategies. The first group occurred unintentionally by cooling from above the β transus to approximately 20 ºC below the β transus (~960 ºC). This caused the microstructure to first homogenise to β and then nucleate and grow α phase at β phase grain boundaries, as shown in Figure 4.10. Since the holding time at ~960 ºC was eight

hours, grain boundary α grew to a large size. The sample was then air cooled and recrystallised at 750 ºC for 3 hours followed by air cooling.

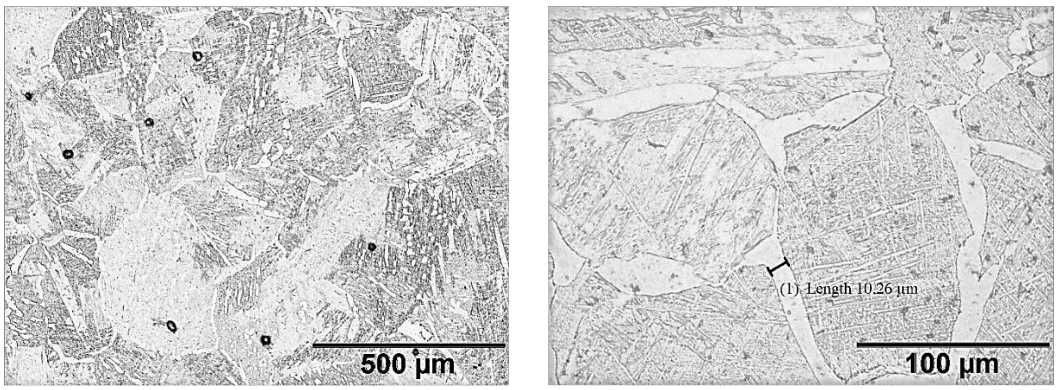

Figure 4.10: Grain boundary bi-modal microstructure of sample T2-G1-2

The second bi-modal microstructure (Figure 4.11 - sample T2-G6-3) was achieved by heating to approximately 10 - 20 ºC below the β transus (without exceeding it) and holding there for 8 hours. The globalisation of α grains can be seen in the figure. The sample was water quenched and then annealed at 870 ºC for 4 hours followed by air cooling.

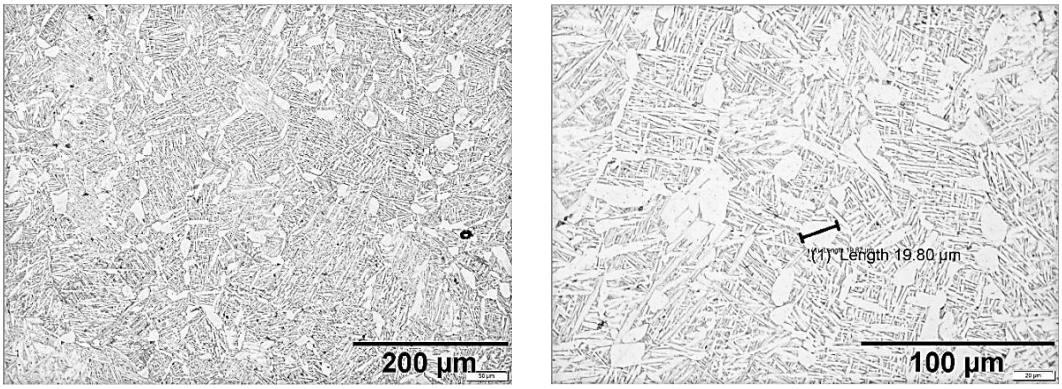

Figure 4.11: Bi-modal microstructure achieved (~960 ºC 4hrs hold, WQ followed by 870 ºC air cooled) for sample T2-G6-3

The third bi-modal microstructure is more accurately described as bi-lamellar due to the shape of α grains remaining predominantly long and lamellar-like. Figure 4.12(a) depicts the microstructure of sample T2-G3-3 which was held at ~910 ºC for 8 hours, then water quenched and recrystallisation annealed at 750 ºC for four hours followed by furnace cooling. Quenching from a higher temperature, such as 930 °C of sample T2-G3-1, Figure 4.12(b), promotes transformation to the β phase and results in a larger percentage of secondary α.

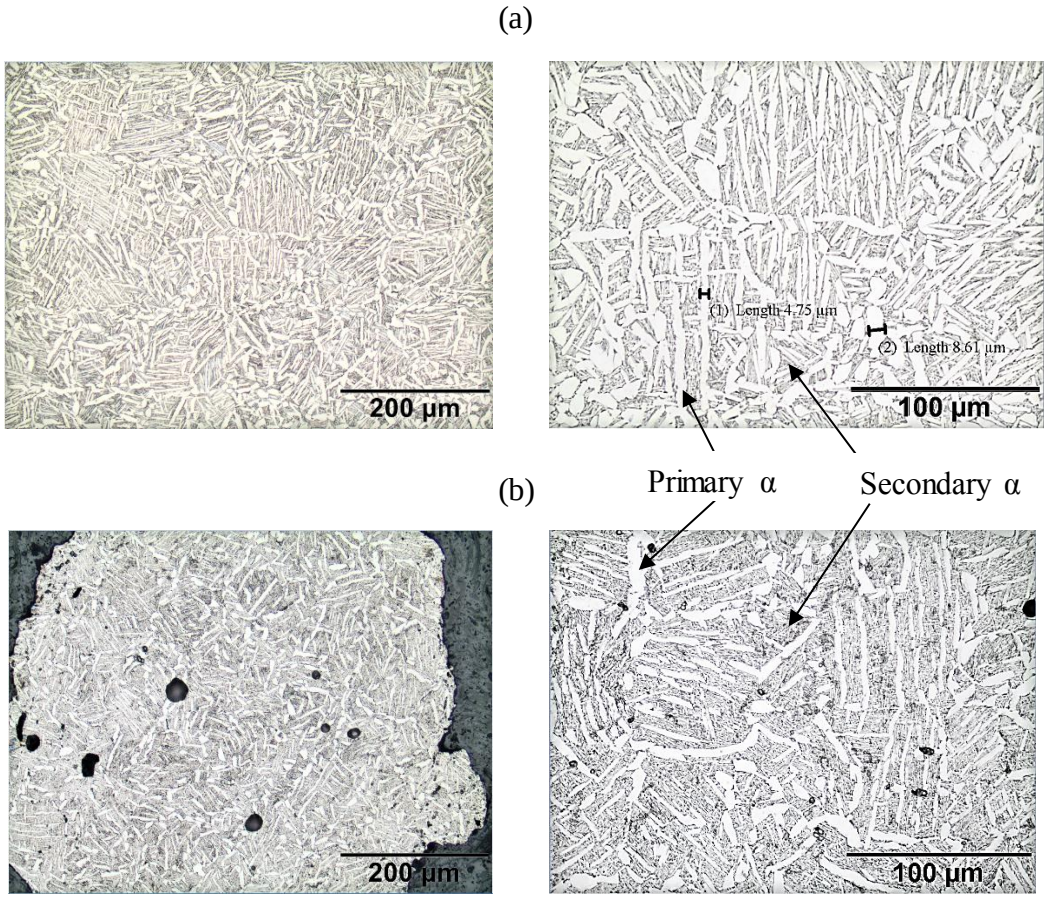

Figure 4.12: Bi-lamellar microstructure achieved Sample T2-G3-3 (WQ from ~910 ºC) and T2-G3-1 (WQ from ~930ºC)

4.6. SEM ANALYSIS OF LOW TEMPERATURE ANNEAL STRATEGIES

SEM micrographs of samples heat treated at 510 ºC and 600 ºC (samples T2-G2-4 and T2-G2-1 respectively) are shown in Figure 4.13. Since heavier elements appear lighter in a SEM images, areas in a SEM image that have a high concentration of vanadium appear lighter (in contrast to optical micrographs, where the concentration of vanadium appears darker due to the formation of β phase). The SEM images in Figure 4.13 show that the sample heat treated at 600 ºC contains β phase precipitation (that is rich in vanadium because of solute partitioning) at grain triple points and boundaries (this was also observed by other literature studies, see Figure 2.4(c)). No β phase precipitates are visible in the sample heat treated at 510 ºC and therefore the microstructure of Figure 4.13(a) contains only α' grains. This agrees with that discussed in Section 2.1.2.

(a) (b)

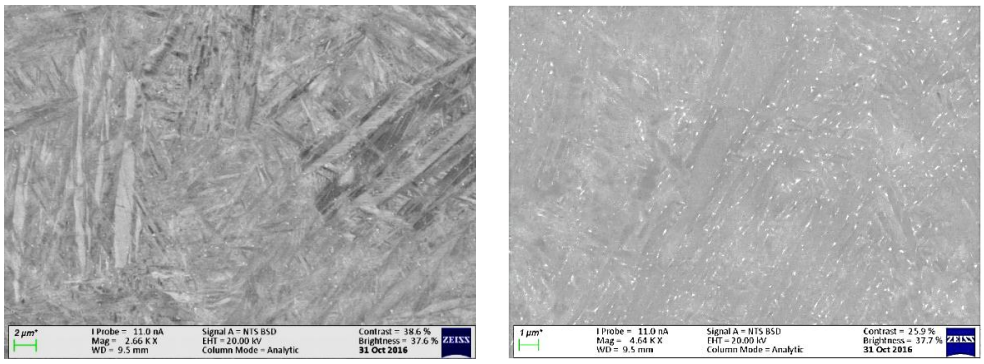

Figure 4.13: SEM images of samples heat treated at (a) 510 °C and (b) 600 °C both for 8 hours

4.7. EBSD ANALYSIS

4.7.1. Variant selection

Variant selection during SLM was investigated by calculating the variant type of each α' grain orientation of the XY-plane of the vertically as-built sample, as described in Chapter 3.9.5. Figure 4.14 depicts both the histogram of the variant type and α'-α' misorientation angle. A comparison in frequency of theoretical percentage and measured values is tabulated in Table 4.4.

(a) (b)

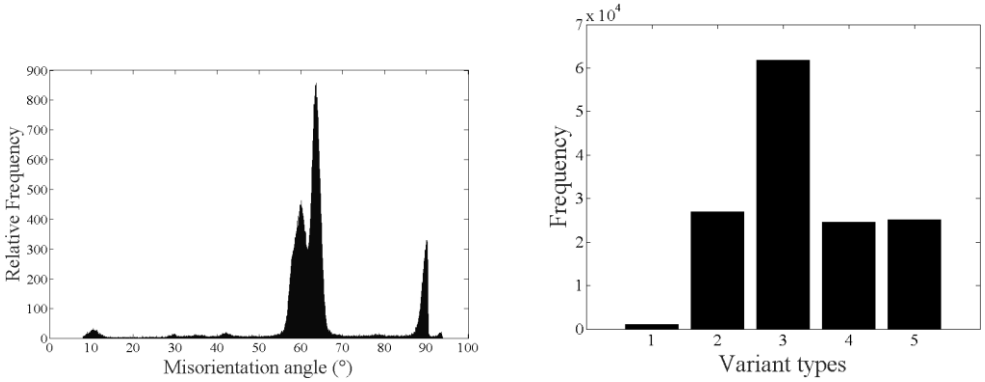

Figure 4.14: (a) Histogram plot of (a) α' misorientation angle, (b) calculated variant types

Table 4.4: Variant selection data

Type, misorientation angle and axis	**Theoretical variant [%] Wang *et al.* (2003)**	**Measured α variant [%]**	**Measured α/α misorientation [%]**
Type 1 = 10.53º, [0 0 0 1]	9.1	0.74	1.6
Type 2 = 60º, [1 1 $\bar{2}$ 0]	18.2	19.3	20.8
Type 3 = 60.83º, [$\bar{1.38}$ $\bar{1}$ 2.38 0.359]	36.4	44.3	21.8
Type 4 = 63.26º, [$\bar{10}$ 5 5 $\bar{3}$]	18.2	18.6	40.3
Type 5 = 90º, [1 $\bar{2.38}$ 1.38 0]	18.2	18.1	15.5
TOTAL	100	100	100

4.7.2. As-built orientation maps

Orientation maps of both α' and reconstructed prior β phase are presented in Figure 4.15. Pole figures and inverse pole figures of the scans of both α' and reconstructed β phase are depicted in Figure 4.16.

The spacing of parallel lines coincided with laser hatch spacing (h) of 105 µm. The perpendicularly of the lines coincides with the 90 º alternating scan direction of each consecutive layer. The ZX-plane of the reconstructed prior β phase depicts a columnar β grain shape. The morphology of the reconstructed phase maps is identical to that of the recrystallisation annealed samples depicted in Figure 4.18 and Figure 4.21.

4.7.3. Recrystallisation strategy orientation maps

EBSD orientations maps of the α phase and reconstructed β phase of the T1-G4-1 and T1-G1-1 samples are depicted in Figure 4.18 and Figure 4.21, respectively. Their respective pole figures and inverse pole figures of each phase are depicted in Figure 4.19 and Figure 4.20.

The reconstructed β phase texture

The cross-shape traced with broken lines in Figure 4.23 emphasises the texture created by the alternating scanning strategy of the laser. All β phase IPFs show a [001] texture in the direction of the build.

The α phase texture

The α phase crystals of all samples showed a weak texture in which the (0001) poles are preferentially orientated 30-45 º from the sample Z-axis.

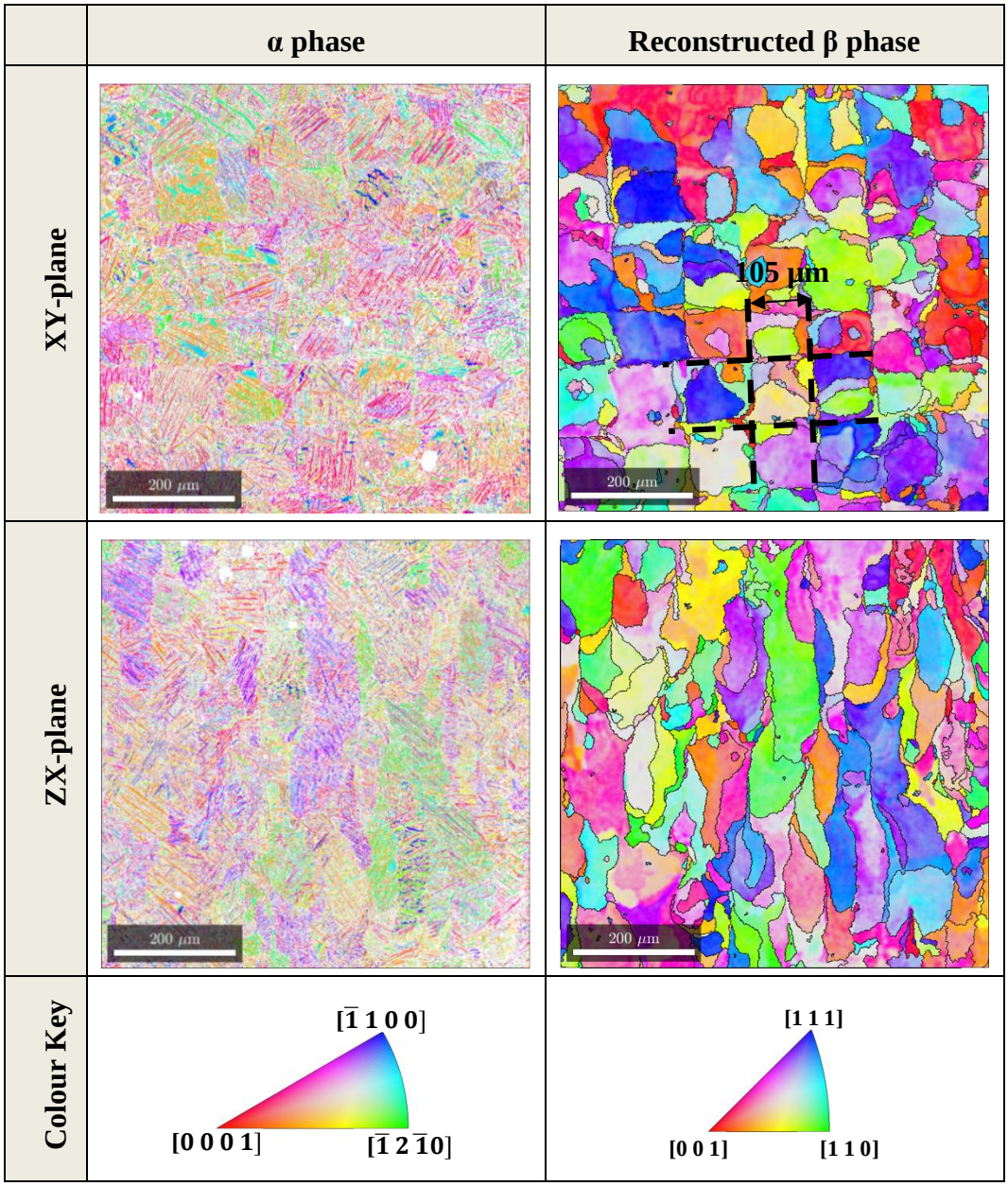

Figure 4.15: Orientation maps of as-built sample B1-15

	Pole figures	Inverse pole figures
XY-plane	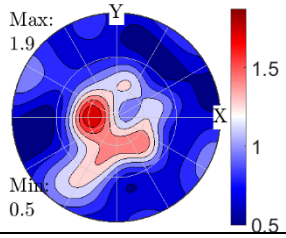	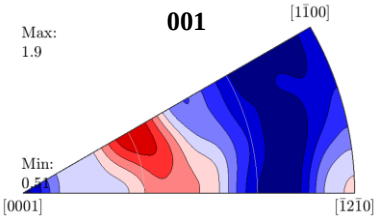
ZX-plane	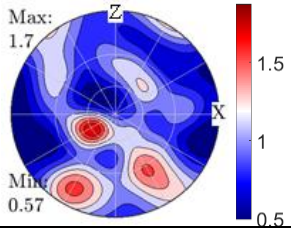	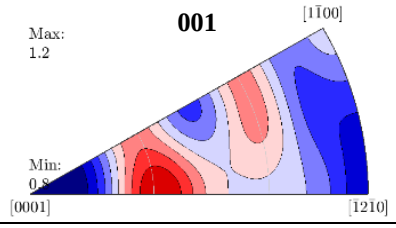

Figure 4.16: α phase: (0 0 0 1) pole figure and [0 0 1] inverse pole figures as-built sample B1-15

	Pole figures	Inverse pole figure
XY-plane	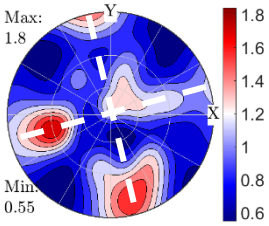	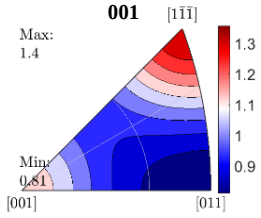
ZX-plane	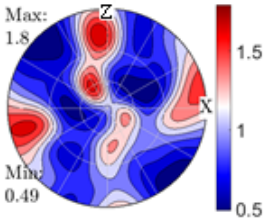	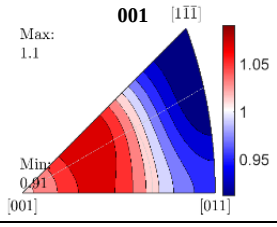

Figure 4.17: Reconstructed β phase: (0 0 1) pole and [0 0 1] inverse pole figures as-built sample B1-15

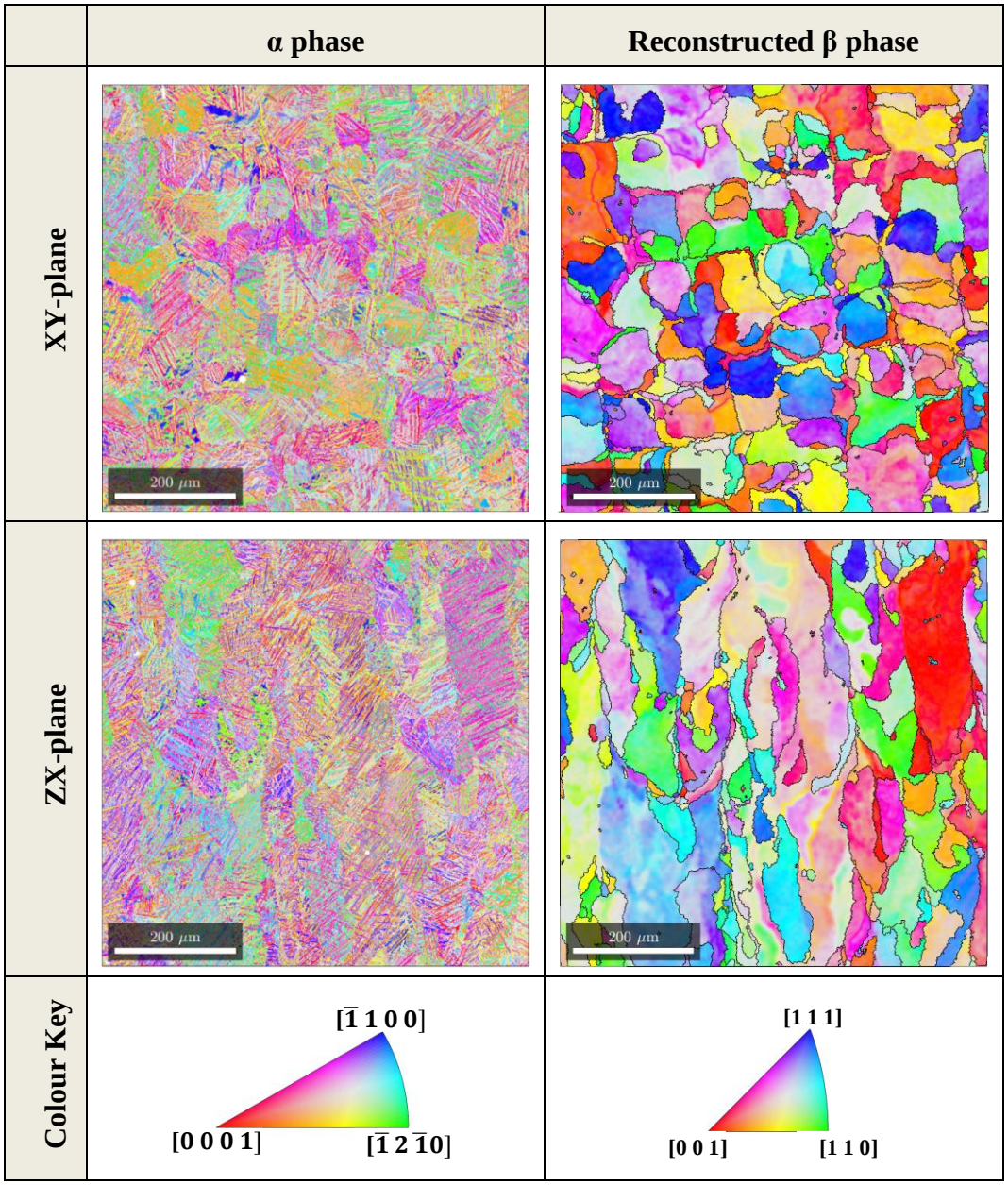

Figure 4.18: Orientation maps of T1-G4-1 (~770 ºC)

	Pole figures	Inverse pole figures
XY-plane	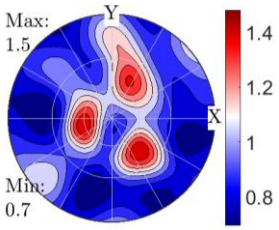	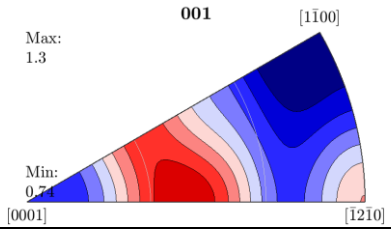
ZX-plane	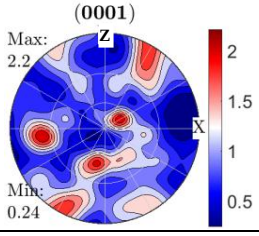	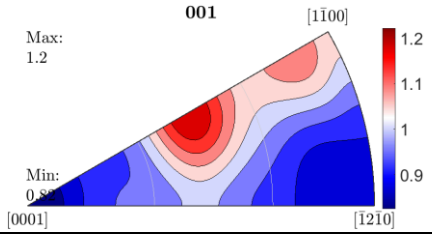

Figure 4.19: α phase: (0 0 0 1) pole and [0 0 1] inverse pole figures of T1-G4-1 (~770 ºC)

	Pole figures	Inverse pole figures
XY-plane	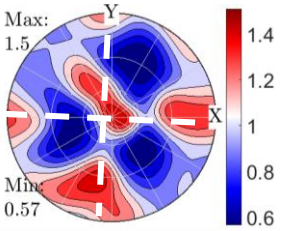	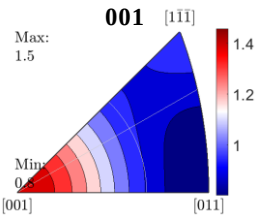
ZX-plane	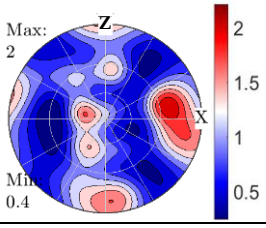	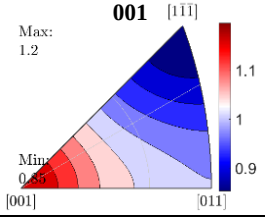

Figure 4.20: Reconstructed β phase: (0 0 1) pole and [0 0 1] inverse pole figures of T1-G4-1 (~770 ºC)

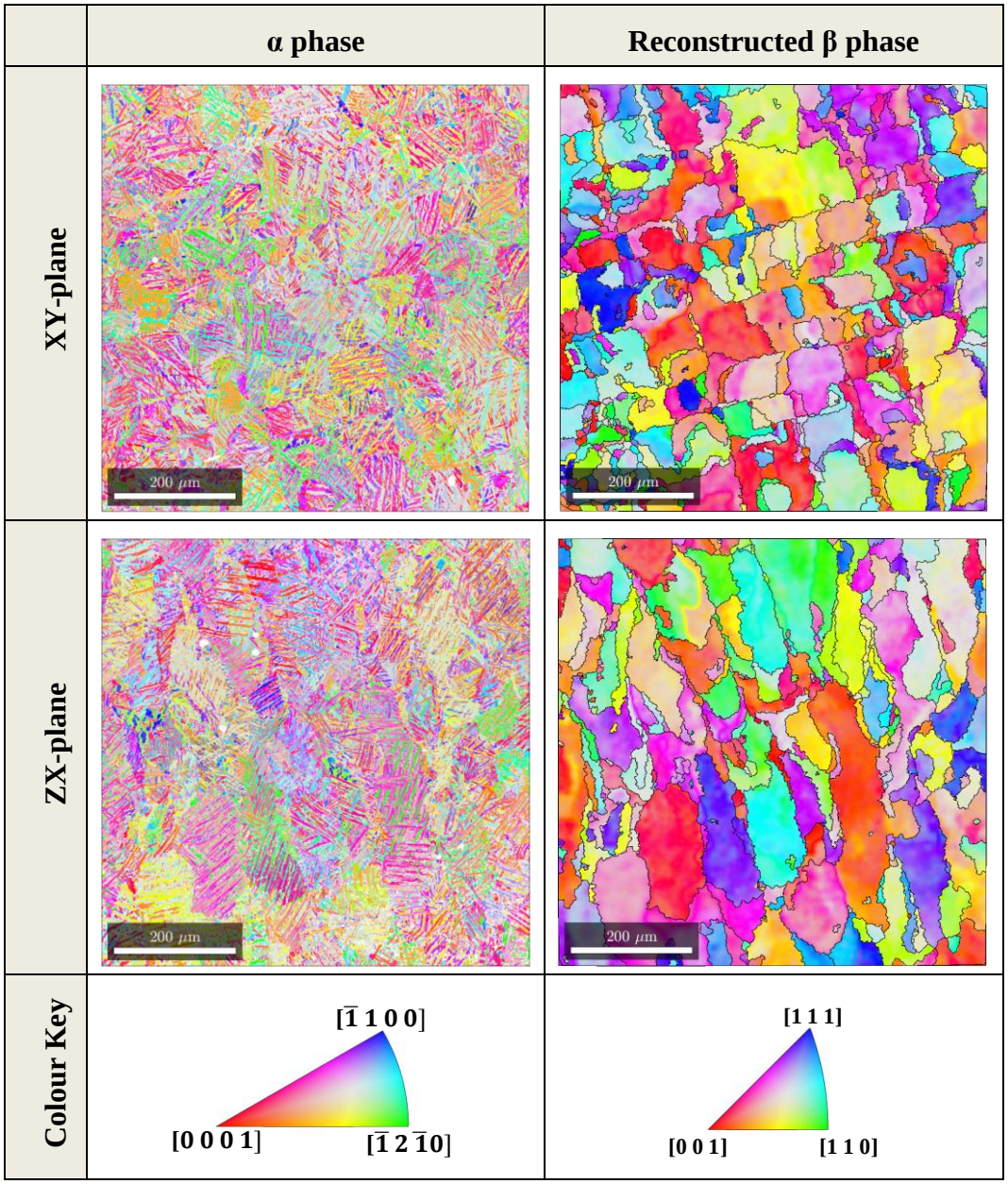

Figure 4.21: Orientation maps of T1-G1-1 (~870 ºC)

	Pole figures	Inverse pole figures
XY-plane	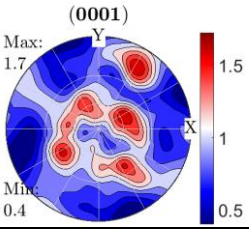	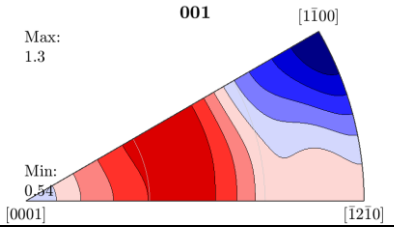
ZX-plane	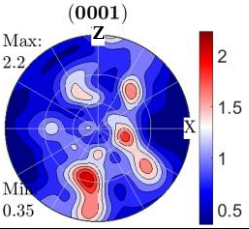	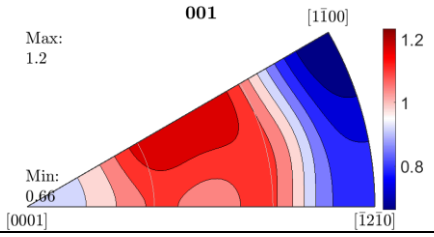

Figure 4.22: α phase: (0 0 0 1) pole and [0 0 1] inverse pole figures of T1-G1-1 (~870 °C)

	Pole figures	Inverse pole figures
XY-plane	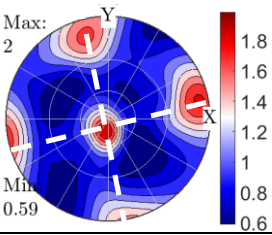	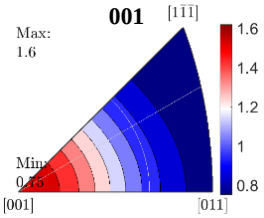
ZX-plane	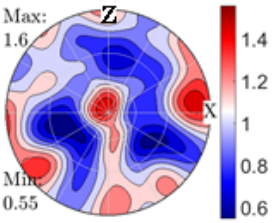	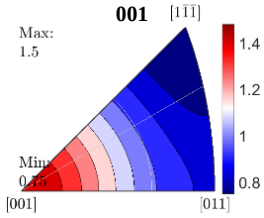

Figure 4.23: Reconstructed β phase: (0 0 1) pole and [0 0 1] inverse pole figures of T1-G4-1 (~870 °C)

4.7.4. β-Anneal strategy

Figure 4.24 depicts the IPF orientation map of the α phase of the XY-plane of sample T1-G2-1. Black lines on α grain boundaries represent prior-β grain boundaries (calculated from α/α misorientation angle as discussed in Section 2.3.1). The enlargement of β grains can clearly be seen as compared to the recrystallised and as-built samples. Large colonies of α grains are observed (indicated by black arrows). Figure 4.25 shows the pole and inverse pole figures of sample T1-G2-1.

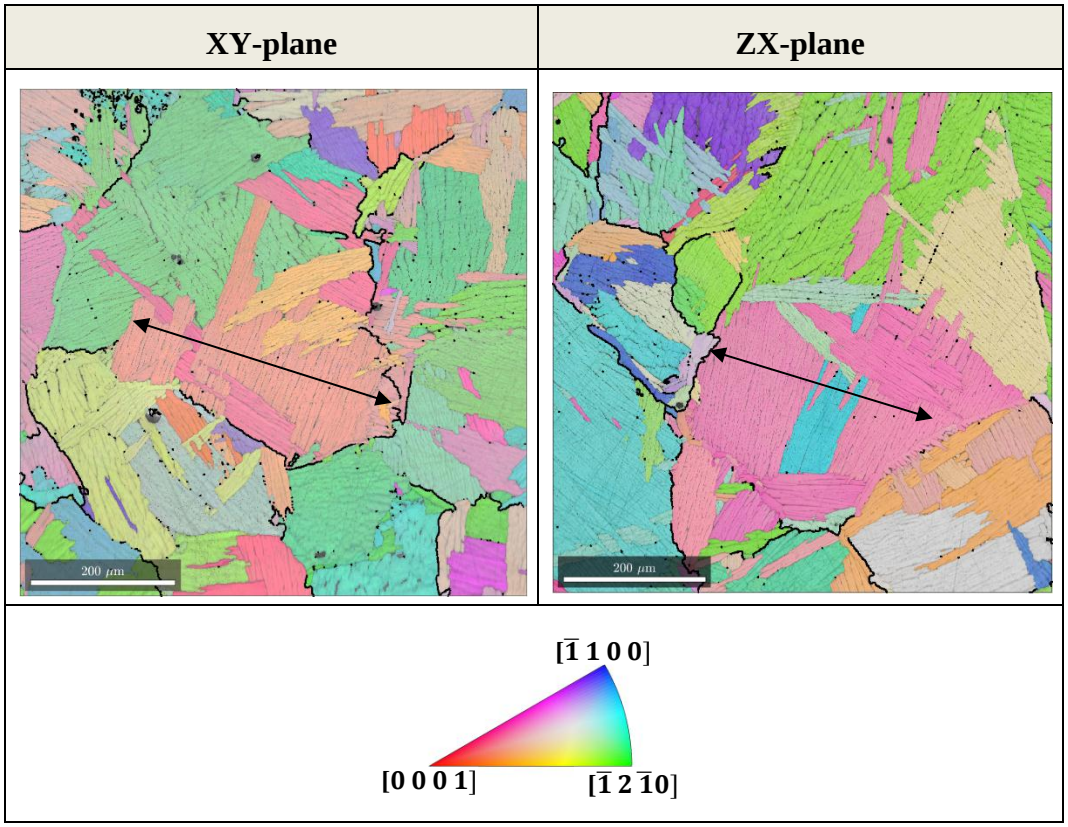

Figure 4.24: IFP Orientation map of T1-G2-1 (β-anneal, FC)

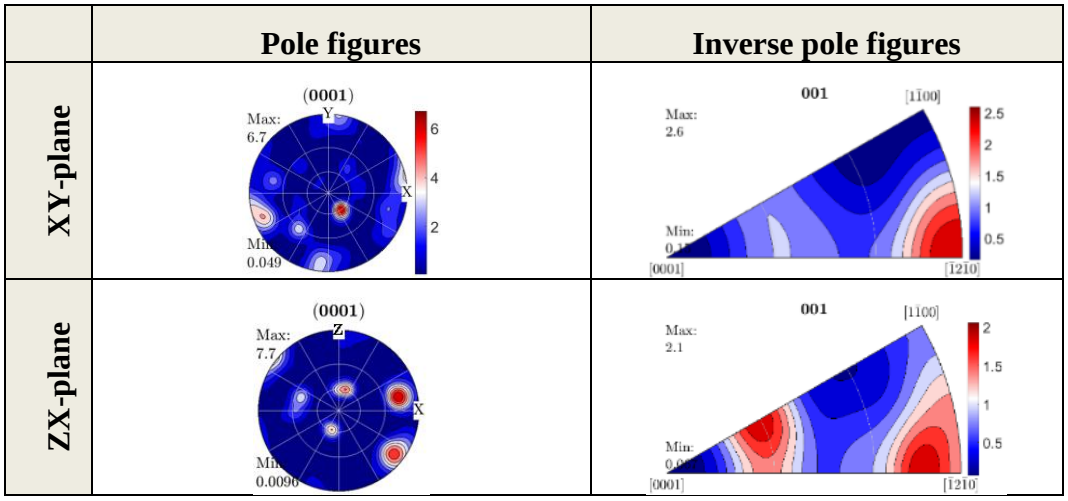

Figure 4.25: [001] inverse pole figures of T1-G2-1 (β-anneal, FC)

4.8. MICRO-HARDNESS

The measured micro-hardness of the as-built (Z-orientated), low temperature annealed and recrystallised annealed samples are summarised in Table 4.5. The micro-hardness of the as-build sample match that of the theoretical hardness of α' (Crespo 2011: 326). A larger scatter in data was observed for the as-built sample, compared to the rest of the samples. Recrystallised samples show a decrease in hardness with an increase in temperature. The sample annealed at 510 ºC showed an increase in micro-hardness.

Table 4.5: Vickers micro-hardness measurements

	Measurement in sample XY-plane [HV/2]		
Sample and annealing temperature [ºC]	**Median**	**Max**	**Min**
As-built (Z-built)	350	367	315
T2-G2-4 (~510)	380	389	370
T2-G4-1 (~600)	350	355	323
T1-G4-1 (~770)	315	320	280
T1-G1-1 (~870)	305	310	288

4.9. TENSILE TESTS

4.9.1. Influence of porosity on tensile behaviour

Young's modulus calculated by fitting a straight line through the stress vs local strain (extensometer strains) data using *Matlab*'s "polyfit" function. The gradient of the line was then taken as the Young's modulus. The influence of porosity on Young's modulus can be seen by the trend in data plotted in Figure 4.26. Sample stiffness appears to decrease with an increase in porosity above a porosity percentage of 1 %.

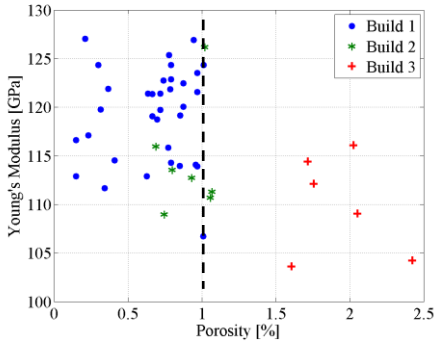

Figure 4.26: Plot Young's modulus vs porosity percentage for all samples

The influence of porosity percentage on ductility (fracture elongation in $G = 5D$) is plotted in Figure 4.27. There is no apparent trend in data when all samples are plotted due to the large scatter in data points. A trend is clear in the recrystallisation group, Figure 4.27(b). Fracture elongation percentage decreases with an increase in porosity.

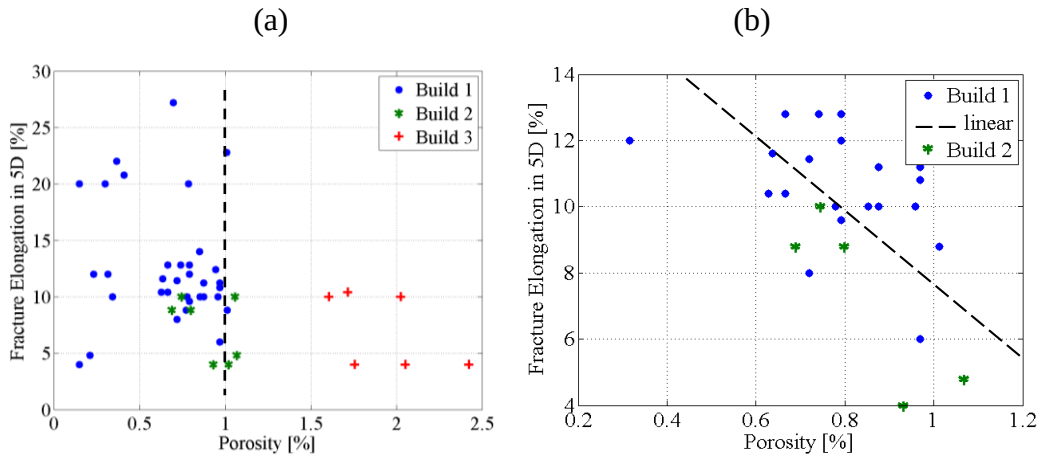

Figure 4.27: Fracture elongation percentage in 5D vs porosity percentage for (a) all samples, (b) recrystallisation groups (T1-G1, T1-G3, T1-G4, T2-G4)

4.9.2. Influence of annealing temperature on tensile behaviour

The influence of annealing temperature on fracture elongation and UTS is plotted in Figure 4.28. While no clear trend in data of fracture elongation vs temperature is visible for the temperature range 740 – 880 ºC, a clear drop in UTS can be seen at 780 – 800 ºC.

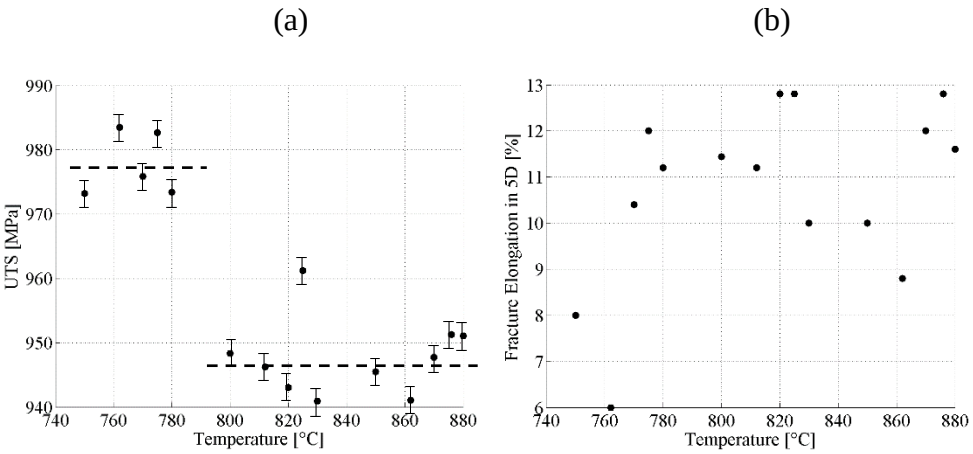

Figure 4.28: Recrystallisation temperature vs (a) ductility and (b) ultimate tensile strength

The influence of annealing temperature on Young's modulus is presented in Table 4.6. Only samples from build 1 were compared to eliminate the influence of

excessive porosity on the results. The Young's modulus of the as-built sample increases with annealing temperature to a maximum of 122.7 GPa at ~870 ºC. While the theoretical Young's modulus of α is 117 GPa; results show an increase beyond this stiffness with an increase in annealing temperature. Two outliers in sample batch temperature T1-G4 (with a furnace centre temperature of ~770 ºC) that fractured at 6% and 8% decreased the median fracture elongation from 11.2 % to 10.4 %. Samples annealed at 820 ºC and 870 ºC had the same minimum fracture elongation of 10 % and a maximum fracture elongation of 12.0 % and 12.8 % respectively. Poor fracture elongation was recorder for the low temperature annealing group of (median of 4.80 %).

Table 4.6: Correlation between temperature and tensile behaviour

Group and group furnace centre temperature [ºC]	**Median Young's modulus [GPa]**	**Median fracture elongation in 5D [%]**
As-built	114	10.0
T2-G2 (~600)	117	4.80
T1-G4 (~770)	120	10.4 (11.2 excluding outliers)
T2-G4 (~820)	122	11.4
T1-G1 (~870)	123	11.6

4.9.3. Correlation between strength and ductility

Fracture elongation percentage vs sample UTS is plotted in Figure 4.29. Heat treatment groups are circled with a standard deviation of 2. The trend in data is emphasised by the broken curved line. Groups B and F show the least amount of scatter in ductility.

It is proposed that the scatter in ductility for samples in groups D and C was caused by the combined effects of a high stress state and the presence of pores. The low ductility of groups A and G are due to the poor density of samples from these builds.

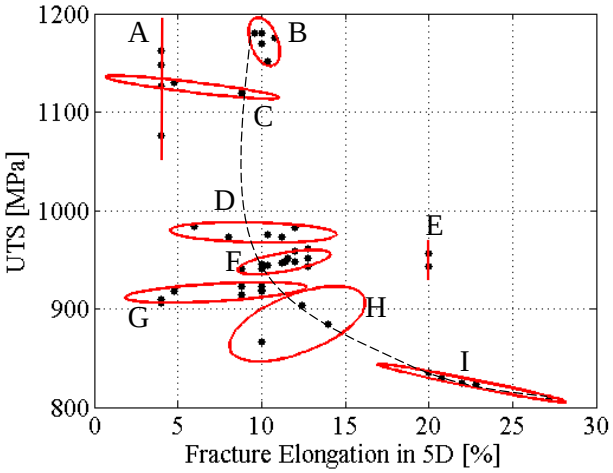

A	T2-G0
B	T1-G0
C	T2-G2
D	T1-G4
E	T2-G3
F	T1-G1, T1-G3
G	T2-G4
H	T2-G1
I	T1-G2

Figure 4.29: UTS's vs fracture elongation in 5D for all samples.

The annealing temperatures of recrystallisation groups D, F and G compare as D>F>G. Due to the linear relationship between grain size and temperature, and since a larger grain size corresponds to a low strength, a trend between strength and temperature was shown. The lower ductility measured in group G is argued to be due to the group's higher porosity causing premature failure in some samples. The lower strength in group H is due to the large grain boundary α seen in the microstructure of a sample from this group (Figure 4.10). The higher ductility measured in groups E and I is argued to be due to the combined effects of a higher percentage of β phase and a larger α phase grain structure. The high strength of group E, compared to group I, is due to the fine secondary α phase created from quenching the sample from the solid-solution phase field.

4.10. FRACTURE SURFACE FEATURES

The fracture surface of sample T2-G3-3 is depicted in Figure 4.30. Small spherical pores are seen on the surface. These pores are evenly spread and do not have the appearance of the common 'dimple' seen on fracture surfaces of ductile metals. It is suggested that these pores are plastically enlarged from existing internal pores caused by SLM processing.

Figure 4.30: Fracture surface of bi-lamellar (T2-G3-3)

Pore nucleation can be seen below the fracture surface of sample T2-G3-1, Figure 4.31. This nucleation is most concentrated at the outside of the sample. Pore nucleation and coalescence around existing pores can be seen in the micrograph of sample T1-G1-1, Figure 4.31 (b) and (c).

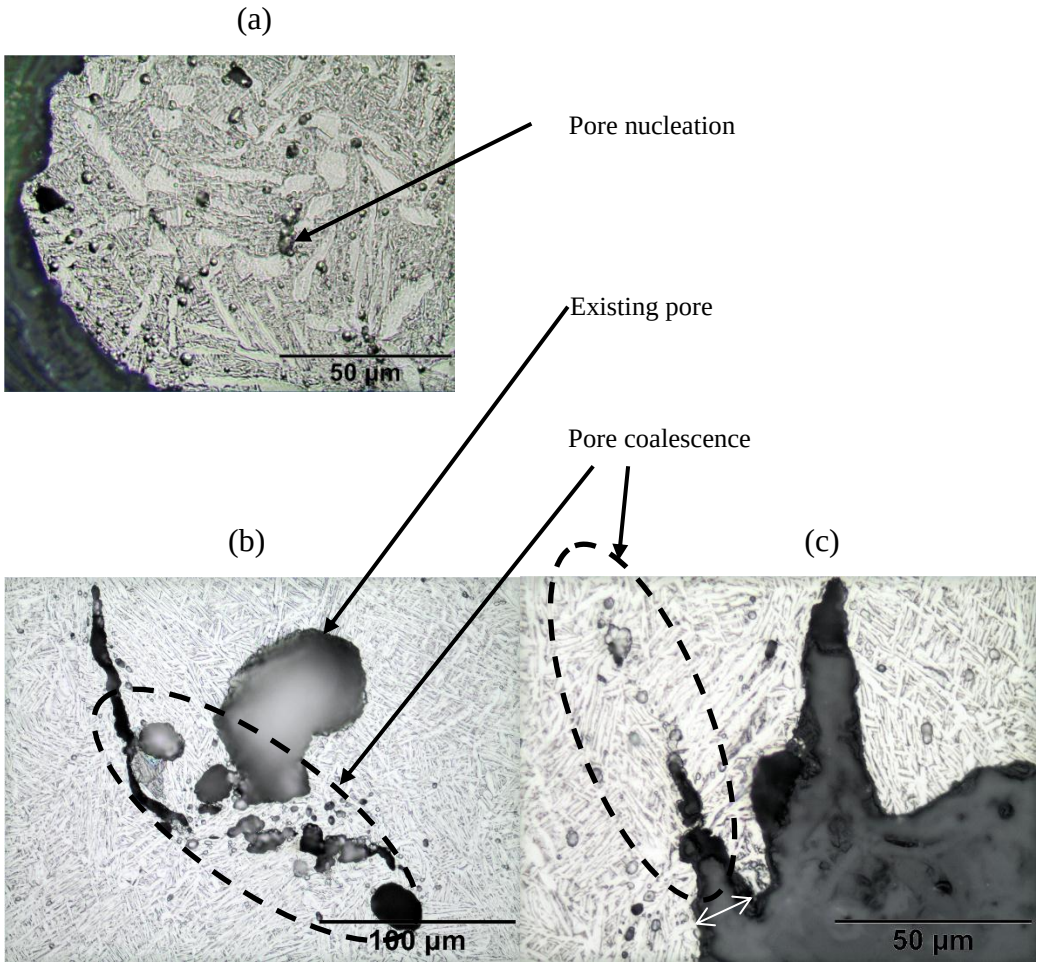

Figure 4.31: Micrographs just below the fracture surface of (a) T2-G3-1, and (b,c) T1-G1-1

5. DISCUSSION

This chapter discusses the results and findings. The significance of each individual result is discussed. The correlations between results of annealing strategies and microstructure as well as correlations between microstructure and tensile behaviour are discussed.

5.1. SAMPLE DENSITY

While sample porosity was not a major focus point of the study; the effect thereof on mechanical properties needed to be measured to distinguish between changes in mechanical properties due to annealing strategies and changes in mechanical properties due to porosity.

Sample density was found to be lower in the second build compared to the first build. Density further decreased drastically in the third build. Due to the drastic increase in porosity between the second and third build, comparing the mechanical properties of the two is problematic. This is because tensile properties are affected by defects and therefore the comparison does not give a true representation of the effect of the annealing strategies on the tensile properties of the samples. The two main causes of defects in samples will now be discussed.

5.1.1. SLM machine error

The machine error caused a slight decrease in sample density from the first to second build of 0.22 %. The decrease in measured density was less drastic than first anticipated. Since each scan vector is re-melted, the defects in a single scan vector are removed during the re-melting. CT scans of the sample from build 2 indicated that the printer error caused defect patterns in the samples. Porosity was most probably caused by air entrapment in missing scan vectors and the subsequent super-heating and expansion process (as discussed in Section 2.12.2). The alignment of pores could be detrimental to fracture toughness and fatigue crack growth due to the increase in coalescence of the pores. The decrease in sample ductility from build 2 is clear as discussed in the results chapter.

5.1.2. Gas flow

A trend in density spread of samples from build 1 was observed. It is argued that this directional trend was caused by the direction of the gas flow. Gas flow (argon) is aimed at removing SLM-produced combustion gasses and splatter away from the build surface. This is to prevent the splatter (large fused particles) from inhibiting homogeneous powder spread and inconsistent powder melting during processing. The gas flow however, did not remove the splatter from the build plate, but only deposited it towards the left, causing the observed porosity pattern. This defect pattern has also been observed by Becker and Dimitrov (2015) of SLM-produced maraging steel 300 manufactured on the same machine.

Pores in the third build appeared to have been caused by a lack of fusion. Lack of fusion resulting from an insufficient laser power. Newly laid powder is thereby not

sufficiently melted to the previous layer. Insufficient power absorption could have been due to a non-homogenous powder layer.

5.2. MARTENSITIC DECOMPOSITION / RECRYSTALLISATION

Martensite decomposition/recrystallisation entails the microstructural transformation of α'/α'' → (α+β). This theoretically improves the ductility of the material and was therefore the aim of the recrystallisation annealing strategy.

The identification of whether α' has decomposed to (α+β) is complicated due to several factors. While the β phase is easy to identify (both through optical and EBSD methods), distinguishing between α and α' with complete certainty is not possible through microstructural analysis alone. This is because both phases have the same crystal structure. Complete certainty of what form the α is in can be attained through, for example, identifying the respective alloy-elemental composition of each phase (as was done by Tan *et al.* (2016)).

Results presented by the author have, however identified strong indicators of full α' decomposition. The influence of recrystallisation annealing strategies on microstructure and tensile behaviour will now be discussed.

Recrystallisation

By studying the micrographs of sample T1-G4-1 (annealed at ~770 °C), Figure 4.9(a), and comparing it to that of T1-G1-1 (annealed at ~870 °C), Figure 4.9(b), two main morphological characteristics stand out. Firstly, the β phase in the former has a precipitate-like appearance. In other words, although β phase has grown along α'/α grains, the lack of significant recrystallisation inhibits the β phase to assume a full lamellar-like structure between α grains, such as is the case in the sample T1-G1-1. The recrystallised structure of (α+β) in T1-G1-1 is much more distinct since it was annealed at 870 °C.

Through careful observation and interpretation of the micrographs it can be argued that while the sample T1-G4-1 showed only partial decomposed to lamellar-like α+β, the sample T1-G1-1 showed complete decomposition to the dual-phase microstructure.

The temperature at which full α' decomposition was measured to take place coincides with literature. The generally excepted martensite start temperature is ~800 ºC, but a much lower temperature of 575 ºC has also been quoted by authors such as Ahmed and Rack (1998). *ThermoCalc* modelling of the difference in Gibbs free energy by Lu *et al.* (2016) of the two phases showed a peak at 800 ºC, Figure 5.1. The difference in Gibbs free energy is the driving force for phase transformation. This indicates that at ~800 ºC the transformation rate will theoretically reach a peak.

Sallica-Leva *et al.* (2016) measured a peak in DSC measurement between 760 and 850 °C when slowly heating a SLM-produced Ti6Al4V sample (see Figure 2.19). This was argued to be due to α' decomposition.

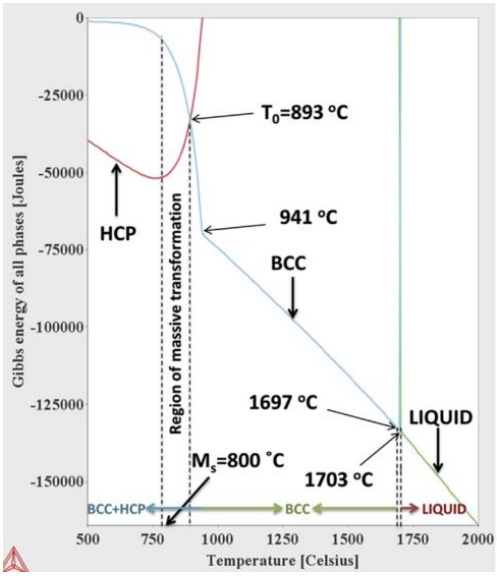

Figure 5.1: Modelling the Gibbs free energy of Ti6Al4V as a function of temperature using Thermo-Calc (TTTI3 database) (Lu *et al.* 2016)

When comparing the grain size of the discussed samples, it can be seen that recrystallisation of the smallest grains (α'/α'') occur first. Higher temperature recrystallisation causes a larger amount of α grains to transform to β. The growth of α phase is thereby possible. Grain growth was measured and found to match that of Xu *et al.* (2015) (see Figure 2.21, page 25).

Globularisation and duplex microstructures

Lamellar grain globularisation increases with an increase in temperature in the range above ~910 ºC. Grain globularisation is dominant at prior-β grain boundaries. This is most likely due to the surface area introduced by the β grain boundaries. The β boundary surface has inherent surface energy and therefore a higher energy state preventing recrystallisation of grains at β boundaries. Furthermore, α grains at β grain boundaries have been found to be much shorter and therefore globularise much quicker than lamellar-like grains.

Fast cooling from above ~900 ºC caused α' to nucleate and grow since the wt % V is too low to successfully stabilise the β phase to prevent it from transforming upon fast to intermediate cooling. This was also found by Pederson (2002).

Tensile behaviour

The interpretation of micro-hardness and Young's modulus results are conflicting. While no change in hardness was measured between the as-built and low annealed sample T2-G2-1 (~600 ºC), a slight increase in median Young's modulus from the as-built sample to the low annealed sample was measured. Therefore, while the micro-hardness measurements do not indicate α' decomposition, the increase in measured stiffness does.

Another indicator of α' decomposition is the clear and sudden drop in UTS from the sample batch T1-G4 (~770 ºC) to sample batches annealed above 800 ºC. The UTS of the samples annealed above 800 ºC does not decrease with temperature. This is a possible indication of a significant change in microstructure at ~800 ºC followed by a less drastic change in microstructure at higher sub-β transus recrystallisation temperatures.

The improved ductility of recrystallised samples is due to the transformation of α'/α'' → (α+β) and grain growth. Simonelli, Tse and Tuck (2014: 6) attribute the increased ductility to the addition of the β phase. This is due to the increase in ease of slip transfer between the α-β phases compared to that of the martensite α'-α' phases. Two primary slip systems of the α phase are aligned with the {110}⟨111⟩ and {112}⟨111⟩ systems of the β phase, with a third set misoriented at a low angle of ~10.51 º and thus, slip transfer across the two phases can occur (Simonelli, Tse and Tuck, 2014).

Although difficult to prove, the cause of the high ductility of the bi-lamellar group (T2-G3) is argued to be due to (a) the isolation of slip lengths to single grains (primary α grains), (b) the increased slip length caused by the enlarged primary α grains formed at the high temperatures of T2-G3 and lastly (c) due to the addition of the ductile β phase.

5.3. MICRO-HARDNESS

The measured Vickers micro-hardness decreases when the as-built sample is annealed in the recrystallisation range and then air cooled. It is argued that the decrease in hardness is because of α and β grain growth and the formation of α'' upon cooling. Pederson (2002) suggests that softer α'' phase forms due to fast cooling from 750 - 900 ºC . This decrease in micro-hardness was measured by Vilaro, Colin and Bartout (2011) (see Figure 2.20(b)). Proof of the formation of α'' would however only be possible though the use of a transmission electron microscope (TEM), and therefore was not be verified.

An increase in hardness when annealing at 510 ºC was measured. This increase is arguably due to the precipitation of Ti_3Al particles in the α phase. The sample annealed at 600 ºC measured the same median hardness as as-built, however the hardness data range of the as-built sample is broader than the stress relieved strategy sample. It is argued that the increase in precision of data was caused by the relief of residual stresses.

5.4. VARIANT SELECTION

Variant selection was measured in the XY-plane of the as-built sample B1-15. Since the SLM thermodynamics of all samples are the same (they were built with the same laser process parameters) and since the variant selection ultimately depends on the thermodynamically-dependant process parameters, the variant selection is assumed to be the same for all the samples.

The number of variants were measured directly and indirectly. Direct measurement was performed through back-calculating the α-variants from the reconstructed β phase. The indirect method identified the frequency of misorientation angles between α grains. A preferred variant selection could be observed in the mismatch between the theoretical frequency of variant-types and the measured frequencies.

For the direct method, variant-type 3 was favoured over variant-type 1. The other three variant-types match that of theoretical amounts (almost exactly). The variant-type frequencies calculated from the indirect methods differ strongly from the theoretical amounts. The cause of the discrepancy between the results of the direct and indirect methods is unclear and further investigation is therefore required.

5.5. PREFERENTIAL ALPHA AND BETA GRAIN ORIENTATION AS A FUNCTION OF BUILD DIRECTION

β texture

Pole figures of the reconstructed β phase of samples indicate that both the build direction and the scan direction influence the β phase texture. Firstly, the build direction caused the β texture to be preferentially orientated with its <001> direction parallel to the build direction (i.e. the Z-axis). This caused the {100} texture observed. The reader is reminded that the planes: (100), (010) and (001) make up the {100} family (the faces of the BCC cube) and therefore any one of these planes will cause the same texture appearance. This texture has also been observed by authors such as Simonelli (2014) and Antonysamy, Meyer and Prangnell (2013). The observed texture is due to β grain growth following the direction of heat flow during crystallization (as discussed in Chapter 2 with reference to Figure 2.23,).

Secondly, pole figures indicate that the BCC crystal lattice aligns itself with the scan direction. This can be seen by the vertices of the cross-shape made by the poles aligning with the direction of the scan vectors (as demonstrated in Figure 4.17, Figure 4.20 and Figure 4.23).

α texture

The texture observed in the pole figures of all the α phase orientation maps match that of texture produced during industrial TMP of Ti6Al4V above the β transus (see Figure 2.30).

Zeng and Bieler (2005) showed that working the material in the β phase field during TMP causes the β phase to assume a {100} texture (viewed from the sample Z-axis) (see Figure 2.29). Since this is the same texture produced during SLM, and since BOR applied to both wrought Ti6Al4V and SLM-produced Ti6Al4V, the two α textures (β-field TMP and SLM-produced) are observed to be identical.

The observed α texture in the pole figures of all samples is now explained. α grain <0 0 0 1> direction was observed to be preferentially orientated at 30 - 45 º to the sample Z-axis. Since the BOR necessitates the HCP (0 0 0 1) plane to be parallel to the BBC {1 0 1} planes, four out of six (0 0 0 1) planes lie at 45 º to the BCC (1 0 0) plane. Therefore, eight out of the 12 α-variants are orientated at ~45 º to the

BCC (1 0 0) plane (two variants per {101} plane). Since the β phase in SLM-produced Ti6Al4V is {1 0 0}-textured, this therefore explains the observed α-texture.

5.6. THE INFLUENCE OF ALPHA-TEXTURE ON YOUNG'S MODULUS

While the theoretical Young's modulus matches that measured of the as-built samples from the first build (114 GPa) the stiffness increases with an increase in annealing temperature.

Lütjering and Williams (2007) showed that applying a load at 45 º to the roll direction of a wrought sample (i.e. 45 º to the C-axis of the HCP crystal) achieved a Young's modulus of 120 GPa. Larson and Zarkades (1974) furthermore showed that the Young's modulus parallel to the C-axis is 145 GPa while perpendicular to the C-axis the modulus decreased to 100 GPa. Therefore, the smaller the angle between the load and the C-axis of the HCP crystal, the higher the stiffness.

Results of tensile load application in the Z-direction of recrystallised samples namely, T1-G4, T1-G3 and T1-G1, measured a stiffness of 120, 122 and 123 GPa respectively. The Z-axis pole figures of these samples showed a preferential ~30 - 45 º angle with respect to the sample's Z-axis.

Since the load direction and stiffness relative to the (0 0 0 1) pole direction agrees with that of literature, the results show that the inherent texture and influence thereof on stiffness of the SLM-produced Ti6Al4V samples, matches that of β-worked Ti6Al4V with load application at ~45 º to the roll direction. Stiffness furthermore increases with an increase in temperature. This is argued to be due to an increase in texture during recrystallisation.

5.7. THE INFLUENCE OF COOLING RATE ON MICROSTRUCTURE

5.7.1. Slow and intermediate cooling

Since a slow cooling rate causes a large grain growth and a lower nucleation rate, the slower the cooling rate, the more the transformation percentage leans towards grain growth as appose to grain nucleation.

A SLM-produced Ti6Al4V sample from CUT was subjected to the same annealing process as T1-G2 (β anneal, furnace cooled), but gave a different microstructural result. The α phase orientation map of the sample depicted in Figure 5.2(a) show a much larger α grain width as compared to the previous discussed maps (Figure 4.24). Residual β is also observed to be much thicker as depicted in Figure 5.2(b). While further analysis of the sample (such as elemental composition) needs to be done to give a factual explanation for the observed microstructure, a theoretical explanation is proposed. If the two samples are identical in elemental composition (most likely) the observed microstructure was caused by a much slower cooling rate after heat treating in the β phase field than those of sample group T1-G2. The reason

why the sample would cool down slower in the same furnace, however is not known, but could have been influenced by its smaller size.

(a) (b)

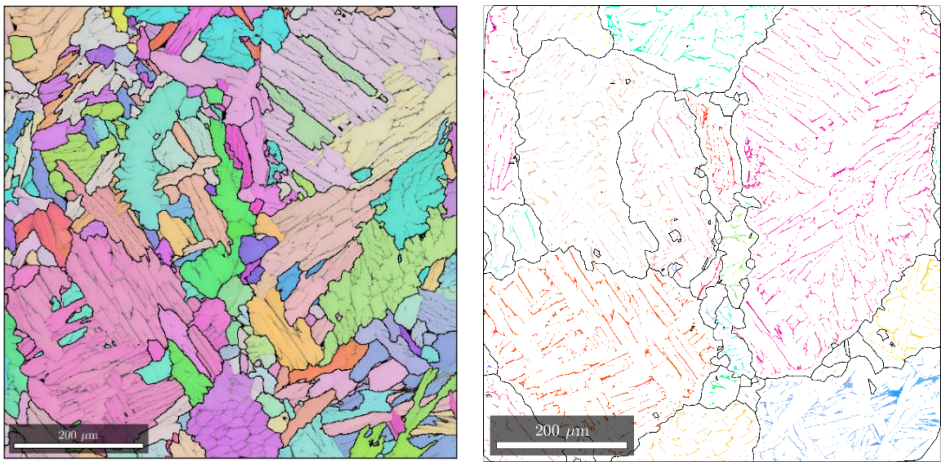

Figure 5.2: IPF orientation map of (a) α phase (b) residual β phase (black lines indicate prior β grain boundaries)

5.7.2. Fast cooling rate

When the sample is cooled too fast, it misses the nose of the diffusional transformation plot on the TTT diagram (see Appendix K.1). α phase therefore transforms to martensitic, as discussed in the literature review chapter, Section 2.5.

The temperature at which martensite forms is quoted by literature at both ~800 ° and 575 ºC. A phenomenological theory is proposed that takes both temperatures into consideration. It is proposed that α' starts at ~800 ºC while α'' starts to form at ~575 ºC. The prior is argued based on results discussed in Chapter 4, and literature results of Kelly (2014), Sallica-Leva *et al.* (2016) and Lu *et al.* (2016). The latter theory (the formation of α'' at ~575 °C) is based on the capability of α'' to form due to induced stress. It could be possible that the stress induced by α' laths during formation cause α'' to form between the α' laths. Since the β phase is argued to form from α'' (Ivasishin and Teliovich, 1999), and the fact that the 600 ºC heat treatment strategy (T2-G2) showed evidence of β-precipitation at the boundaries of α' grains, serves as evidence for the existence of α'' between α' laths and therefore the formation thereof at ~575 ºC.

5.8. THE EFFECT OF STRESS RELIEF ANNEALING ON TENSILE BEHAVIOUR

The samples that were stress relieved at 600 ºC (T2-G2) showed an increase in median stiffness to the theoretical stiffness of α (117 GPa) with negligible influence of the precipitated β particles. Although this would suggest that α'/α'' has decomposed to α, the median micro-hardness does not change from that of the median of the as-built group.

The stress relieved group achieved a high strength due to the small grain size (in agreement with the Hall-Petch relation) and can furthermore be assumed to be free of residual stress. The only fundamental difference between the as-built group and T2-G2 group is (a) an increase in α measured in the stiffness and (b) a relaxation in residual stress. Since the reduction in ductility of the T2-G2 group is unlikely to have been caused by the slight increase in median stiffness α phase, the only explanation for the lower ductility is the relaxation of residual stress during annealing.

Residual stress has been measured to be compressive on the inside SLM-produced samples[1]. Compressive residual stress will theoretically aid in preventing pore nucleation and coalescence. Since this compressive residual stress no longer exists in the stress relieved group, pores nucleate and coalesce at a higher rate causing the lower measured fracture strain.

The recrystallisation strategy allowed for a ductile dual phase (α+β) to form. The increased ductility aids in plastic deformation at pore boundaries. This helps to reduce crack nucleation and crack growth thereby increasing sample elongation to fracture.

5.9. CRYSTAL PLASTIC DEFORMATION

Crystallographic slip was investigated in addition to the transformation kinetics outlined in the project objectives. This investigation was aimed at understanding the slip mechanisms in the annealing strategy that performed the best in terms of fracture elongation (T1-G2). Micrographs of the sample T1-G2-1 near the fracture surfaces (parallel to the fracture surface) was investigated as shown in Figure 5.3.

Slip lines were identified, among others, by the topological steps caused by shadows, as shown in Figure 5.3(b). Grains of the recrystallisation anneal strategy were too small to identify slip systems in their micrographs, since their slip distance is much smaller than the microscopic resolution. The α colony structure observed in the slow cooled sample group, T1-G2, influences the slip kinetics. It is clear from the Figure 5.3(b) that slip lines are confined to α grain colonies.

Evidence of slip was also observed on the surface of the sample, Figure 5.3(a). Colonies were observed to deform both in a bend-like fashion, Figure 5.3(c) and a shear like manner, Figure 5.3(d). This is due to their relative preferential slip direction with respect to the applied load. Further analysis of preferential slip systems could be done through EBSD of samples after they have been plastically deformed.

[1] Ongoing M.Eng work by Lucas Anderson at the University of Stellenbosch

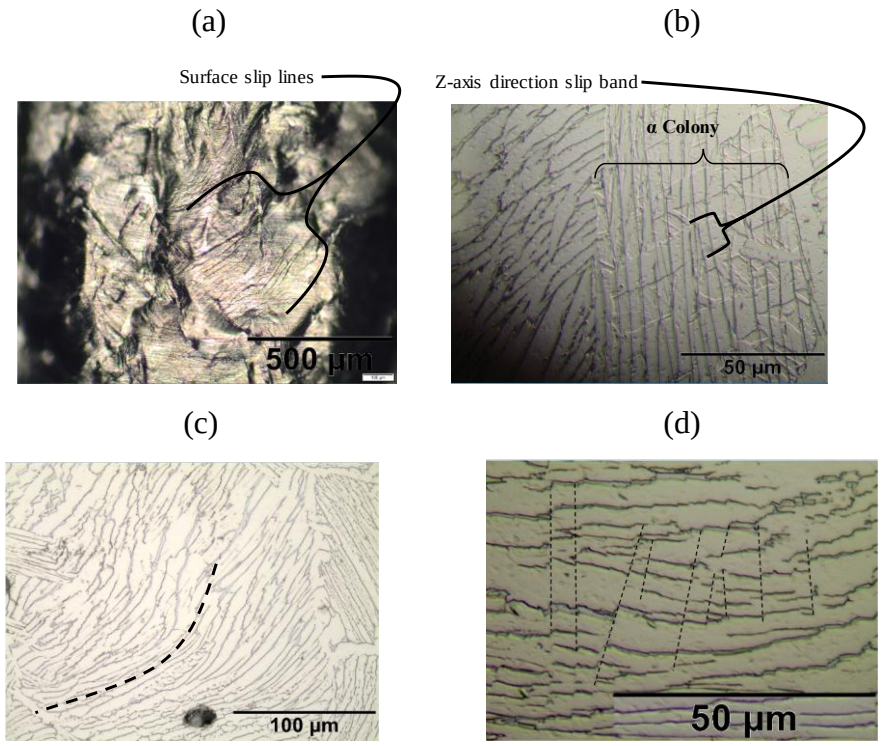

Figure 5.3: Slip lines (a) surface, (b) colony. Deformation mechanisms (c) bending of α colonies (d) in-plane cascade shear steps

6. CONCLUSION

The study aimed at correlating annealing strategies to microstructure and microstructure to tensile behaviour to improve and optimise the tensile properties of SLM-produced Ti6Al4V. Figure 6.1 summarises the core property links the study successfully quantified.

A total of 130 SLM-produced Ti6Al4V samples were manufactured. An in-depth literature review provided the author with a firm understanding of the transformation kinetics of SLM-produced Ti6Al4V. Four different annealing strategies were engineered (a total of 10 annealing groups), based on literature, with the aim of gaining an understanding of the unique microstructural transformation of SLM-produced Ti6Al4V (α'/α''). An in-depth investigation into the microstructure produced by each of the ten annealing strategies was done using both EBSD and optical microscopy. The outcome of the broad set of annealing strategies provided the necessary understanding of how the microstructure behaves when subjected to different heat treatment strategies.

A total of 38 annealed and 8 as-built samples were subjected to uniaxial tensile tests to determine their tensile properties. Correlations between sample tensile properties and annealing strategies were made with the aim of gaining an understanding of how the microstructure, resulting from the annealing strategies, influenced the tensile behaviour. Through correlating the data, as depicted in Figure 6.1, an optimal annealing strategy was determined. The following sections summarise the major findings of the study.

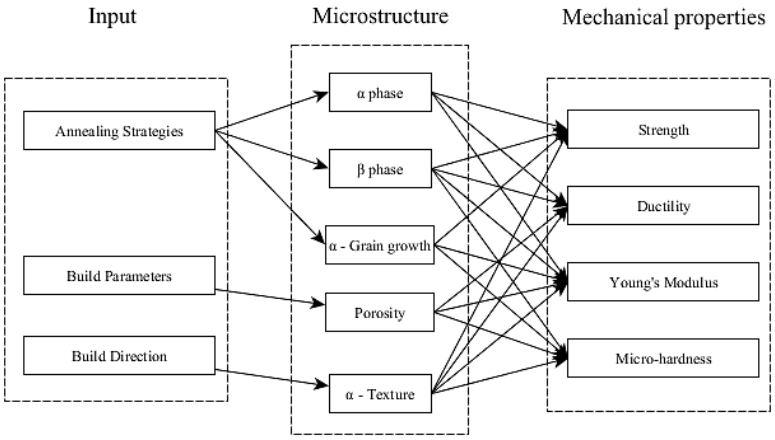

Figure 6.1: The quantified correlations between various SLM-produced Ti6Al4V properties

6.1. PART DENSITY AND MICRO-DEFECTS

A radial decrease in part density within a single build was caused by splatter and combustion gasses being drawn in the direction of the gas-flow exhaust duct and contaminating the build layer surface.

Sample density was also found to decrease from build 1 to build 2 due the observed printer error. Defects in samples were shown to negatively affect tensile properties such as ductility. Low ductility outliers of build 2 and 3 were caused by porosity in these samples.

6.2. INFLUENCE OF ANNEALING STRATEGY ON MICROSTRUCTURE

It was found that upon heating, β-precipitation nucleated at α' grain boundaries and grain triple points at between ~510 - 600 ºC. Annealing below this temperature range caused an increase in hardness due to the formation of Ti_3Al particles.

Upon further heating above 600 ºC, β phase diffused and grew along α' grain triple points and α grain boundaries up until ~ 800 ºC. At ~800 ºC, mass recrystallisation of α'/α'' (starting with the smallest grains) become noticeable in the optical micrographs and UTS results of samples. Further heating above ~800 ºC caused large growth of α grain size and a steep increase in β phase percentage.

The study has shown that globularisation of lamellar-like α grains is possible when annealing at a high enough solid solution temperature. This globularisation annealing strategy eliminates the need for working the material such as is done in industry with wrought Ti6Al4V.

Growth in β phase during bi-lamellar/modal solid-solution annealing caused the vanadium wt % to decrease below ~15 wt % and thereby lowered the stability of the phase. Fast to intermediate cooling from above ~900 ºC (below the β-transus) caused secondary α'/α'' to nucleate and grow from the β phase between primary α grains. This allowed for the construction of bi-lamellar and bi-modal microstructures which has been shown to be possible in SLM-produced Ti6Al4V for the first time. Slow cooling from this temperature range caused α grains to enlarge significantly. Heating above the β-transus temperature of ~970 ºC showed full transformation to β phase microstructure.

6.3. TENSILE TESTS

The martensitic decomposition transformation of α'/α'' → (α+β) was shown to improve ductility due to grain recrystallisation (α'/α''→ α), grain growth of α and the addition of the ductile β phase. Grain growth of α was however shown to be detrimental to material strength, with a decrease of ~20% of the as-build's strength.

Tensile test results showed that this recrystallisation and phase transformation enhances microstructural α texture thereby increasing stiffness. A correlation between stiffness and build direction was identified for the first time. Whereas α texture in wrought Ti-alloys is controlled by TMP strategies, the α texture in SLM-produced Ti6Al4V is determined by build direction.

The tensile behaviour of the bi-lamellar microstructural samples, achieved through a duplex annealing strategy, gave the best combination of strength and ductility.

In-depth understanding of how to tailor SLM-produced Ti6Al4V microstructure through heat treatment strategies as well as a thorough understanding of the correlation between heat treatments, microstructure and tensile behaviour was achieved. The content of this thesis has demonstrated that the objectives of the project were carried out successfully and that the set aim was achieved.

6.4. RECOMMENDATIONS

Recommendations are made for future investigation into aspects of the study that require further research:

- The use of a TEM to identify α'' phase in as-built samples since the phase is too small to observe using conventional optical and XRD methods.
- Using a EBSD and SEM on deformed samples to identify preferential slip systems
- Tailoring process parameters to decrease the thermal gradient during the SLM process in order to aid the decomposition process of α' during building.
- Improving part density by further optimising process parameters.
- The use of more conventional annealing instrumentation for the oxidation-prone Ti6Al4V. Experimental methods using a vacuum furnace is suggested.
- The use of a dilatometer to measure phase transformation and thereby further aid in the phase transformation of SLM-produced Ti6Al4V.

REFERENCES

Ahmed, T. and Rack, H. J. 1998. Phase transformations during cooling in α+β titanium alloys, *Materials Science and Engineering: A*, 243(1–2), pp. 206–211.

Antonysamy, A. A., Meyer, J. and Prangnell, P. B. 2013. Effect of build geometry on the β-grain structure and texture in additive manufacture of Ti6Al4V by selective electron beam melting, *Materials Characterization*, 84, pp. 153–168.

Arcam 2016. *Ti6Al4V ELI Titanium Alloy*. [Online]. Available at: http://www.arcam.com/wp-content/uploads/Arcam-Ti6Al4V-ELI-Titanium-Alloy.pdf [Accessed: 13 August 2016].

ASTM E8/EM-11 2011. *Standard Test Methods for Tension Testing of Metallic Materials*. West Conshohocken, PA: ASTM International.

ASTM F1472-08 2008. ASTM F1472-08: Standard Specification for Wrought Titanium-6Aluminum-4Vanadium Alloy for Surgical Implant Applications, pp. 1–5.

ASTM International 2014. ASTM F2921 - 11 StandardTerminology for Additive Manufacturing — Coordinate Systems and Test, pp. 1–13.

Balasubramanian, S. and Anand, L. 2002. Plasticity of initially textured hexagonal polycrystals at high homologous temperatures: application to titanium, *Acta Materialia*, 50(1), pp. 133–148.

Banerjee, D. and Williams, J. C. 2013. Perspectives on Titanium Science and Technology, *Acta Materialia*, 61(3), pp. 844–879.

Becker, T. H. and Dimitrov, D. 2015. The achievable mechanical properties of SLM produced Maraging Steel 300 components, *Rapid Prototyping Journal*, 22(3), pp. 487–494.

Beladi, H., Chao, Q. and Rohrer, G. S. 2014. Variant selection and intervariant crystallographic planes distribution in martensite in a Ti–6Al–4V alloy, *Acta Materialia*, 80, pp. 478–489.

Bhattacharyya, D., Viswanathan, G. ., Denkenberger, R., Furrer, D. and Fraser, H. L. 2003. The role of crystallographic and geometrical relationships between α and β phases in an α/β titanium alloy, *Acta Materialia*, 51(16), pp. 4679–4691.

Boyer, R., Collings, E. W. and Welsch, G. 1994. *Materials Properties Handbook: Titanium Alloys*. ASM International.

Burgers, W. G. 1934. On the process of transition of the cubic-body-centered modification into the hexagonal-close-packed modification of zirconium, *Physica*, 1(7), pp. 561–586.

Carroll, B. E., Palmer, T. A. and Beese, A. M. 2015. Anisotropic tensile behavior of Ti–6Al–4V components fabricated with directed energy deposition additive manufacturing, *Acta Materialia*, 87, pp. 309–320.

Cayron, C. 2008. Importance of the α→β transformation in the variant selection mechanisms of thermomechanically processed titanium alloys, *Scripta Materialia*, 59(5), pp. 570–573.

Chlebus, E., Kuźnicka, B., Kurzynowski, T. and Dybała, B. 2011. Microstructure and mechanical behaviour of Ti-6Al-7Nb alloy produced by selective laser melting, *Materials Characterization*, 62(5), pp. 488–495.

Chretien, J., King, M., Proia, W. and Rudolf, S. 2010. *Titanium Alpha Case Prevention*. Worcester Polytechnic Institute.

Crespo, A. 2011. Modelling of Heat Transfer and Phase Transformations in the Rapid Manufacturing of Titanium Components, in *Convection and Conduction Heat Transfer*. InTech, pp. 315–340.

Donachie, M. 2000. *Titanium A Technical Guide*. 2nd edn. Ohio: ASM International.

Dye, D. 2015. *Lecture slides of course MSE307 Engineering Alloys 2014-15 L5 : Phase Metallurgy of Titanium Alloys*.

EBSD Explained - From data acquisition to advanced analysis 2015. *Oxford instruments*.

Elmer, J. W., Palmer, T. a., Babu, S. S. and Specht, E. D. 2005. In situ observations of lattice expansion and transformation rates of α and β phases in Ti-6Al-4V, *Materials Science and Engineering A*, 391(1), pp. 104–113.

Elmer, J. W., Palmer, T. a., Babu, S. S., Zhang, W. and DebRoy, T. 2004. Phase transformation dynamics during welding of Ti-6Al-4V, *Journal of Applied Physics*, 95(12), pp. 8327–8339.

Filip, R., Kubiak, K., Ziaja, W. and Sieniawski, J. 2003. The effect of microstructure on the mechanical properties of two-phase titanium alloys, *Journal of Materials Processing Technology*, 133(1), pp. 84–89.

Ford, S. L. N. 2014. Additive Manufacturing Technology: Potential Implications for U.S. Manufacturing Competitiveness, *Journal of International Commerce and Economics*, (9), pp. 1–35.

Gammon, L. M., Briggs, R. D., Packard, J. M., Batson, K. W., Boyer, R. and Domby, C. W. 2004. Metallography and Microstructures of Titanium and its Alloys, *Materials Park, OH: ASM International, 2004.*, 9, pp. 899–917.

Germain, L., Gey, N. and Humbert, M. 2007. Reliability of reconstructed beta-orientation maps in titanium alloys., *Ultramicroscopy*, 107(12), pp. 1129–35.

Gil Mur, F. X., Rodríguez, D. and Planell, J. A. 1996. Influence of tempering temperature and time on the α′-Ti-6Al-4V martensite, *Journal of Alloys and Compounds*, 234(2), pp. 287–289.

Glavicic, M. G., Kobryn, P. A., Bieler, T. R. and Semiatin, S. L. 2003. A method to determine the orientation of the high-temperature beta phase from measured EBSD data for the low-temperature alpha phase in Ti-6Al-4V, *Materials Science and Engineering: A*, 346(1–2), pp. 50–59.

Guo, N. and Leu, M. C. 2013. Additive manufacturing: technology, applications and research needs, *Frontiers of Mechanical Engineering*, 8(3), pp. 215–243.

Hahn, T. 2012. *Investigating the Laser Cusing Process Capabilities with an Emphasis on the Achievable Mechanical Properties*. Stellenbosch University.

Hielscher, R., Bachmann, F., Johnson, O. K. and Mainprice, D. 2016. *MTex Toolbox*. [Online]. Available at: http://mtex-toolbox.github.io./ [Accessed: 11 December 2016].

Huang, Q., Liu, X., Yang, X., Zhang, R., Shen, Z. and Feng, Q. 2015. Specific heat treatment of selective laser melted Ti–6Al–4V for biomedical applications, *Frontiers of Materials Science*, 9(4), pp. 373–381.

Ivasishin, O. M. and Teliovich, R. V 1999. Potential of rapid heat treatment of titanium alloys and steels, *Materials Science and Engineering: A*, 263(2), pp. 142–154.

Karkina, L. E. and Yakovenkova, L. I. 2012. Dislocation core structure and deformation behavior of Ti_3 Al, *Modelling and Simulation in Materials Science and Engineering*. IOP Publishing, 20(6), p. 65003.

Kasperovich, G., Haubrich, J., Gussone, J. and Requena, G. 2016. Correlation between porosity and processing parameters in TiAl6V4 produced by selective laser melting, *Materials and Design*. Elsevier Ltd, 105(May), pp. 160–170.

Kelly, S. M. 2002. *Characterization and Thermal Modeling of Laser Formed Ti-6Al-4V*. Virginia Polytechnic Institute and State University.

Kelly, S. M. 2004. *Thermal and Microstructure Modeling of Metal Deposition Processes with Application to Ti-6Al-4V*. State University.

Khairallah, S. A., Anderson, A. T., Rubenchik, A. and King, W. E. 2016. Laser powder-bed fusion additive manufacturing: Physics of complex melt flow and formation mechanisms of pores, spatter, and denudation zones, *Acta Materialia*, 108, pp. 36–45.

Kim, H. Y., Ikehara, Y., Kim, J. I., Hosoda, H. and Miyazaki, S. 2006. Martensitic transformation, shape memory effect and superelasticity of Ti–Nb binary alloys, *Acta Materialia*, 54(9), pp. 2419–2429.

Knowles, C. R., Becker, T. H. and Tait, R. B. 2012. The effect of heat treatment on the residual stress levels within direct metal laser sintered Ti-6Al-4V as measured using the hole-drilling strain gauge method, in *RAPDASA*. Sun City, pp. 119–129.

Kruth, J., Badrossamay, M., Yasa, E., Deckers, J., Thijs, L. and Van Humbeeck, J. 2010. Part and material properties in selective laser melting of metals, *Proceedings of the SFF Symposium*.

Larson, E. and Zarkades, A. 1974. *Battelle Columbus Laboratories Report, MCIC-74*.

Lee, Y. T. and Welsch, G. 1990. Young's modulus and damping of Ti-6Al-4V alloy as a function of heat treatment and oxygen concentration, *Materials Science and Engineering: A*. Elsevier, 128(1), pp. 77–89.

Li, Z., Li, J., Zhu, Y., Tian, X. and Wang, H. 2016. Variant selection in laser melting deposited α + β titanium alloy, *Journal of Alloys and Compounds*, 661, pp. 126–135.

Lu, S. L., Qian, M., Tang, H. P., Yan, M., Wang, J. and StJohn, D. H. 2016. Massive transformation in Ti-6Al-4V additively manufactured by selective electron beam melting, *Acta Materialia*, 104, pp. 303–311.

Lütjering, G. and Williams, J. C. 2007. *Titanium*. Berlin: Springer.

Makiewicz, K. T. 2013. *Development of Simultaneous Transfromation Kinetics Microstructure Model with Application to Laser Metal Deposited Ti-6Al-4V and Alloy 718*. Ohio State University.

Morgan, R., Sutcliffe, C. J. and O'Neill, W. 2004. Density analysis of direct metal laser re-melted 316L stainless steel cubic primitives, *Journal of Materials Science*, 39(4), pp. 1195–1205.

Motyka, M., Kubiak, K., Sieniawski, J. and Waldemar Ziaja 2012. Chapter 5 - Hot Plasticity of Alpha Beta Alloys, in Amin, A. K. M. N. (ed.) *Titanium Alloys – Towards Achieving Enhanced Properties for Diversified Applications*. InTech, pp. 87–118.

Murgau, C. C., Pederson, R. and Lindgren, L. E. 2012. A model for Ti–6Al–4V microstructure evolution for arbitrary temperature changes, *Modelling and Simulation in Materials Science and Engineering*, 20(5), pp. 1–23.

Murphy, D. B., Salmon, E. D., Spring, K. R., Parry-Hill, M., Sutter, R. T. and Davidson, ichael W. 2012. *Wavefront Shear in Wollaston and Nomarski Prisms*. [Online]. Available at: http://www.olympusmicro.com/primer/java/dic/wollastonwavefronts/index.html [Accessed: 27 September 2016].

Murr, L. E., Esquivel, E. V., Quinones, S. A., Gaytan, S. M., Lopez, M. I., Martinez, E. Y., Medina, F., Hernandez, D. H., Martinez, E., Martinez, J. L., Stafford, S. W., Brown, D. K., Hoppe, T., Meyers, W., Lindhe, U. and Wicker, R. B. 2009. Microstructures and mechanical properties of electron beam-rapid manufactured Ti-6Al-4V biomedical prototypes compared to wrought Ti-6Al-4V, *Materials Characterization*, 60(2), pp. 96–105.

Murr, L. E., Quinones, S. a., Gaytan, S. M., Lopez, M. I., Rodela, A., Martinez, E. Y., Hernandez, D. H., Martinez, E. Y., Medina, F. and Wicker, R. B. 2009. Microstructure and mechanical behavior of Ti-6Al-4V produced by rapid-layer manufacturing, for biomedical applications., *Journal of the mechanical behavior of biomedical materials*. Elsevier Ltd, 2(1), pp. 20–32.

Nanite 2014. *Thermocouple circuit Ktype including voltmeter temperature.svg*. [Online]. Available at: https://commons.wikimedia.org/wiki/File:Thermocouple_circuit_Ktype_including_voltmeter_temperature.svg.

Osakada, K. and Shiomi, M. 2006. Flexible manufacturing of metallic products by selective laser melting of powder, *International Journal of Machine Tools and Manufacture*, 46(11), pp. 1188–1193.

Pederson, R. 2002. *Microstructure and Phase Transformation of Ti-6Al-4V*. Luleå University of Technology.

Qiu, C., Adkins, N. J. E. and Attallah, M. M. 2013. Microstructure and tensile properties of selectively laser-melted and of HIPed laser-melted Ti-6Al-4V, *Materials Science and Engineering A*. Elsevier, 578, pp. 230–239.

Qiu, D., Shi, R., Zhang, D., Lu, W. and Wang, Y. 2015. Variant selection by dislocations during α precipitation in α/β titanium alloys, *Acta Materialia*, 88, pp. 218–231.

Rafi, H. K., Karthik, N. V., Gong, H., Starr, T. L. and Stucker, B. E. 2013. Microstructures and Mechanical Properties of Ti6Al4V Parts Fabricated by Selective Laser Melting and Electron Beam Melting, *Journal of Materials Engineering and Performance*, 22(12), pp. 3872–3883.

Ready, J. F. 1971. *Effects of High-Power Laser Radiation*. London: Academic Press.

Roberts, I. a., Wang, C. J., Esterlein, R., Stanford, M. and Mynors, D. J. 2009. A three-dimensional finite element analysis of the temperature field during laser melting of metal powders in additive layer manufacturing, *International Journal of Machine Tools and Manufacture*. Elsevier, 49(12–13), pp. 916–923.

Rombouts, M. 2006. *Selective laser sintering/melting of iron-based powders*. Katholieke Universiteit Leuven.

Royal Academy of Engineering 2013. *Additive manufacturing: opportunities and constraints: A summary of a roundtable forum held on 23 May 2013 hosted by the Royal Academy of Engineering*.

Sallica-Leva, E., Caram, R., Jardini, A. L. and Fogagnolo, J. B. 2016. Ductility improvement due to martensite a' decomposition in porous Ti-6Al-4V parts produced by selective laser melting for orthopedic implants, *Journal of the Mechanical Behavior of Biomedical Materials*. Elsevier, 54, pp. 149–158.

Sefer, B. 2014. *Oxidation and Alpha–Case Phenomena in Titanium Alloys used in Aerospace Industry: Ti–6Al–2Sn–4Zr–2Mo and Ti–6Al–4V*. Luleå University of Technology.

Semiatin, S. L., Kinsel, K. T., Pilchak, a. L. and Sargent, G. a. 2013. Effect of process variables on transformation-texture development in Ti-6Al-4V sheet following beta heat treatment, *Metallurgical and Materials Transactions A: Physical Metallurgy and Materials Science*, 44(8), pp. 3852–3865.

Seshacharyulu, T., Medeiros, S. C., Morgan, J. T., Malas, J. C., Frazier, W. G. and Prasad, Y. V. R. K. 2000. Hot deformation and microstructural damage mechanisms in extra-low interstitial (ELI) grade Ti-6Al-4V, *Materials Science and Engineering A*, 279(1–2), pp. 289–299.

Shi, R. and Wang, Y. 2013. Variant selection during α precipitation in Ti–6Al–4V under the influence of local stress – A simulation study, *Acta Materialia*, 61(16), pp. 6006–6024.

Simchi, A. and Pohl, H. 2003. Effects of laser sintering processing parameters on the microstructure and densification of iron powder, *Materials Science and Engineering: A*, 359(1–2), pp. 119–128.

Simonelli, M. 2014. *Microstructure and mechanical properties of Selective Laser Melted*. Loughborough University.

Simonelli, M., Tse, Y. and Tuck, C. 2012. Further understanding of ti-6al-4v selective laser melting using texture analysis, in *Solid Freeform Fabrication Symposium*, pp. 480–491.

Simonelli, M., Tse, Y. Y. and Tuck, C. 2014. Effect of the build orientation on the mechanical properties and fracture modes of SLM Ti–6Al–4V, *Materials Science and Engineering: A*. Elsevier, 616, pp. 1–11.

Stráský, J. 2014. *Lecture slides of Josef Stráský.` Department of Physics of Materials. Charles University in Prague*. [Online]. Available at: http://material.karlov.mff.cuni.cz/people/strasky/Titanium_course/ [Accessed: 30 May 2016].

Tan, X., Kok, Y., Toh, W. Q., Tan, Y. J., Descoins, M., Mangelinck, D., Tor, S. B., Leong, K. F. and Chua, C. K. 2016. Revealing martensitic transformation and α/β interface evolution in electron beam melting three-dimensional-printed Ti-6Al-4V, *Scientific Reports*. Nature Publishing Group, 6(1), p. 26039.

Thejane, K., Chikosha, S. and du Preez, W. B. 2016. Characterisation of Ti6Al4V (ELI) Powder Used by the South African Collaborative Program in Additive Manufacturing, in *17th RAPDASA*.

Thijs, L. 2014. *Microstructure and texture of metal parts produced by Selective Laser Melting*. Katholieke Universiteit Leuven.

Tromans, D. 2011. Elastic Anistropy Of HCP Metal Crystals And Polycrystals, *IJRRAS*, 6(4).

Vilaro, T., Colin, C. and Bartout, J. D. 2011. As-fabricated and heat-treated microstructures of the Ti-6Al-4V alloy processed by selective laser melting, *Metallurgical and Materials Transactions A: Physical Metallurgy and Materials Science*, 42(10), pp. 3190–3199.

Vrancken, B., Thijs, L., Kruth, J.-P. and Van Humbeeck, J. 2012. Heat treatment of Ti6Al4V produced by Selective Laser Melting: Microstructure and mechanical properties, *Journal of Alloys and Compounds*, 541(0), pp. 177–185.

Wang, S. C., Aindow, M. and Starink, M. J. 2003. Effect of self-accommodation on α/α boundary populations in pure titanium, *Acta Materialia*, 51(9), pp. 2485–2503.

Wang, S. C., Starink, M. J., Ubhi, H. S. and Li, W. S. 2012. Identification of transformed grain boundaries and reconstruction of the prior grains from EBSD data in pure Ti and α-Ti alloys, *Reviews on Advanced Materials Science*, 32(1), pp. 47–51.

Wauthle, R., Vrancken, B., Beynaerts, B., Jorissen, K., Schrooten, J., Kruth, J.-P. and Van Humbeeck, J. 2015. Effects of build orientation and heat treatment on the microstructure and mechanical properties of selective laser melted Ti6Al4V lattice structures, *Additive Manufacturing*, 5, pp. 77–84.

Waziers, S., Roy, S., Suwas, S., Tamirisakandala, S., Srinivasan, R. and Miracle,

D. 2009. Solidification Microstructure and Texture in Grain-Refined Titanium Alloys, *Microstructure and Texture in Steels*, pp. 475–482.

Weaver, M. 2011. *Lecture slides of Mark Weaver Course: MTE 583 - Advanced Structure of Metals. University of Alabama*. The University of Alabama: Department of Metallurgical and Materials Engineering. [Online]. Available at: http://bama.ua.edu/~mweaver/courses/MTE583/ [Accessed: 12 October 2016].

Welsch, G., Boyer, R. and Collings, E. W. 1993. *Materials Properties Handbook: Titanium Alloys*.

Xu, W., Brandt, M., Sun, S., Elambasseril, J., Liu, Q., Latham, K., Xia, K. and Qian, M. 2015. Additive manufacturing of strong and ductile Ti–6Al–4V by selective laser melting via in situ martensite decomposition, *Acta Materialia*, 85, pp. 74–84.

Xu, W., Sun, S., Elambasseril, J., Liu, Q., Brandt, M. and Qian, M. 2015. Ti-6Al-4V Additively Manufactured by Selective Laser Melting with Superior Mechanical Properties, *The Journal of The Minerals, Metals & Materials Society*, 67(3), pp. 1–6.

Xue, W., Krishna, B. V., Bandyopadhyay, A. and Bose, S. 2007. Processing and biocompatibility evaluation of laser processed porous titanium, 3, pp. 1007–1018.

Yan, M. and Yu, P. 2015. An Overview of Densification, Microstructure and Mechanical Property of Additively Manufactured Ti-6Al-4V — Comparison among Selective Laser Melting, Electron Beam Melting, Laser Metal Deposition and Selective Laser Sintering, and with Conventional Powder, in *Sintering Techniques of Materials*. INTECH, pp. 76–106.

Yang, J., Han, J., Yu, H., Yin, J., Gao, M., Wang, Z. and Zeng, X. 2016. Role of molten pool mode on formability, microstructure and mechanical properties of selective laser melted Ti-6Al-4V alloy, *Materials and Design*, 110, pp. 558–570.

Zeng, L. and Bieler, T. R. 2005. Effects of working, heat treatment, and aging on microstructural evolution and crystallographic texture of α, α', α'' and β phases in Ti-6Al-4V wire, *Materials Science and Engineering A*, 392(1–2), pp. 403–414.

APPENDIX A: POWDER ANALYSIS

A.1. CHEMICAL COMPOSTION

Table A.1: Chemical composition of new powder from three different canisters (Thejane, Chikosha and du Preez, 2016)

Specification	**Chemical composition (weight %)**					
	Al	**V**	**Fe**	**N**	**O**	**Ti**
ASTM F3001 Ti6Al4V (ELI)	5.5-6.5	3.5-4.5	0.25	0.05	0.13	89
TLS Technik GmbH	6.34	3.94	0.25	0.006	0.082	89
Canister 1	6.04	3.83	0.16	0.010	0.079	90
Canister 2	6.07	3.81	0.16	0.078	0.078	90
Canister 3	6.06	3.84	0.16	0.05	0.078	90

Table A.2: Chemical composition of powder after three cycle uses (Thejane, Chikosha and du Preez, 2016)

Specification	**Chemical composition (weight %)**					
	Al	V	Fe	N	O	Ti
Requirements of ASTM F3001 Ti6Al4V (ELI)	5.5-6.5	3.5-4.5	0.25	0.05	0.13	89
Cycle 1	6.07	3.88	0.17	0.049	0.082	90
Cycle 2	6.21	3.89	0.18	0.010	0.092	90
Cycle 3	5.96	3.84	0.17	0.011	0.096	90

A.2. X-RAY MICRO COMPUTED TOMOGRAPHY SCANS

Table A.3: Results of CT scans of SU powder

	Scan 1	Scan 2	Scan 3
Number of particles in scan volume	267574	263420	262459
Mean particle volume (mm^3)	0.0000204	0.0000190	0.0000196
Average particle diameter (mm)	0.03390 (34 microns)	0.03310 (33 microns)	0.03345 (33 microns)
Number of internal closed pores	472	357	308
Average % internal closed porosity	0.01 %	0.01 %	0.00 %
Average pore diameter	0.0131	0.0122	0.0125
Largest pore diameter (mm)	0.0329	0.0280	0.0270

A.3. POWDER PARTICLE SIZE DISTRIBUTION

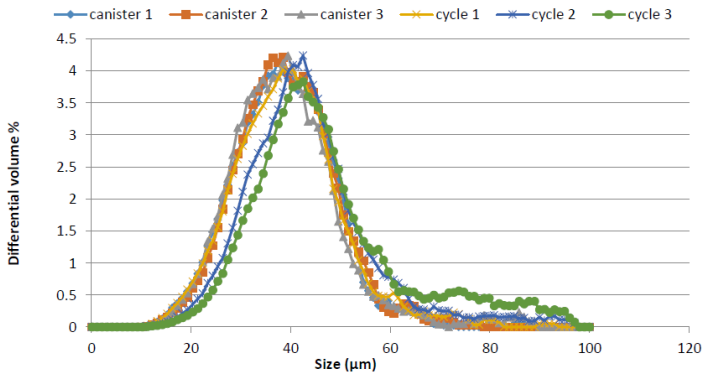

Figure A.1: Particle size distribution, adapted from Thejane, Chikosha and Du. Preez (2016)

APPENDIX B: FURNACE CALIBRATION

B.1. FURNACE TEMPERATURE MEASUREMENTS

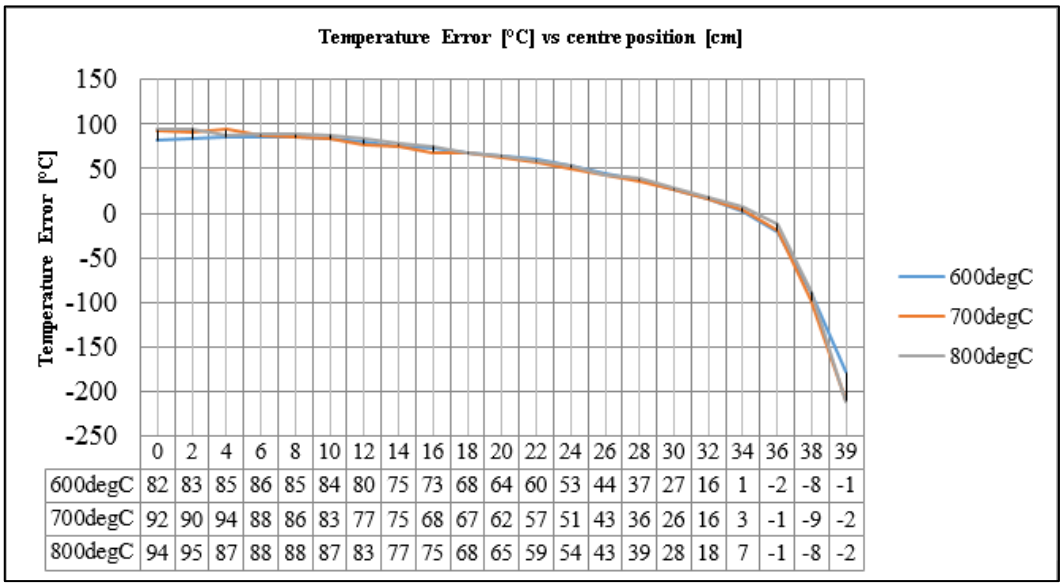

	0	2	4	6	8	10	12	14	16	18	20	22	24	26	28	30	32	34	36	38	39
600degC	82	83	85	86	85	84	80	75	73	68	64	60	53	44	37	27	16	1	-2	-8	-1
700degC	92	90	94	88	86	83	77	75	68	67	62	57	51	43	36	26	16	3	-1	-9	-2
800degC	94	95	87	88	88	87	83	77	75	68	65	59	54	43	39	28	18	7	-1	-8	-2

Figure B.1: Furnace temperature measurements

B.2. OXYGEN CONTAMINATION MICROGRAPHS

(a) (b)

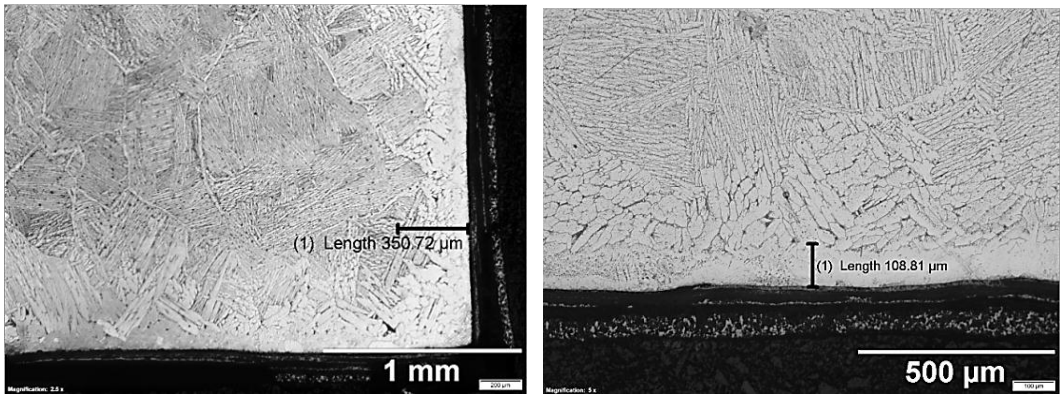

(c)

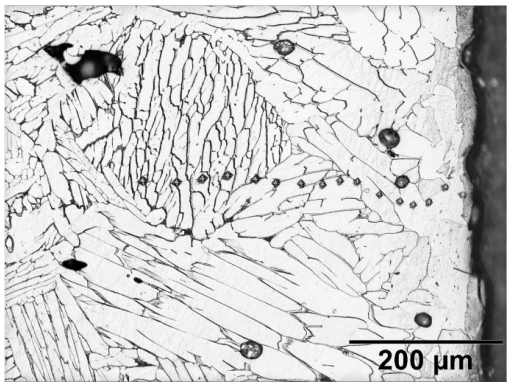

Figure B.2: Oxygen contamination (a) total noticeable influence (b) α case (c) micro indentation marks

(a) (b)

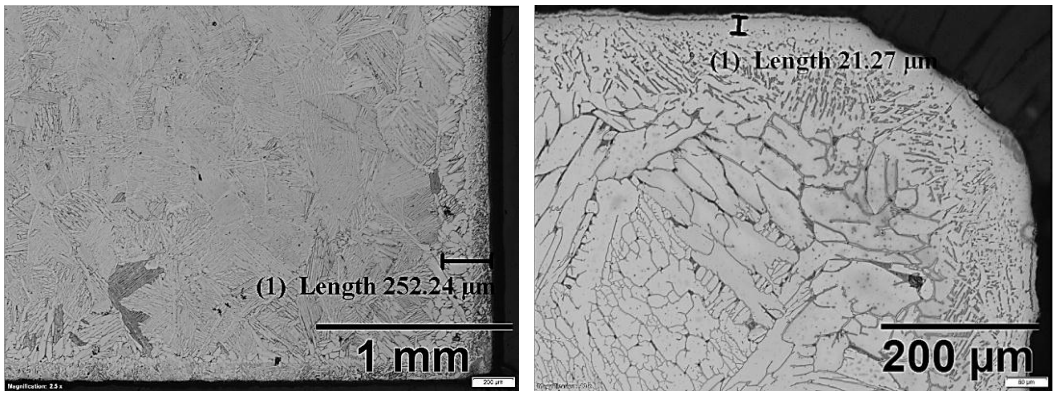

Figure B.3: Oxygen contamination (a) total noticeable influence (b) α case

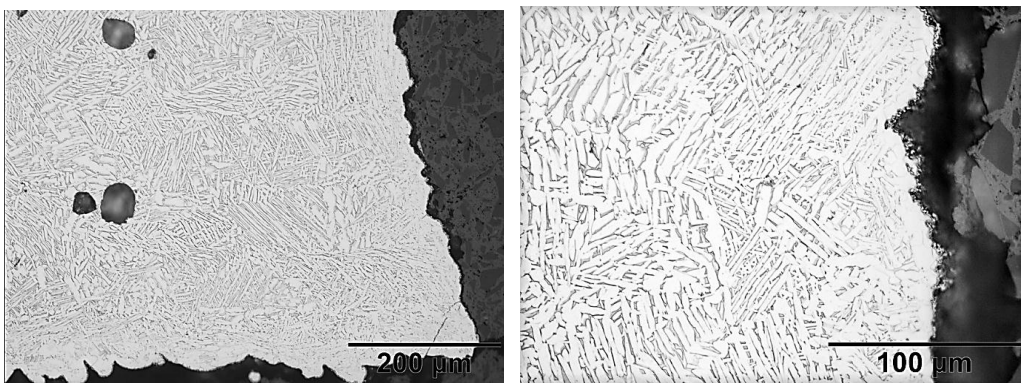

Figure B.4: Oxygen contamination (a) no noticeable influence (b) slight noticeable influence on β-phase presence

APPENDIX C: TECHNICAL DRAWING OF TENSILE SAMPLE

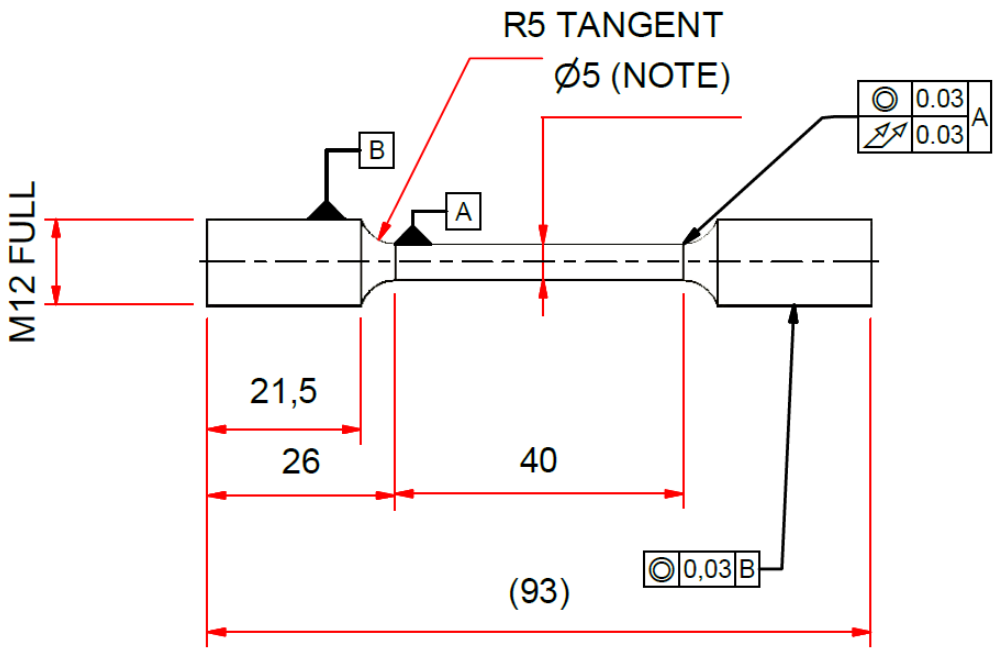

APPENDIX D: DECLARATION OF CONFORMITY DOCUMENTS

D.1. SCALE

KERN & Sohn GmbH
Ziegelei 1
72336 Balingen-Frommern
Germany

www.kern-sohn.com
+0049-[0]7433-9933-0
+0049-[0]7433-9933-149
info@kern-sohn.com

EU-Konformitätserklärung | EU Declaration of Conformity

DE Wir erklären hiermit unter alleiniger Verantwortung, dass das Produkt, auf das sich diese Erklärung bezieht, mit den nachstehenden Richtlinien übereinstimmt. Für die Waage liegt eine Bauartzulassung vor. Das Jahr der EU-Konformitätsbewertung ist neben der CE Konformitätskennzeichnung aufgeführt. Solche Waagen sind ab Werk EU-konformitätsbewertet und tragen die Kennzeichnung „M" auf dem Gerät selbst und auf der Verpackung. Die angegebene Gravitationszone legt den Verwendungsort fest.

EN We hereby declare and assume sole responsibility for the declaration that the product complies with the directives hereinafter. The scale was issued with a type approval certificate. The year of EU conformity assessment can be found next to the CE mark. Such scales bear the mark "M", on the device itself as well as on the packaging. The gravity zone specified determines the place of use.

Typ | Type	Seriennr. | Serial no.
ABT-NM	**xxxxxxxxxx**

CE Kennzeichnung Mark applied	EU-Richtlinie EU directive	Normen Standards	Bauartzulassungen Type approvals
CE	2011/65/EU *(RoHS)*	EN 50581:2012	
CE	2014/30/EU *(EMC)*	EN 61326-2-2:2013	
CE M16 0122[1)]	2014/31/EU *(NAWI)*		T8728
CE	2014/35/EU *(LVD)*	EN 61010-1:2010	

[1)] Die benannte Stelle NMi Certin BV (0122) führt Audits für Modul D gemäß NAWI-Richtlinie durch und stellte das Zertifikat CE-240 für KERN aus.
[1)] The notified body NMi Certin BV (0122) performed Module D audit for NAWI directive and issued the certificate CE-240 for KERN.

g =

Ort oder Zone: internal adjustment
Location or zone:

Datum | Date: 02.06.2016

Ort der Ausstellung: 72336 Balingen, Germany
Place of issue:

	John Doe *KERN & Sohn GmbH*	Albert Sauter *KERN & Sohn GmbH*
Signatur: Signature:	Prüfbevollmächtigter Verification officer	Geschäftsführer Managing director

D.2. M2 LASERCUSING MACHINE

EC conformity declaration according to directive 2006/42/EC, Annex II A

The manufacturer: *Concept Laser GmbH*
An der Zeil 8
96215 Lichtenfels

declares herewith, that the following product

Product description: M2 cusing
Type: M2-20XX-XX-XX

conforms to the requirements of directive 2006/42/EC.

The following standards were also applied:

EMC Directive 2004/108/EC
EC Low Voltage Directive 2006/95/EC
ATEX directive 94/9/EC

Contact person for technical documents: Frank Schödel, *Concept Laser GmbH*

The following harmonised standards were applied:

EN ISO 12100-1:2003	Safety of machinery - Basic concepts, general principles for design – Part 1: Basic terminology, methodology (ISO 12100-1:2003)
EN ISO 12100-2:2003	Safety of machinery - Basic concepts, general principles for design – Part 2: Technical principles (ISO 12100-2:2003)
EN 60204-1:2006	Safety of machinery - Electrical equipment of machines – Part 1: General requirements (IEC 60204-1:2005, modified)
EN 60947-1:2007	Low-voltage switchgear and controlgear - Part 1: General rules (IEC 60947-1:2007)
EN 61131-2:2007	Programmable controllers - Part 2: Equipment requirements and tests (IEC 61131-2:2007)
EN 61204-3:2000	Low-voltage power supplies DC output - Part 3: Electromagnetic compatibility (EMC) (IEC 61204-3:2000)
EN 61310-3:2008	Safety of machinery - Indication, marking and actuation – Part 3: Requirements for the location and operation of actuators (IEC 61310-3:2007)

location: Lichtenfels
date: 02.03.2010

Frank Herzog (managing director)

APPENDIX E: M2 LASERCUSING MACHINE SPECIFICATIONS

4.1.1 Technical data for the *M2 Cusing* laser machine

Weight of *M2 cusing* machine	approx. 2000 kg
Dimensions of *M2 cusing* machine (W x D x H)	2440 mm x 1630 mm x 2354 mm
Dimensions of construction chamber (X x Y x Z)	250 mm x 250 mm x 280 mm
Production speed	2 cm^3/h to 20 cm^3/h (material-dependent)
Maximum scanning speed	7m/s
Laser beam diameter	70 µm to 200 µm
LaserCUSING layer thicknesses	20 µm – 50 µm
Connected loads:	Power consumption 7.4 kW Power connection 3/N/PE AC 400 V, 32 A
Network connection	Ethernet 100 MB/s; machine connection: RJ45 jack
Laser system	Fibre laser 200 F
	Laser protection class 4
	Power max. 200 W (cw mode); wavelength 1075 nm (infrared) (in line with EN 60825 - 1/94)
Control cabinet protection class	IP54
Compressed air	6 – 10 bar
Inert gas (protective gas)	Two gas connections for nitrogen (5.0) or (and) argon (4.6), 5 bar; optional: external N_2 generator
Inert gas consumption	approx. 2.5 m^3/h
Storage and transportation temperature	-20 – +35 °C
Function at ambient temperature	+15 – +35 °C
Maximum temperature change	2 °C / h
Relative atmospheric humidity	Max. 80 % (non-condensing) (use exclusively indoors)
Height above sea level	Max. 2000 m
Safety of the control system	In line with EN 954-1
CE marking	CE
Sound pressure level (at 1 m distance)	< 70 dB (A)

See the operating manuals from the manufacturers for details about the technical data for the components used.

APPENDIX F: ARCHIMEDES METHOD POROSITY MEASUREMENTS

Table F.1: Build 1 porosity percentage (samples 1-50)

Porosity [%]	sample #								
0.78	**41**	0.77	**31**	0.63	**21**	0.80	**11**	0.32	**1**
0.78	**42**	0.79	**32**	0.79	**22**	0.55	**12**	0.37	**2**
0.70	**43**	0.96	**33**	0.64	**23**	0.77	**13**	0.54	**3**
1.00	**44**	1.01	**34**	1.08	**24**	0.71	**14**	0.67	**4**
1.19	**45**	0.76	**35**	0.88	**25**	0.79	**15**	0.39	**5**
1.22	**46**	1.06	**36**	1.08	**26**	0.55	**16**	0.23	**6**
1.20	**47**	0.97	**37**	0.80	**27**	0.85	**17**	0.21	**7**
1.00	**48**	0.97	**38**	1.04	**28**	0.70	**18**	0.94	**8**
0.72	**49**	1.01	**39**	0.74	**29**	0.34	**19**	0.30	**9**
0.85	**50**	0.76	**40**	0.41	**30**	0.78	**20**	0.15	**10**

Table F.2: Porosity of samples from build 2

Sample #	Porosity [%]
20	0.93
32	0.75
43	0.69
9	1.07
10	1.02
38	1.06
49	1.29

Table F.3: Porosity of horizontal samples from build 3

Sample #	Porosity [%]
5	1.76
4	2.05
7	2.42
1	1.61
6	2.03
3	1.72

APPENDIX G: APPARATUS ACQUISITION SETTINGS

G.1. X-RAY MICRO COMPUTED TOMOGRAPHY

Table G.1: CT scanning apparatus specifications

Instrument	*General Electric Nanotom S.*
X-ray filament	240 kV/320 W
Capable voxel resolution	1.5 µm.
Reconstruction software	*Datos*
Data analysis software	*Volume Graphics VGStudioMax 3.0*

G.2. SEM - JEOL JSM-7001F

Table G.2: SEM acquisition setting

Accelerating Voltage	15.00 kV
Specimen Tilt	70.05 º
Hit Rate	99.60 %
Speed of Acquisition	40.52 Hz
Step size	0.5 µm
Magnification	300x
Scan size	0.7 mm

APPENDIX H: PHYSICAL PROPERTIES OF TI6AL4V

Table H.1: Physical properties of Ti6Al4V (a) (Elmer *et al.* 2004: 8333), (b) (Yan and Yu, 2015)

(a)

Physical property	Value
Liquidus temperature, T_L (K)	1928
Solidus temperature, T_S (K)	1878
Density of liquid metal, ρ (kg/m^3)	3.89×10^3
Effective viscosity of liquid, μ (kg/m-s)	0.049
Thermal conductivity of liquid, k_L (W/m-K)	32.5
Thermal conductivity of solid, k_S (W/m-K)	8.3 to 24.2
Specific heat of solid, C_{PS} (J/kg-K)	725
Specific heat of liquid, C_{PL} (J/kg-K)	872
Temperature coefficient of surface tension, $d\gamma/dT$ (N/m-K)	-2.8×10^{-4}
Coefficient of thermal expansion (K^{-1})	1.1×10^{-5}
Convective heat transfer coefficient top surface (W/m^2-K)	1.59×10^3

(b)

Physical property	**Value**
Density of solid (ρ)	4.43 g/cm^3
Density of liquid (ρ)	3.89 g/cm^3
Solidus temperature	1877 K (1604°C)
Liqudus temperature	1933 K (1660°C)
Temperature of $(\alpha+\beta) \rightarrow \beta$	1253K (980°C)
Temperature of $\alpha \rightarrow \beta$	~1023K (750°C)
Thermal conductivity of solid (k_s)	6.7 W/m/K
Thermal conductivity of liquid (k_l)	32.5 W/m/K
Specific heat capacity of solid (Cp_s)	0.526 J/g/K
Specific heat capacity of liquid (Cp_l)	0.872 J/g/K
Coefficient of thermal expansion of solid (K^{-1})	8.6 µm/m/K
Temperature of martensite phase transformation (M_s)	~1053K (780°C) or ~883K(610°C)

APPENDIX I: CRYSTALOGRAPHY AND METALLOGRAPHY

I.1. ETCHANTS

Name	Typical composition	Notes
Kroll's reagent	1.5 mL HF 4 mL HNO_3 94 mL H_2O	. . .
Oxalic reagent (tint etch)	20 mL HF 20 g oxalic 98 mL H_2O	15 s for Ti-6Al-4V. Do not remove etch products.
Ammonium bifluoride (ABF)	1 g ammonium bifluoride (NH_4FHF) 99 mL H_2O	Do not remove etch products.
Lactic hydride reagent	Mix fresh 5 mL lactic acid and 5 mL stock solution (3 mL HF, 97 mL HNO_3)	Commercially pure titanium hydrides

Figure I.1: Common etchants for titanium metallography (Gammon *et al.* 2004: 902)

I.2. DIFFERENCIAL IMAGING CONTRAST

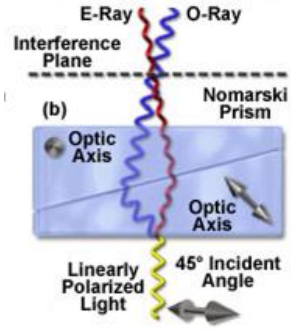

Figure I.2: Schematic of a Nomarski Prism (Murphy *et al.* 2012)

I.3. ORIENTATION MATRICES OF SYMMETRY ELEMENTS

Table 1
Rotational symmetry elements of the cubic system

$$\mathbf{E}^{\beta} = \begin{bmatrix} 1 & 0 & 0 \\ 0 & 1 & 0 \\ 0 & 0 & 1 \end{bmatrix} \quad \mathbf{C}^{\beta}_{2x} = \begin{bmatrix} 1 & 0 & 0 \\ 0 & -1 & 0 \\ 0 & 0 & -1 \end{bmatrix} \quad \mathbf{C}^{\beta}_{2y} = \begin{bmatrix} -1 & 0 & 0 \\ 0 & 1 & 0 \\ 0 & 0 & 1 \end{bmatrix} \quad \mathbf{C}^{\beta}_{2z} = \begin{bmatrix} -1 & 0 & 0 \\ 0 & -1 & 0 \\ 0 & 0 & 1 \end{bmatrix}$$

$$\mathbf{C}^{\beta}_{31+} = \begin{bmatrix} 0 & 0 & 1 \\ 1 & 0 & 0 \\ 0 & 1 & 0 \end{bmatrix} \quad \mathbf{C}^{\beta}_{32+} = \begin{bmatrix} 0 & 0 & -1 \\ 1 & 0 & 0 \\ 0 & -1 & 0 \end{bmatrix} \quad \mathbf{C}^{\beta}_{33+} = \begin{bmatrix} 0 & 0 & -1 \\ -1 & 0 & 0 \\ 0 & 1 & 0 \end{bmatrix} \quad \mathbf{C}^{\beta}_{34+} = \begin{bmatrix} 0 & 0 & 1 \\ -1 & 0 & 0 \\ 0 & -1 & 0 \end{bmatrix}$$

$$\mathbf{C}^{\beta}_{31-} = \begin{bmatrix} 0 & 1 & 0 \\ 0 & 0 & 1 \\ 1 & 0 & 0 \end{bmatrix} \quad \mathbf{C}^{\beta}_{32-} = \begin{bmatrix} 0 & 1 & 0 \\ 0 & 0 & -1 \\ -1 & 0 & 0 \end{bmatrix} \quad \mathbf{C}^{\beta}_{33-} = \begin{bmatrix} 0 & -1 & 0 \\ 0 & 0 & 1 \\ -1 & 0 & 0 \end{bmatrix} \quad \mathbf{C}^{\beta}_{34-} = \begin{bmatrix} 0 & -1 & 0 \\ 0 & 0 & -1 \\ 1 & 0 & 0 \end{bmatrix}$$

$$\mathbf{C}^{\beta}_{4x+} = \begin{bmatrix} 1 & 0 & 0 \\ 0 & 0 & -1 \\ 0 & 1 & 0 \end{bmatrix} \quad \mathbf{C}^{\beta}_{4y+} = \begin{bmatrix} 0 & 0 & 1 \\ 0 & 1 & 0 \\ -1 & 0 & 0 \end{bmatrix} \quad \mathbf{C}^{\beta}_{4z+} = \begin{bmatrix} 0 & -1 & 0 \\ 1 & 0 & 0 \\ 0 & 0 & 1 \end{bmatrix} \quad \mathbf{C}^{\beta}_{4x-} = \begin{bmatrix} 1 & 0 & 0 \\ 0 & 0 & 1 \\ 0 & -1 & 0 \end{bmatrix}$$

$$\mathbf{C}^{\beta}_{4y-} = \begin{bmatrix} 0 & 0 & -1 \\ 0 & 1 & 0 \\ 1 & 0 & 0 \end{bmatrix} \quad \mathbf{C}^{\beta}_{4z-} = \begin{bmatrix} 0 & 1 & 0 \\ -1 & 0 & 0 \\ 0 & 0 & 1 \end{bmatrix} \quad \mathbf{C}^{\beta}_{2a} = \begin{bmatrix} 0 & 1 & 0 \\ 1 & 0 & 0 \\ 0 & 0 & -1 \end{bmatrix} \quad \mathbf{C}^{\beta}_{2b} = \begin{bmatrix} 0 & -1 & 0 \\ -1 & 0 & 0 \\ 0 & 0 & -1 \end{bmatrix}$$

$$\mathbf{C}^{\beta}_{2c} = \begin{bmatrix} 0 & 0 & 1 \\ 0 & -1 & 0 \\ 1 & 0 & 0 \end{bmatrix} \quad \mathbf{C}^{\beta}_{2d} = \begin{bmatrix} -1 & 0 & 0 \\ 0 & 0 & 1 \\ 0 & 1 & 0 \end{bmatrix} \quad \mathbf{C}^{\beta}_{2e} = \begin{bmatrix} 0 & 0 & -1 \\ 0 & -1 & 0 \\ -1 & 0 & 0 \end{bmatrix} \quad \mathbf{C}^{\beta}_{2f} = \begin{bmatrix} -1 & 0 & 0 \\ 0 & 0 & -1 \\ 0 & -1 & 0 \end{bmatrix}$$

Table 2
Rotational symmetry elements of the hexagonal system

$$\mathbf{E}^{\alpha} equals; \begin{bmatrix} 1 & 0 & 0 \\ 0 & 1 & 0 \\ 0 & 0 & 1 \end{bmatrix} \quad \mathbf{C}^{\alpha}_{6z+} = \begin{bmatrix} 1/2 & -\sqrt{3}/2 & 0 \\ \sqrt{3}/2 & 1/2 & 0 \\ 0 & 0 & 1 \end{bmatrix} \quad \mathbf{C}^{\alpha}_{3z+} = \begin{bmatrix} -1/2 & -\sqrt{3}/2 & 0 \\ \sqrt{3}/2 & -1/2 & 0 \\ 0 & 0 & 1 \end{bmatrix}$$

$$\mathbf{C}^{\alpha}_{2z} = \begin{bmatrix} -1 & 0 & 0 \\ 0 & -1 & 0 \\ 0 & 0 & 1 \end{bmatrix} \quad \mathbf{C}^{\alpha}_{6z-} = \begin{bmatrix} 1/2 & \sqrt{3}/2 & 0 \\ -\sqrt{3}/2 & 1/2 & 0 \\ 0 & 0 & 1 \end{bmatrix} \quad \mathbf{C}^{\alpha}_{3z-} = \begin{bmatrix} -1/2 & \sqrt{3}/2 & 0 \\ -\sqrt{3}/2 & -1/2 & 0 \\ 0 & 0 & 1 \end{bmatrix}$$

$$\mathbf{C}^{\alpha}_{21+} = \begin{bmatrix} 1 & 0 & 0 \\ 0 & -1 & 0 \\ 0 & 0 & -1 \end{bmatrix} \quad \mathbf{C}^{\alpha}_{22+} = \begin{bmatrix} -1/2 & \sqrt{3}/2 & 0 \\ \sqrt{3}/2 & 1/2 & 0 \\ 0 & 0 & -1 \end{bmatrix} \quad \mathbf{C}^{\alpha}_{23+} = \begin{bmatrix} 1/2 & \sqrt{3}/2 & 0 \\ \sqrt{3}/2 & -1/2 & 0 \\ 0 & 0 & -1 \end{bmatrix}$$

$$\mathbf{C}^{\alpha}_{21-} = \begin{bmatrix} -1 & 0 & 0 \\ 0 & 1 & 0 \\ 0 & 0 & -1 \end{bmatrix} \quad \mathbf{C}^{\alpha}_{22-} = \begin{bmatrix} 1/2 & -\sqrt{3}/2 & 0 \\ -\sqrt{3}/2 & -1/2 & 0 \\ 0 & 0 & -1 \end{bmatrix} \quad \mathbf{C}^{\alpha}_{23-} = \begin{bmatrix} -1/2 & -\sqrt{3}/2 & 0 \\ -\sqrt{3}/2 & 1/2 & 0 \\ 0 & 0 & -1 \end{bmatrix}$$

(Glavicic *et al.*, 2003)

I.4. α VARIANTS

Table I.1: Table of α variants from Beladi *et al*. (2014: 484), data from Wang *et al*. (2003)

Variant	Plane parallel	Direction parallel	Rotation angle/axis from V1
V1	$(1\,\bar{1}\,0)_\beta \parallel (0\,0\,0\,1)_\alpha$	$[1\,1\,1]_\beta \parallel [1\,1\,\bar{2}\,0]_\alpha$	–
V2	$(1\,0\,\bar{1})_\beta \parallel (0\,0\,0\,1)_\alpha$	$[1\,1\,1]_\beta \parallel [1\,1\,\bar{2}\,0]_\alpha$	60°/[1 1 $\bar{2}$ 0]
V3	$(0\,1\,\bar{1})_\beta \parallel (0\,0\,0\,1)_\alpha$	$[1\,1\,1]_\beta \parallel [1\,1\,\bar{2}\,0]_\alpha$	60°/[1 1 $\bar{2}$ 0]
V4	$(1\,1\,0)_\beta \parallel (0\,0\,0\,1)_\alpha$	$[\bar{1}\,1\,1]_\beta \parallel [1\,1\,\bar{2}\,0]_\alpha$	90°/[1 $\overline{2.38}$ 1.38 0]
V5	$(1\,0\,1)_\beta \parallel (0\,0\,0\,1)_\alpha$	$[\bar{1}\,1\,1]_\beta \parallel [1\,1\,\bar{2}\,0]_\alpha$	63.26°/[$\overline{10}$ 5 5 $\bar{3}$]
V6	$(0\,1\,\bar{1})_\beta \parallel (0\,0\,0\,1)_\alpha$	$[\bar{1}\,1\,1]_\beta \parallel [1\,1\,\bar{2}\,0]_\alpha$	60.83°/[$\overline{1.377}$ $\bar{1}$ 2.377 0.359]
V7	$(1\,1\,0)_\beta \parallel (0\,0\,0\,1)_\alpha$	$[1\,\bar{1}\,1]_\beta \parallel [1\,1\,\bar{2}\,0]_\alpha$	90°/[1 $\overline{2.38}$ 1.38 0]
V8	$(1\,0\,\bar{1})_\beta \parallel (0\,0\,0\,1)_\alpha$	$[1\,\bar{1}\,1]_\beta \parallel [1\,1\,\bar{2}\,0]_\alpha$	60.83°/[$\overline{1.377}$ $\bar{1}$ 2.377 0.359]
V9	$(0\,1\,1)_\beta \parallel (0\,0\,0\,1)_\alpha$	$[1\,\bar{1}\,1]_\beta \parallel [1\,1\,\bar{2}\,0]_\alpha$	63.26°/[$\overline{10}$ 5 5 $\bar{3}$]
V10	$(1\,\bar{1}\,0)_\beta \parallel (0\,0\,0\,1)_\alpha$	$[1\,1\,\bar{1}]_\beta \parallel [1\,1\,\bar{2}\,0]_\alpha$	10.53°/[0001]
V11	$(1\,0\,1)_\beta \parallel (0\,0\,0\,1)_\alpha$	$[1\,1\,\bar{1}]_\beta \parallel [1\,1\,\bar{2}\,0]_\alpha$	60.83°/[$\overline{1.377}$ $\bar{1}$ 2.377 0.359]
V12	$(0\,1\,1)_\beta \parallel (0\,0\,0\,1)_\alpha$	$[1\,1\,\bar{1}]_\beta \parallel [1\,1\,\bar{2}\,0]_\alpha$	60.83°/[$\overline{1.377}$ $\bar{1}$ 2.377 0.359]

Table I.2: Variant types and their properties

Type	Reduced axis/angle pairs between crystals of this type	Deviation of integer axes ('tolerance')	Percentage out of 132 possible HAGBs [%]	Likely transformation slip systems
0	Identity	-	-	$(\bar{1}101)_\alpha[\bar{1}2\bar{1}\bar{3}]_\alpha$ $/(0\bar{1}1)_\beta[\bar{1}11]_\beta$
I	$[0\,0\,0\,1]/10.53º$	0º	9.1	$(1101)_\alpha[11\bar{2}0]_\alpha$ $/(\bar{1}\bar{1}2)_\beta[111]_\beta$
II	$[11\bar{2}0]/60º$	0º	18.2	$(\bar{1}10\bar{1})_\alpha[\bar{1}2\bar{1}3]_\alpha$ $/(\bar{1}01)_\beta[1\bar{1}1]_\beta$
III	$[-1.377, -1, 2.377, 0.35$ $/60.83º$	0.48º	36.4	$(0001)_\alpha[11\bar{2}0]_\alpha$ $/(0\bar{1}0)_\beta[111]_\beta$
IV	$[\overline{10}\,5\,5\,\bar{3}]/63.26º$	0º	18.2	$(\bar{1}101)_\alpha[11\bar{2}0]_\alpha$ $/(0\bar{1}1)_\beta[111]_\beta$
V	$[1, -2.38, 1.38, 0]/90º$	0.02º	18.2	$(\bar{1}10\bar{1})_\alpha[11\bar{2}0]_\alpha$ $/(\bar{1}01)_\beta[111]_\beta$

Table I.3: Variants (1-12) orientation matrices with variant-type in brackets. Adapted from Simonelli (2014) and Beladi, Chao and Rohrer (2014)

1. $\boldsymbol{D^{-1}C^{\beta}_{4Y-}}$ (~)	7. $\boldsymbol{D^{-1}C^{\beta}_{33-}}$ (Type 5)
2. $\boldsymbol{D^{-1}C^{\beta}_{32+}}$ (Type2)	8. $\boldsymbol{D^{-1}C^{\beta}_{2d}}$ (Type 3)
3. $\boldsymbol{D^{-1}C^{\beta}_{2e}}$ (Type 2)	9. $\boldsymbol{D^{-1}}$E (Type 4)
4. $\boldsymbol{D^{-1}C^{\beta}_{33+}}$ (Type 5)	10. $\boldsymbol{D^{-1}C^{\beta}_{2a}}$ (Type 1)
5. $\boldsymbol{D^{-1}C^{\beta}_{31-}}$ (Type 4)	11. $\boldsymbol{D^{-1}C^{\beta}_{2b}}$ (Type 3)
6. $\boldsymbol{D^{-1}C^{\beta}_{4X-}}$ (Type 3)	12. $\boldsymbol{D^{-1}C^{\beta}_{2X}}$ (Type 3)

I.5. HCP ANISOTROPY FACTORS AND COMLIANCES

Metal	f_E	f_G	Metal	f_E	f_G
Be	1.202	1.107	Nd	1.277	0.997
Mg	1.117	0.988	Gd	1.126	0.995
Sc	1.179	0.965	Tb	1.105	0.992
Ti	1.406	1.165	Dy	1.107	1.001
Co	1.402	1.022	Ho	1.087	1.009
Zn	0.293	0.796	Er	1.068	1.002
Y	1.072	0.999	Tm	0.955	0.978
Zr	1.273	0.977	Lu	0.966	0.995
Ru	1.148	0.983	Hf	1.166	1.034
Cd	0.361	0.765	Re	1.241	0.969
La	1.151	0.907	Os	1.125	1.004
Pr	1.377	1.015	Tl	3.286	1.851

Figure I.3: (a) Anisotropy factors for a range of HCP metals (Tromans, 2011: 476)

$$\begin{bmatrix}\varepsilon_1\\ \varepsilon_2\\ \varepsilon_3\\ \gamma_4\\ \gamma_5\\ \gamma_6\end{bmatrix} = \begin{bmatrix} S_{11} & S_{12} & S_{13} & \bullet & \bullet & \bullet \\ S_{12} & S_{11} & S_{13} & \bullet & \bullet & \bullet \\ S_{13} & S_{13} & S_{33} & \bullet & \bullet & \bullet \\ \bullet & \bullet & \bullet & S_{44} & \bullet & \bullet \\ \bullet & \bullet & \bullet & \bullet & S_{44} & \bullet \\ \bullet & \bullet & \bullet & \bullet & \bullet & S_{66} \end{bmatrix} \begin{bmatrix}\sigma_1\\ \sigma_2\\ \sigma_3\\ \sigma_4\\ \sigma_5\\ \sigma_6\end{bmatrix}$$

$$S_{66} = 2(S_{11} - S_{12})$$

where compliance values in TPa^{-1} equal:

$$S_{11} = 9.26$$
$$S_{12} = -4.67$$
$$S_{13} = -1.81$$
$$S_{33} = 6.84$$
$$S_{44} = 21.5$$
$$S_{66} = 2(s_{11} - s_{12})$$

Figure I.4: Hooks law of HCP crystal where subscripts 1, 2, 3 represent direction <2 -1 -1 0>, (1 1 0) and (0 0 0 1) respectively.

APPENDIX J: ADDITIVE MANUFACTURING

State of starting material	Process	Material preparation	Layer creation technique	Phase change	Typical materials	Applications
Liquid	SLA	Liquid resin in a vat	Laser scanning/ light projection	Photopoly-merization	UV curable resin, ceramic suspension	Prototypes, casting patterns, soft tooling
	MJM	Liquid polymer in jet	Ink-jet printing	Cooling & photopoly-merization	UV curable acrylic plastic, wax	Prototypes, casting patterns
	RFP	Liquid droplet in nozzle	On-demand droplet deposition	Solidification by freezing	Water	Prototypes, casting patterns
Filament/ Paste	FDM	Filament melted in nozzle	Continuous extrusion and deposition	Solidification by cooling	Thermoplastics, waxes	Prototypes, casting patterns
	Robocasting	Paste in nozzle	Continuous extrusion	–	Ceramic paste	Functional parts
	FEF	Paste in nozzle	Continuous extrusion	Solidification by freezing	Ceramic paste	Functional parts
Powder	SLS	Powder in bed	Laser scanning	Partial melting	Thermoplastics, waxes, metal powder, ceramic powder	Prototypes, casting patterns, metal and ceramic preforms (to be sintered and infiltrated)
	SLM	Powder in bed	Laser scanning	Full melting	Metal	Tooling, functional parts
	EBM	Powder in bed	Electron beam scanning	Full melting	Metal	Tooling, functional parts
	LMD	Powder injection through nozzle	On-demand powder injection and melted by laser	Full melting	Metal	Tooling, metal part repair, functional parts
	3DP	Powder in bed	Drop-on-demand binder printing	–	Polymer, Metal, ceramic, other powders	Prototypes, casting shells, tooling
Solid sheet	LOM	Laser cutting	Feeding and binding of sheets with adhesives	–	Paper, plastic, metal	Prototypes, casting models

Figure J.1: Working principles of AM processes (Guo and Leu, 2013)

Table J.1: MAM processes and the main companies in industry (Guo and Leu, 2013)

MAM Process	Companies	Materials used
SLM	EOS, SLM solutions, Concept Laser, Trumpf, MCP-HEK Tooling	Stainless steel: GP1, PH1 and 17-4, cobalt chrome MP1, Titanium: Ti6Al4V, Ti6Al4V ELI and TiCP, IN718, Maraging steel MS1, AlSi20Mg
EBM	Arcam	Steel H13, 17-4 PH, PH 13-8 Mo, 304, 316 and 420, aluminium 4047, titanium TiCP, Ti-6-4, Ti-6-2-4-2 and Ti6-2-4-6, IN625, IN617, Cu-Ni alloy, cobalt satellite 21
LDM/LENS	Optomec	Ti6Al4V, Ti6Al4V ELI, cobalt chrome

J.1. SLM PROCESS LITERATURE MATRIX

Machine	Estimated Porosity (vol. %)	E[J/mm^3] P[W], V[mm/s], h[mm], t[mm]	Beam diameter (d) [mm]	Scan strategy	0.2 % proof stress (yield stress) (MPa)	UTS (MPa)	Elongation (%)	Young's Modulus (MPa)	Reference
EOS M270 DMLS	0	42, 120, 960, 0.1, 0.03	0.1		1098 (15)	1237 (13)	8.8 (0.6)	109 (2.1)	(Gong et al. 2015)
Concept Laser M2	0.19	44.4, 100, 1000, 0.075, 0.03	0.15	90deg stacking, 5mm islands	-	-	-	-	(van Rooyen 2013)
Concept Laser M2	1	52, 100, 600, 0.105, 0.03	0.15	90deg stacking, 5mm islands	1108 (19)	1215 (20)	8.13 (1.02)	107.2 (2.8)	(van Rooyen 2013)
Concept Laser M2	<0.1	66.67-125, 150-200, 800-1500, 0.075, 0.02	0.15	90deg stacking, 5mm islands	>1000	~1200	7 to 10	-	(Qiu et al. 2013)
EOS M280 DMLS (CUT Bloem)	0.05	41.3-67.4, **170, 1200**-1400, 0.07-0.098, 0.03	0.1	67deg stacking, 5mm islands	-	-	-	-	(du Plessis et al, 2016)
EOS M270 DMLS	1	74, 120, 540, 0.1, 0.03	0.1	-	1150 (91)	1257 (74)	8.0 (2.0)	111 (1.4)	(Gong et al. 2015)
In-house LM-Q SLM machine	-	87, 250, 1600, 0.06, 0.03	~	-	1110 (9)	1267 (5)	7.28 (1.12)	109.2 (3.1)	(Vrancken et al. 2012)
EOS M270 DMLS	1	32, 120, 1260, 0.1, 0.03	0.1	-	932 (16)	1112 (13)	6.6 (1.4)	95 (3.0)	(Gong et al. 2015)
EOS M270 DMLS	5	100, 120, 400, 0.1, 0.03	0.1	-	1066 (91)	1148 (80)	5.4 (3.8)	109 (3.7)	(Gong et al. 2015)
EOS M270 DMLS	5	27, 120, 1500, 0.1, 0.03	0.1	-	813 (23)	978 (32)	3.7 (0.6)	83 (3.0)	(Gong et al. 2015)

J.2. MAM PROCESS DESCRIPTIONS

Indirect MAM methods (partial melting or sintering)

The first type of indirect process entails sintering the metal powder. Selective Laser Sintering (SLS) selectively sinters powder layers that are evenly spread onto the powder bed. The process is essentially identical to SLM, as depicted in Figure 2.32.

Achievable density is below 99 % and similar to that achievable through PM (Yan & Yu, 2015). A post process step such as liquid metal infiltration or HIP is used to densify and/or improve material properties.

The second type of indirect method entails adding a binder material, such as a low-melting metal, polymer, or mixture of the two, to the metal powder to 'glue' powder particles together. Upon laser irradiation, the polymer melts and binds the metallic powder particles. This method can produce high precision parts. A popular company that specialises in this type of MAM is *Höganäs AB*.

Post processing either entails the removal of the binder thereafter sintering the powder or using a non-melting technique in which the binder (made of small metal particles in a liquid of photo-curable resin) is cured using UV light. A tertiary HIP process and/or liquid-metal infiltration can follow to densify and improve mechanical properties.

Full melt / direct methods

Direct methods, as the name implies, does not require a multi-step fabrication process. Direct methods of MAM include SLM, Electron Beam Melting (EBM) and Laser Melting Deposition, (LMD) (Figure J.1) or LENS (laser engineered net shaping). Direct methods use a high-power laser or electron beam technology to fully melt metal powder to achieve high density (up to 99 %) metal parts. Lengthy post processing needed in the indirect methods to increase part density is avoided through direct methods.

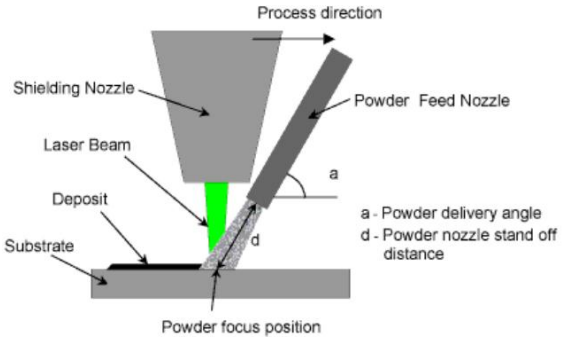

Figure J.1: Schematic of the working principles of LMD and LENS systems (Yan and Yu, 2015)

In-depth research into the kinetics of laser-powder interaction and subsequent localised melting (and evaporating) into liquid pool and solidification thereof has been done by Rombouts (2006) and Thijs (2014).

The MAM techniques of SLM and SLS follow the same process route, the only difference being that SLS process uses a low-power laser to partially melt (sinter) particle surfaces together instead of full melting such as is the case with SLM. A detailed schematic of the SLM / SLS process is depicted in Figure 2.32. Current leading suppliers of SLM printing machines are *EOS* and *Concept Laser*. Leading suppliers of EBM machines are *Arcon*. Each type of MAM process and their main manufacturers is included in 0.

The ASTM committee on AM suggested a reference coordinate system for SLM parts. A schematic of this coordinate system is depicted in Figure 2.31.

Laser characteristics

The laser used in SLM machines has a Gaussian energy distribution through the cross-section of the beam. Most SLM machines use a transverse electromagnetic (TEM) mode of '00'. The laser has a symmetrical energy distribution radially about the centre of the beam Figure J.2.

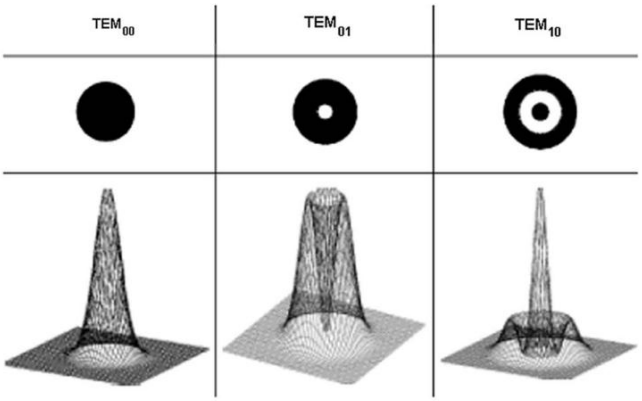

Figure J.2: Various Gaussian energy profile in laser cross-section (Ready 1971: 433)

The centre of the beam has the maximum irradiance intensity (power per area) of I_0. The laser irradiance of this profile is defined as:

$$I(r) = I_0 e^{2d^2/d_1^2} \tag{17}$$

Where d_1 is the beam diameter at which the irradiance diminishes to $1/e^2$ and d is the distance from the centre of the beam. Similarly, the heat flux of the laser follows from (17) as:

$$q(r) = \frac{2P}{\pi r_0^2} e^{2r^2/r_0^2} \tag{18}$$

Where P is the laser power and r_0 the spot size and r the radial distance. The heat flux input to the powder layer is dependence on the material's laser energy absorbance, α. This parameter is dependent on a number of factors including: nature

of the surface, level of oxidation, wavelength of the laser, surface temperature etc. (Roberts *et al.* 2009). The heat flux input to a layer is therefore expressed as:

$$\bar{q} = \alpha \cdot q(r) \tag{19}$$

Three main laser regimes may be distinguished: continuous mode, pulsed mode and pulsed mode with the recoil effect. The most common mode used is the continuous mode.

Focal offset distance

Focal offset distance is a laser process parameter rarely changed from its default of zero. The influence of focal offset distance on microstructure was investigated by Xu *et al.* (2015) and found to be beneficial in decreasing the thermal gradient during melting and thereby improve the decomposition of martensite during building.

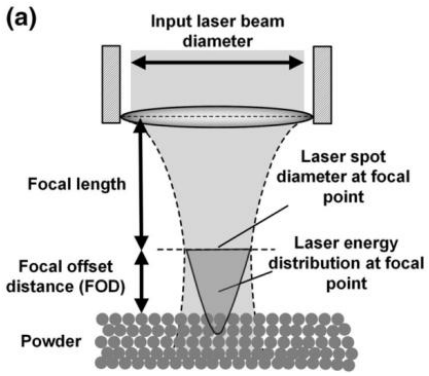

Figure J.3: Laser attributes (W Xu *et al.* 2015)

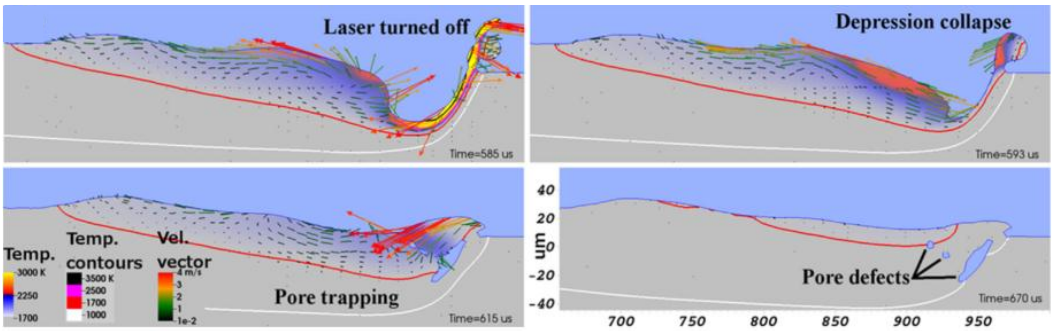

Figure J.4: Modelling of pore entrapment due to melt pool collapse at the end of scan vector (Khairallah et al., 2016)

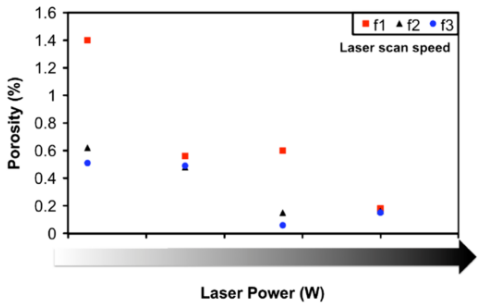

Figure J.5: Dependency of porosity on laser power and scan speed (Qiu, Adkins and Attallah, 2013) where scan speeds compare according to f1<f2<f3

(a) (b) (c)

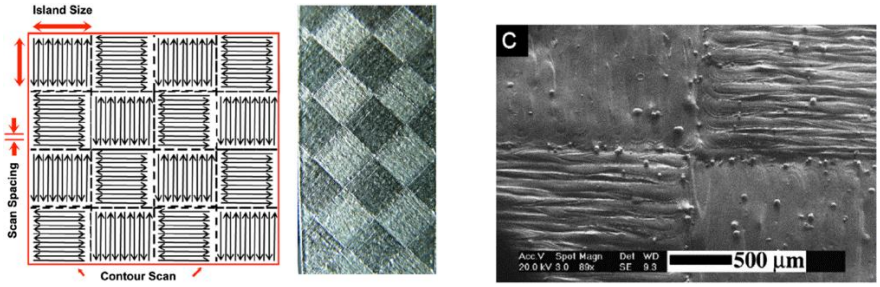

Figure J.6: Concept Laser M2 scanning strategy ('islands' scan strategy) (a) schematic and the (b) resulting surface viewed with an optical microscope and (c) viewed with a SEM (Qiu, Adkins and Attallah, 2013)

APPENDIX K: PHASE TRANSFORMATION

K.1. TTT DIAGRAM OF TI6AL4V

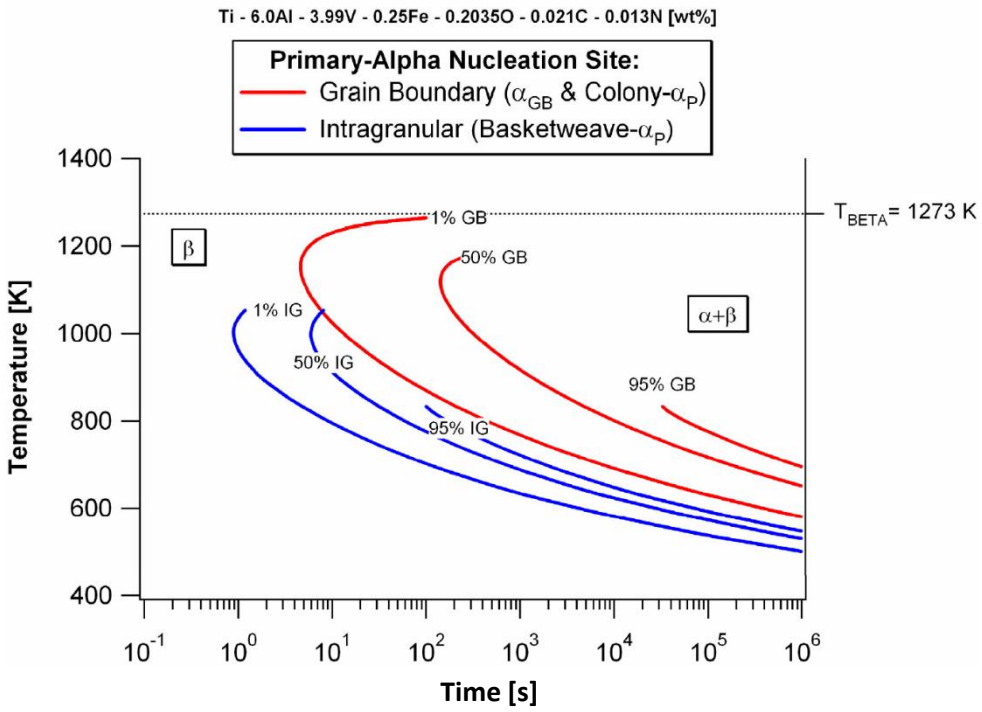

Figure K.1: TTT diagram of Ti6Al4V (Kelly, 2004)

K.2. TRANSFORMATION CHARACTERISTICS

Table K.1Transformation products, rates and temperatures (Kelly, 2004)

Transformation product	Cooling rate [K/s]	Start Temperature
Allotriomorphic (α_{GB})	CR < 20	1243-1273K
Widmanstätten (α) (Colony α_P, Basketweave α_{BW})	CR < 20	~1173K,Ref.[29]; ~1223K,Ref.[30]
Massive (α_m)	20< CR <410	1243-1273K
Martensitic (α′)	CR>410	M_S = 848K

APPENDIX L: THERMOMECHANICAL PROCESSING

L.1. PRODUCTION OF INGOT AND WROUGHT PARTS

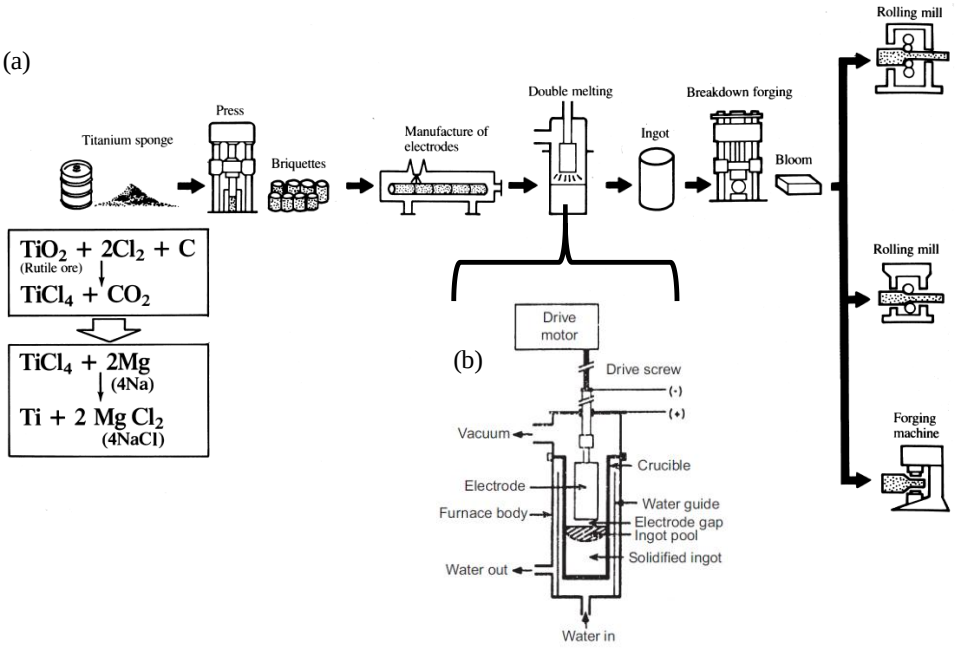

Figure L.1: Production of wrought Ti and Ti-alloys from Ti sponge. (Donachie, 2000: 26) (b) Components of the VAR process (Donachie, 2000: 27)

L.2. INDUSTRIAL TMP STRATEGIES

Table L.1: Industrial TMP strategies (Welsch, Boyer and Collings, 1993)

Heat-treatment designation	Heat-treatment cycle	Microstructure
Duplex anneal (or overage)	Solution treat at 50–75 °C (90–135 °F) below T_β(a), air cool and age for 2–8 h at 540–675 °C (1000–1250 °F)	Primary α, plus Widmanstätten α–β regions
Solution treat and age	Solution treat at ~40 °C (70 °F) below T_β, water quench(b) and age for 2–8 h at 535–675 °C (995–1250 °F)	Primary α, plus tempered α′ or α β–α mixture
Beta anneal	Solution treat at ~15 °C (30 °F) above T_β, air cool and stabilize at 650–760 °C (1200–1400 °F) for 2 h	Widmanstätten α–β colonies
Beta quench (Beta STOA)	Solution treat at ~15 °C (30 °F) above T_β, water quench and temper at 650–760 °C (1200–1400 °F) for 2 h	Tempered α′
Recrystallization anneal	925 °C (1700 °F) for 4 h, cool at 50 °C/h (90 °F/h) to 760 °C (1400 °F), air cool	Equiaxed α with β at grain-boundary triple points
Mill anneal	α–β hot work plus anneal at 705 °C (1300 °F) for 30 min to several hours and air cool	Incompletely recrystallized α with a small volume fraction of small β particles

(a) T_β is the beta transus temperature for the particular alloy in question. (b) In more heavily β-stabilized alloys such as Ti-6Al-2Sn-4Zr-6Mo or Ti-6Al-6V-2Sn, solution treatment may be followed by air cooling. Subsequent aging causes precipitation of α phase to form an α–β mixture.

APPENDIX M: MATLAB CODE – β PHASE RECONSTRUCTION

```
function [ebsd] = main_reconstruction()
delete ebsd_file.txt out.txt beta_alltemp.txt
warning('off');
clear X sto
threashold = 30;
ebsd_a = ebsd('Ti-Hex');

[grains_a,ebsd_a.grainId]
=calcGrains(ebsd_a('indexed'),'angle',15*degree);

tP = grains_a.triplePoints('Ti-Hex','Ti-Hex','Ti-Hex');
totgrains = length(tP); %number of triple points

fl = 0; %flag
tstart = tic;

parfor g=1:totgrains

[TPgrains_id] = tP.grainId(g,:); %trip alpha ids (1x3)

% calc beta to return single beta solution (see calc_beta function
below)
[solutionbeta,quest]=calc_beta(grains_a,TPgrains_id,threashold);

% question: is flag 1? (has a solution been return by calc_beta?
if YES, then continue)

if quest~=0

     fl=fl+1;
     [a,b,c,~] = Euler(solutionbeta,'Bunge');
     phibeta=rad2deg(a); %convert Euler angle to degree
     thetaneta=rad2deg(b);
     psibeta=rad2deg(c);

 %write solution to trip point co-ordinate
 hoeke_pix = [phibeta,theta,psibeta,tP(g).x,tP(g).y];
 dlmwrite('ebsd_file.txt',hoeke_pix,'-append','delimiter','\t')


cs=crystalSymmetry('cubic');
ss=specimenSymmetry('triclinic');
r=rotation('Euler', phibeta*degree, theta*degree, psibeta*degree);
%BETA solution rotation (B)
hoek = orientation(r, cs,ss); %beta solution orientation (S*B)

%~~~~~~~~~~~~~~~~~~~~ VARIENT SUBROUTINE HERE !!!!!!!
%X represents varient 1-12
X(g) = variant_distribution (hoek, TPgrains_id,grains_a);

%store hex trip grain IDs and variant number
```

```
sto(g,:) = [TPgrains_id,X(g)];

%write separate variants into separate text files
variantSub(sto(g,:),ebsd_a);
%~~~~~~~~~~~~~~~~~~~~~~~~~~~~~~~~~~~~~~~~~~~

    end
end
```

```
function [solution, q] = calc_beta (grains,TPgrains_id,threashold)

q=1; %flag variable

%the mean orientation of each tripel point alpha grain
%(1x3) euler angles in radians
var1=grains(TPgrains_id(1,1)).meanOrientation.Euler;
var2=grains(TPgrains_id(1,2)).meanOrientation.Euler;
var3=grains(TPgrains_id(1,3)).meanOrientation.Euler;

ori_1 = rotation('Euler',var1);
ori_2 = rotation('Euler',var2);
ori_3 = rotation('Euler',var3);

cs=crystalSymmetry('6/mmm', [2.954 2.954 4.729], 'X||a*', 'Y||b',
'Z||c', 'mineral', 'Ti-Hex');
ss=specimenSymmetry('triclinic');

rot1 = orientation(ori_1,cs,ss);
rot2 = orientation(ori_2,cs,ss);
rot3 = orientation(ori_3,cs,ss);

s=symmetrise(rot1,cs,ss);
s2=symmetrise(rot2,cs,ss);
s3=symmetrise(rot3,cs,ss);

s = s(s.i==0); %get rid of inverses
s2 = s2(s2.i==0);
s3 = s3(s3.i==0);

%BOR angle in radians
d=rotation('Euler', 135*degree, 90*degree, 355*degree);

for i=1:2:5
    betaa(i)=s(i)*inv(d);
    betaa2(i)=s2(i)*inv(d);
    betaa3(i)=s3(i)*inv(d);
end

for i=8:2:12 %select the correct variants
    betaa(i)=s(i)*inv(d);
```

```
    betaa2(i)=s2(i)*inv(d);
    betaa3(i)=s3(i)*inv(d);
end

betaa=betaa.unique; %get rid of zero rows
betaa2=betaa2.unique;
betaa3=betaa3.unique;

betaa(:,1) = []; %6 BETA rotations (rotation matrix)
betaa2(:,1) = []; %6 BETA rotations from single variant s2
betaa3(:,1) = []; %6 BETA rotations from single variant s3

cs=crystalSymmetry('m-3m', [3.192 3.192 3.192], 'mineral',
'Titanium cubic');
ss=specimenSymmetry('triclinic');

ori = orientation(betaa(:), cs,ss); %6x1 matrix 6 variants (6rows)
ori2 = orientation(betaa2(:), cs,ss);
ori3 = orientation(betaa3(:), cs,ss);

beta_1=ori; %6 beta solutions orientations from a single alpha
beta_2=ori2;
beta_3=ori3;

%trip point beta misorientation minimisation routine
parfor i=1:6
    for j=1:6
        mis12(i,j)=angle(beta_1(i),beta_2(j))/degree; %calc angle
        mis13(i,j)=angle(beta_1(i),beta_3(j))/degree;
        mis32(i,j)=angle(beta_3(i),beta_2(j))/degree;
    end
end

%find minimum angle between solutions
[x,y]=find(mis12==min(min(mis12)));

value=mis12(x(1),y(1));
if (value < threashold)
    beta1=beta_1(x(1));

    [xx,yy]=find(mis13==min(mis13(x(1),:))); %find second min

    value2 =mis13(xx(1),yy(1));
    if (value2 < threashold)

        value3=mis32(yy(1),y(1));

        if (value3 < threashold)

            solution=beta1; %single solution found
        else
            solution=0;
            q=0;

        end
    else
```

```
        solution=0;
        q=0;

    end
else
    solution=0;
    q=0;

end
end
```